University of Massachusetts Amherst
ScholarWorks@UMass Amherst

Doctoral Dissertations | Dissertations and Theses

November 2015

Improving Sea-Surface Remote Sensing of Ocean Wind Vectors by Scatterometers

Joseph W. Sapp
University of Massachusetts - Amherst

Follow this and additional works at: https://scholarworks.umass.edu/dissertations_2

Part of the Electromagnetics and Photonics Commons, and the Other Electrical and Computer Engineering Commons

Recommended Citation

Sapp, Joseph W., "Improving Sea-Surface Remote Sensing of Ocean Wind Vectors by Scatterometers" (2015). *Doctoral Dissertations*. 469.
https://scholarworks.umass.edu/dissertations_2/469

This Open Access Dissertation is brought to you for free and open access by the Dissertations and Theses at ScholarWorks@UMass Amherst. It has been accepted for inclusion in Doctoral Dissertations by an authorized administrator of ScholarWorks@UMass Amherst. For more information, please contact scholarworks@library.umass.edu.

IMPROVING SEA-SURFACE REMOTE SENSING OF OCEAN WIND VECTORS BY SCATTEROMETERS

A Dissertation Presented

by

JOSEPH W. SAPP

Submitted to the Graduate School of the
University of Massachusetts Amherst in partial fulfillment
of the requirements for the degree of

DOCTOR OF PHILOSOPHY

September 2015

Electrical and Computer Engineering

© Copyright by Joseph W. Sapp 2015

All Rights Reserved

IMPROVING SEA-SURFACE REMOTE SENSING OF OCEAN WIND VECTORS BY SCATTEROMETERS

A Dissertation Presented

by

JOSEPH W. SAPP

Approved as to style and content by:

Stephen Frasier, Chair

Ramakrishna Janaswamy, Member

Bruce Turkington, Member

Paul Chang, Member

Zorana Jelenak, Member

Christopher V. Hollot, Department Chair
Electrical and Computer Engineering

DEDICATION

To my bride, Renee, and our children.

The men were amazed and asked,
"What kind of man is this? Even
the winds and the waves obey him!"

Matthew 8:27 (NIV)

ACKNOWLEDGMENTS

There are many people who have lifted up this project in one way or another. First I need to thank Paul Chang and Zorana Jelenak. For all the years I have known them they have been wise, professional coaches. I would like to think that their advice (and prodding) have made me a better researcher. This dissertation would not be the same without them and I thank them for being on my committee. (I also appreciate the friendly pressure they put on me during travel to try new things. I would also like to think that this has made me more adventurous and comfortable in new situations, which are invaluable qualities to acquire.)

Tom Hartley was always available to help with hardware advice, IWRAP installation, and did much of the Ettus upgrade. I'm grateful for his diligence, patience with me (especially during those long Tampa days), and general consideration of others. It was always a bit more motivation to get things done in Tampa early enough to swing by Cigar City Brewing with Tom.

Among the other denizens of MIRSL, the work presented here owes a lot to Jason Dvorsky. Besides helping with IWRAP install and uninstall and taking shifts on storm flights, he flew the entire Winter 2011 season—the data from which the last chapter of this dissertation came. I especially appreciated this effort because I didn't have to spend time away from my oldest daughter, who was 9 months old.

I was happy to call Tony Swochak and Tony Hopf friends and received much encouragement from them. Vijay Venkatesh, with whom I took a radar truck across the country within a month of moving to Massachusetts, was and continues to be a sensible adviser. And to Krzystof Orzel, whose friendship helped sustain my efforts

and buoy my spirits, I am very thankful. I always looked forward to Friday for what I considered The Weekly Summary and Preparation for That to Come which, of course, was conjoined with a *piwo*.

Early on at UMass, we visited Stony Brook Community Church—and never had reason to look anywhere else. Thanks to everybody there, I am now spoiled for the rest of my life. We may never be part of a (local) church with more PhDs per capita again. Though we made friends with nearly all the regulars, I'd like to recognize a few in particular. Dan Brown encouraged me, and was a special teacher since his family's journey through his grad school time was similar to mine. He and his wife introduced us to Bill and Erika van Duzer, with whom we were blessed to share much of our life and nearly all of our kids' birthdays. Jim Hartley provided some much-needed advice and wisdom on getting through the dissertation process, as well as a review of some early chapters. Dave Ranen was another good friend with whom I was able to share my passion for strengthening men. And to Bob and Aimee Gould, who welcomed us into their home and their lives right from the start, I can't be thankful enough.

It has been a pleasure to work with Linda Klemyk and, for the latter few years, Mary Nied. Their administration behind the scenes contributed to the more visible work that I was able to do. And it was always fun to bring the little ones by after a doctor's visit. As I learned here: "Life's too short to not have chocolate"—and, I would now add, animal crackers.

I owe much to my adviser, Steve Frasier. When I was touring MIRSL, I never thought that I would be participating in research flights on a NOAA Hurricane Hunter (for one, I think I naively assumed the operation was from the ground). It has turned out to be a unique and valuable educational and professional experience—not to mention that now I get to say casually that I've troubleshot a radar while circling outside a tropical storm.

I am very grateful that, from the beginning, Steve shouldered the burden of funding this research. He has also had patience with me on many occasions when he could have reasonably demanded more. This has translated into compassion that is probably rarely experienced in the graduate student world; the most recent example was just last year when he voluntarily sent me home and took over data collection on a research flight through his first hurricane. He could have easily justified staying back but considered my family's needs instead. Finally, he taught me how to conduct academic research while working with a challenging data set. I think it was good preparation for the world of remote sensing research.

Though I think my Mom and Dad weren't thrilled so much with the hurricane flights, they supported us in many ways during my time at MIRSL. They provided a good base from which I could start my career and are a treasured source of love, compassion, and practical advice. Thank you for always being available and helping me to grow, even still today.

Lastly, to my wife Renee: thank you! For your encouragement to start, and continue, this process (though we were only just married), your patience throughout, your willingness to make the sacrifices we've made, and your uplifting spirit. This was especially true when I felt led to pursue the Ph.D. instead of the originally-decided M.S. I couldn't have asked for a more faithful wife who is willing to argue with me so we can both be better off. And while we didn't think we'd become parents while completing this, I couldn't have planned it better. Seeing you add Mother to your skillset has been beautiful. Like you reminded me so often, a large part of this effort was so that our children could have a better life. And I think our experience during this time has certainly made all of our lives richer.

ABSTRACT

IMPROVING SEA-SURFACE REMOTE SENSING OF OCEAN WIND VECTORS BY SCATTEROMETERS

SEPTEMBER 2015

JOSEPH W. SAPP

B.S., THE PENNSYLVANIA STATE UNIVERSITY

Ph.D., UNIVERSITY OF MASSACHUSETTS AMHERST

Directed by: Professor Stephen Frasier

Though scatterometers have been used to sense global ocean surface wind vectors for over 40 years, there remain some significant shortcomings. The largest problems appear in retrieving the wind vector when the ocean is being driven by high wind speeds or when rain is present in the beam-illuminated volume. Geophysical model functions (GMFs) developed using data from high-wind events can improve retrievals at high wind speeds, but only if sufficient ground truth measurements exist in the scatterometer swath. Airborne scatterometers, such as the Imaging Wind and Rain Airborne Profiler (IWRAP) developed by the Microwave Remote Sensing Laboratory (MIRSL) at the University of Massachusetts Amherst (UMass), are well-suited for collecting such high-wind data, largely due to their abilities to reposition to areas of interest, sample the ocean surface on a small scale, and use complementary in-situ sensors. The IWRAP system is also able to investigate the effect of precipitation

impact (the "splash effect") on the sea surface normalized radar cross-section (NRCS), since it can discriminate between volume and surface effects of precipitation. This dissertation will improve upon the existing IWRAP GMF and quantify the effect of precipitation on wind vector retrievals. Additionally, IWRAP is used to observe the effects of Earth-incidence angle and polarization on the sea-surface radar backscatter, helping scatterometer GMFs to be applicable to other satellite sensors.

IWRAP and collocated Stepped Frequency Microwave Radiometer (SFMR) data were gathered from 4 years of flight experiments. Using this data, the high-wind IWRAP GMF is extended to incidence angles near 22° at C- and Ku-band VV- and HH-polarization from $15\,\mathrm{m\,s^{-1}}$ to $45\,\mathrm{m\,s^{-1}}$. There is also a revision made to the higher harmonics of the GMF near 50° incidence, but the mean NRCS appears to be modeled appropriately. There is no splash effect observed in the mean NRCS or first harmonic at wind speeds from $15\,\mathrm{m\,s^{-1}}$ to $45\,\mathrm{m\,s^{-1}}$. The second harmonic shows some muted behavior in precipitation. Lastly, a wind speed dependence is observed in the VV/HH NRCS polarization ratio in both incidence angle and azimuth.

CONTENTS

Page

ACKNOWLEDGMENTS . . . . . **vi**

ABSTRACT . . . . . **ix**

LIST OF TABLES . . . . . **xiv**

LIST OF FIGURES . . . . . **xv**

LIST OF ACRONYMS . . . . . **xxv**

CHAPTER

1. INTRODUCTION **1**

1.1 Scatterometry 1
1.2 Radar Operation 4
1.3 A Brief History of Satellite Scatterometry 6
1.4 Dissertation Outline 9

2. INSTRUMENTATION AND FIELD EXPERIMENT DESCRIPTIONS **11**

2.1 The Imaging Wind and Rain Airborne Profiler 11

2.1.1 System Description 11
2.1.2 Summary of System Changes 18

2.1.2.1 Changes to the Location of the Ku-band Front-End 18
2.1.2.2 Pulse Compression 19
2.1.2.3 Dual- and Cross-Polarization 20
2.1.2.4 Software-Configurable Incidence Angles 20
2.1.2.5 Calibration and Digital Receiver Improvements 21

2.2 The Stepped Frequency Microwave Radiometer 22
2.3 Experiment Descriptions 27

3. HIGH-WIND-SPEED RAIN-FREE GEOPHYSICAL MODEL FUNCTION IMPROVEMENT 30

3.1 Introduction 30
3.2 Adjustment to the Wind Speed Dependence of the IWRAP Geophysical Model Function 34
3.3 Variability and Calibration Methods 35

3.3.1 Statistical Variability 39
3.3.2 Geophysical Variability 40
3.3.3 Sampling Uncertainty 42
3.3.4 Calibration Offset 43

3.4 Methodology for Developing a New Rain-Free Geophysical Model Function 48

3.4.1 SFMR Reprocessing 48
3.4.2 IWRAP Data Processing 49

3.5 Results of the New Rain-Free Geophysical Model Function 53

3.5.1 NRCS Response to Azimuth and Wind Speed 53
3.5.2 Mean NRCS Response to Wind Speed 58
3.5.3 Response of Higher-Order Coefficients to Wind Speed 66

3.6 Conclusion 74

4. PRECIPITATION SPLASH EFFECTS ON HIGH-SPEED OCEAN-SURFACE WIND VECTOR MEASUREMENTS 78

4.1 Introduction 78
4.2 Remote Sensing of Precipitation 80

4.2.1 Volume Scattering 80
4.2.2 Dual-Frequency Attenuation Estimation 82
4.2.3 Reducing the Uncertainty of the $\bar{K}_s$ Measurement 85

4.3 Experiment Methodology 86

4.3.1 Path-averaged Specific Attenuation-SFMR Rain Rate Model 86
4.3.2 Splash Effect 90

4.4 Analysis of Observed NRCS with Respect to Reference NRCS 92

4.4.1 K_s–R Models vs. SFMR Rain Rate 92
4.4.2 Effect of Precipitation on NRCS 93

4.4.2.1 Effect of Precipitation on Fourier Coefficients 95
4.4.2.2 Azimuthal Behavior 105

4.5 Conclusion 107

5. POLARIZATION RATIO EFFECTS OF HIGH WIND SPEEDS AT C-BAND 112

5.1 Introduction 112
5.2 Experiment Description 113
5.3 Data Processing Methodology 115
5.4 Results 121
5.5 Summary 128

6. CONCLUSION AND FUTURE WORK 129

BIBLIOGRAPHY 131

LIST OF TABLES

Table **Page**

3.1 Remapped IWRAP GMF Coefficients: A_0 Parameters 36

3.2 Remapped IWRAP GMF Coefficients: a_1 Parameters 37

3.3 Remapped IWRAP GMF Coefficients: a_2 Parameters 37

3.4 IWRAP-2014 GMF Coefficients: A_0 Parameters 75

3.5 IWRAP-2014 GMF Coefficients: a_1 Parameters 75

3.6 IWRAP-2014 GMF Coefficients: a_2 Parameters 75

5.1 C-band Radar Parameters 113

5.2 Summary of the Winter 2011 Flight Experiment 114

5.3 Coefficients for the Fit of the Mean VV-polarized NRCS as a Function of Wind-relative Azimuth Angle to $A + B\cos\ \chi + C\cos\ 2\chi$ in Linear Units 125

5.4 Coefficients for the Fit of the Mean HH-polarized NRCS as a Function of Wind-relative Azimuth Angle to $A + B\cos\ \chi + C\cos\ 2\chi$ in Linear Units 125

5.5 Coefficients for the Fit of the Mean Polarization Ratio as a Function of Wind-relative Azimuth Angle to $A + B\cos\ \chi + C\cos\ 2\chi$ in Linear Units 128

LIST OF FIGURES

Figure **Page**

2.1 Typical configuration of the IWRAP scatterometer/profiler instrument on the NOAA WP-3D aircraft. The incidence angle, conical scan rate, transmit and receive polarizations, pulse compression mode, pulse length, and pulse repetition frequency (PRF), among others, are all configurable. 12

2.2 Block diagram of the IWRAP C-band front-end. The switches are configured for transmit mode. The dashed box indicates the grouping of components within a rack-mounted enclosure. 12

2.3 Block diagram of the current configuration of the IWRAP Ku-band front-end. The switches are configured for transmit mode. The dashed boxes indicate the grouping of components into rack-mounted enclosures, and the dotted boxes indicate components grouped into separate boxes on the front-end/antenna mounting plate. 14

2.4 Block diagram of the current IWRAP C-band transceiver and front-end. The switches are configured for receive mode. The RF portion is also shown in figure 2.2. 16

2.5 Block diagram of the current IWRAP Ku-band transceiver and front-end. The switches are configured for receive mode. The RF portion is also shown in figure 2.3. 17

2.6 SFMR GMF developed by Uhlhorn and Black [28]. The left panel shows the change in brightness temperatures (T_bs) as a function of wind speed only. The center panel shows the same as a function solely of rain rate. The right panel shows the T_b response to SST. 26

3.1 Illustration of the change in SFMR model of excess emissivity due to wind. The 2003 model overestimated wind speeds below approximately $58\,\mathrm{m\,s^{-1}}$. 36

3.2 Illustration of the change in IWRAP GMF due to a change in the SFMR GMF. The upper curves are the old (dashed) and remapped (solid) C-band VV-polarization GMF at 50°. The lower curves are the old (dash-dotted) and remapped (solid) C-band HH-polarization GMF at 49°. An underestimation of SFMR wind speeds above approximately 58 $\mathrm{m\,s^{-1}}$ results in an expected lower observed NRCS. 38

3.3 Mean IWRAP NRCS (A_0) vs. SFMR Wind Speed for four flights in the 2014 hurricane season, illustrating variability both within a flight and between flights. These data are from the outer incidence angle (47.4°) of the C-band radar at VV-polarization. The points are A_0 estimates from individual wind vector cells of alongtrack distance 0.5 km. The data are binned into 2.5 $\mathrm{m\,s^{-1}}$-wide wind speed bins. The solid lines are the interquartile means and the error bars are the interquartile standard deviations. 39

3.4 Mean NRCS (A_0) estimates, shown as empty circles, for the inner angle of the C-band radar at VV-polarization for the flight experiment on January 21, 2014. A_0 samples are grouped into wind speed bins of 2.5 $\mathrm{m\,s^{-1}}$ and averaged. The mean A_0 values for each bin are plotted as filled circles and the standard deviations are the error bars. The IWRAP GMF, which is only valid above 25 $\mathrm{m\,s^{-1}}$, is shown as a blue solid line. Note the vertically displaced cloud of NRCS measurements, which skews the mean in at least 3 wind speed bins. 44

3.5 Mean NRCS (A_0) estimates, shown as empty circles, for the outer angle of the C-band radar at VV-polarization for the flight experiment on January 21, 2014. A_0 samples are grouped into wind speed bins of 2.5 $\mathrm{m\,s^{-1}}$ and averaged. The mean A_0 values for each bin are plotted as filled circles and the standard deviations are the error bars. The IWRAP GMF, which is only valid above 25 $\mathrm{m\,s^{-1}}$, is shown as a blue solid line. These NRCS measurements are consistent over the flight. 45

3.6 Schematic diagram of the binning scheme for one wind vector cell. Aircraft motion is upwards and illumination of the surface is shown as solid circles. An NRCS sample is included in the average if the center of the beam falls between the solid lines. Azimuthal averaging is not depicted. 50

3.7 C-band NRCS vs. azimuth for VV-polarization at 21.7° incidence for wind speed bins from $15\,\mathrm{m\,s^{-1}}$ to $45\,\mathrm{m\,s^{-1}}$. Each wind speed bin is $2.5\,\mathrm{m\,s^{-1}}$ wide. Several GMFs are shown alongside the fit to the data, which is shown as a purple line. The IWRAP GMF was not designed to be used below $25\,\mathrm{m\,s^{-1}}$, so it is not shown in this region. 54

3.8 C-band NRCS vs. azimuth for HH-polarization at 22.4° incidence for wind speed bins from $15\,\mathrm{m\,s^{-1}}$ to $45\,\mathrm{m\,s^{-1}}$. Each wind speed bin is $2.5\,\mathrm{m\,s^{-1}}$ wide. Several GMFs are shown alongside the fit to the data, which is shown as a purple line. The IWRAP GMF was not designed to be used below $25\,\mathrm{m\,s^{-1}}$, so it is not shown in this region. 55

3.9 C-band NRCS vs. azimuth for VV-polarization at 47.4° incidence for wind speed bins from $15\,\mathrm{m\,s^{-1}}$ to $45\,\mathrm{m\,s^{-1}}$. Each wind speed bin is $2.5\,\mathrm{m\,s^{-1}}$ wide. Several GMFs are shown alongside the fit to the data, which is shown as a purple line. The IWRAP GMF was not designed to be used below $25\,\mathrm{m\,s^{-1}}$, so it is not shown in this region. 56

3.10 C-band NRCS vs. azimuth for HH-polarization at 47.8° incidence for wind speed bins from $15\,\mathrm{m\,s^{-1}}$ to $45\,\mathrm{m\,s^{-1}}$. Each wind speed bin is $2.5\,\mathrm{m\,s^{-1}}$ wide. Several GMFs are shown alongside the fit to the data, which is shown as a purple line. The IWRAP GMF was not designed to be used below $25\,\mathrm{m\,s^{-1}}$, so it is not shown in this region. 57

3.11 Ku-band NRCS vs. azimuth for VV-polarization at 21.7° incidence for wind speed bins from $15\,\mathrm{m\,s^{-1}}$ to $45\,\mathrm{m\,s^{-1}}$. Each wind speed bin is $2.5\,\mathrm{m\,s^{-1}}$ wide. Several GMFs are shown alongside the fit to the data, which is shown as a purple line. The IWRAP GMF was not designed to be used below $25\,\mathrm{m\,s^{-1}}$, so it is not shown in this region. 58

3.12 Ku-band NRCS vs. azimuth for HH-polarization at 22.2° incidence for wind speed bins from $15\,\mathrm{m\,s^{-1}}$ to $45\,\mathrm{m\,s^{-1}}$. Each wind speed bin is $2.5\,\mathrm{m\,s^{-1}}$ wide. Several GMFs are shown alongside the fit to the data, which is shown as a purple line. The IWRAP GMF was not designed to be used below $25\,\mathrm{m\,s^{-1}}$, so it is not shown in this region. 59

3.13 Ku-band NRCS vs. azimuth for VV-polarization at 45.6° incidence for wind speed bins from $15\,\mathrm{m\,s^{-1}}$ to $45\,\mathrm{m\,s^{-1}}$. Each wind speed bin is $2.5\,\mathrm{m\,s^{-1}}$ wide. Several GMFs are shown alongside the fit to the data, which is shown as a purple line. The IWRAP GMF was not designed to be used below $25\,\mathrm{m\,s^{-1}}$, so it is not shown in this region. 60

3.14 Ku-band NRCS vs. azimuth for HH-polarization at 46.7° incidence for wind speed bins from $15\,\mathrm{m\,s^{-1}}$ to $45\,\mathrm{m\,s^{-1}}$. Each wind speed bin is $2.5\,\mathrm{m\,s^{-1}}$ wide. Several GMFs are shown alongside the fit to the data, which is shown as a purple line. The IWRAP GMF was not designed to be used below $25\,\mathrm{m\,s^{-1}}$, so it is not shown in this region. 61

3.15 C-band mean NRCS vs. wind speed (A_0 term) for 21.7° and 22.4° incidence (upper panels) and 47.4° and 47.8° incidence (lower panels), VV-polarization (left panels) and HH-polarization (right panels). A_0 data are shown as filled circles with the standard deviation of A_0 estimates from all wind vector cells shown as the error bars. GMFs shown where valid are IWRAP (dashed), CMOD5.n (dash-dotted), CMOD5.h (long dashes), and C-2013 (dotted). The new IWRAP GMF is shown as a solid line. 62

3.16 Ku-band mean NRCS vs. wind speed (A_0 term) for 21.7° and 22.2° incidence (upper panels) and 45.6° and 46.7° incidence (lower panels), VV-polarization (left panels) and HH-polarization (right panels). A_0 data are shown as filled circles with the standard deviation of A_0 estimates from all wind vector cells shown as the error bars. GMFs shown where valid are IWRAP (dashed), NSCAT2 (dash-dotted), and Ku-2011 (dotted). The new IWRAP GMF is shown as a solid line. 64

3.17 C-band a_1 term ($\frac{A_1}{A_0}$) of the NRCS vs. wind speed for 21.7° and 22.4° incidence (upper panels) and 47.4° and 47.8° incidence (lower panels), VV-polarization (left panels) and HH-polarization (right panels). a_1 data are shown as filled circles with the standard deviation of a_1 estimates from all wind vector cells shown as the error bars. GMFs shown where valid are IWRAP (dashed) and CMOD5.n (dash-dotted). Note that CMOD5.h has the same a_1 response as CMOD5.n. The new IWRAP GMF is shown as a solid line. 68

3.18 Ku-band a_1 term ($\frac{A_1}{A_0}$) of the NRCS vs. wind speed for 21.7° and 22.2° incidence (upper panels) and 45.6° and 46.7° incidence (lower panels), VV-polarization (left panels) and HH-polarization (right panels). a_1 data are shown as filled circles with the standard deviation of a_1 estimates from all wind vector cells shown as the error bars. GMFs shown where valid are IWRAP (dashed) and Ku-2011 (dash-dotted). The new IWRAP GMF is shown as a solid line. 69

3.19 C-band a_2 term ($\frac{A_2}{A_0}$) of the NRCS vs. wind speed for 21.7° and 22.4° incidence (upper panels) and 47.4° and 47.8° incidence (lower panels), VV-polarization (left panels) and HH-polarization (right panels). a_2 data are shown as filled circles with the standard deviation of a_2 estimates from all wind vector cells shown as the error bars. GMFs shown where valid are IWRAP (dashed) and CMOD5.n (dash-dotted). Note that CMOD5.h has the same a_1 response as CMOD5.n. The new IWRAP GMF is shown as a solid line. 70

3.20 Ku-band a_2 term ($\frac{A_2}{A_0}$) of the NRCS vs. wind speed for 21.7° and 22.2° incidence (upper panels) and 45.6° and 46.7° incidence (lower panels), VV-polarization (left panels) and HH-polarization (right panels). a_2 data are shown as filled circles with the standard deviation of a_2 estimates from all wind vector cells shown as the error bars. GMFs shown where valid are IWRAP (dashed) and Ku-2011 (dash-dotted). The new IWRAP GMF is shown as a solid line. 71

3.21 C-band upwind NRCS less crosswind NRCS vs. wind speed, calculated according to (3.5). σ^0 is divided by A_0 (in linear units) for ease of display. The new IWRAP GMFs are shown as a solid line. The existing IWRAP GMFs are shown as a dashed line and CMOD5.n is shown as a dash-dotted line. The trend of the new IWRAP GMFs matches better with CMOD5.n than with the existing IWRAP GMFs. 72

3.22 Ku-band upwind NRCS less crosswind NRCS vs. wind speed, calculated according to (3.5). σ^0 is divided by A_0 (in linear units) for ease of display. The new IWRAP GMFs are shown as a solid line. The existing IWRAP GMFs are shown as a dashed line and Ku-2011 is shown as a dash-dotted line. The trend of the new IWRAP GMFs matches better with Ku-2011 than with the existing IWRAP GMFs. 73

4.1 Schematic diagram of the limits placed on collocated C-band and Ku-band 360° scans. The C-band scans have the smaller scan radius with crosshatched circles representing the ocean surface illumination. The filled circles represent the surface illumination at Ku-band. The `X` symbol is the mean position of the aircraft during the C-band scan and the `+` symbol is the same for the Ku-band scan. The two scans shown here are offset in time by 0.5 s, illustrating a scenario in which the positions of the two antennas are not synchronized. For the two scans shown here, d_1 and d_2 must be at most 0.8 km each. This keeps the volumes of each scan close at typical altitudes (between 2 km and 3.4 km) and incidence angles of this dataset. Additionally, the time taken to traverse d_3 (e.g., $t = v_g \cdot d_3$) must be less than 0.6 s. 88

4.2 A rainy scan, having significant precipitation in at least 75 % of the scan. The left panel shows the equivalent reflectivity (Z_e) of the C-band radar, and the right panel shows the same for the Ku-band radar. The top of the plot is the range bin of the aircraft and the high-reflectivity horizontal stripe between 2 km to 2.5 km is the surface echo. 89

4.3 A discarded scan due to the presence of precipitation, but not in 75 % of the scan. The left panel shows the equivalent reflectivity (Z_e) of the C-band radar, and the right panel shows the same for the Ku-band radar. The top of the plot is the range bin of the aircraft and the high-reflectivity horizontal stripe between 2 km to 2.5 km is the surface echo. 90

4.4 Path-averaged attenuation ($\bar{K}_s$) at Ku-band vs. SFMR rain rate for the flight experiment through Hurricane Gustav on August 31, 2008. Each rain rate bin is 1 mm h^{-1} wide. The error bars show one standard deviation of the data on either side of the mean. Several GMFs are shown alongside the fit to the data, which is shown as a purple line. The model derived from IWRAP and SFMR data in 2006 is shown as a dashed line. Two models at wavelengths near Ku-band from Atlas and Ulbrich [57] are shown as long-dashed and dash-dotted lines. The ITU-R P.838-3 model [58] at Ku-band is shown as a dotted line. 94

4.5 Mean NRCS vs. wind speed (A_0 term), uncorrected, for 21.7° and 22.4° incidence at C-band (upper panels) and 21.7° and 22.2° incidence at Ku-band (lower panels). VV-polarization responses to wind speed are in the left panels and those for HH-polarization are in the right panels. Rain-free A_0 data are shown as filled circles with the standard deviation of A_0 estimates from all rain-free wind vector cells shown as the error bars. A_0 data from light rain are shown as empty circles with a fit to the data shown as a dashed line. The new IWRAP GMF from chapter 3 is shown as a solid line. 96

4.6 Mean NRCS vs. wind speed (A_0 term), corrected for attenuation, for 21.7° and 22.4° incidence at C-band (upper panels) and 21.7° and 22.2° incidence at Ku-band (lower panels). VV-polarization responses to wind speed are in the left panels and those for HH-polarization are in the right panels. Rain-free A_0 data are shown as filled circles with the standard deviation of A_0 estimates from all rain-free wind vector cells shown as the error bars. A_0 data from light rain are shown as empty circles with a fit to the data shown as a dashed line. The new IWRAP GMF from chapter 3 is shown as a solid line. 97

4.7 Mean NRCS vs. wind speed (A_0 term), uncorrected, for 21.7° and 22.4° incidence at C-band (upper panels) and 21.7° and 22.2° incidence at Ku-band (lower panels). VV-polarization responses to wind speed are in the left panels and those for HH-polarization are in the right panels. Rain-free A_0 data are shown as filled circles with the standard deviation of A_0 estimates from all rain-free wind vector cells shown as the error bars. A_0 data from all rainy cells are shown as empty diamonds with a fit to the data shown as a dashed line. The new IWRAP GMF from chapter 3 is shown as a solid line. 98

4.8 Mean NRCS vs. wind speed (A_0 term), corrected for attenuation, for 21.7° and 22.4° incidence at C-band (upper panels) and 21.7° and 22.2° incidence at Ku-band (lower panels). VV-polarization responses to wind speed are in the left panels and those for HH-polarization are in the right panels. Rain-free A_0 data are shown as filled circles with the standard deviation of A_0 estimates from all rain-free wind vector cells shown as the error bars. A_0 data from all rainy cells are shown as empty diamonds with a fit to the data shown as a dashed line. The new IWRAP GMF from chapter 3 is shown as a solid line. 99

4.9 Normalized NRCS A_1 term (a_1) vs. wind speed, corrected for attenuation, for 21.7° and 22.4° incidence at C-band (upper panels) and 21.7° and 22.2° incidence at Ku-band (lower panels). VV-polarization responses to wind speed are in the left panels and those for HH-polarization are in the right panels. Rain-free a_1 data are shown as filled circles with the standard deviation of a_1 estimates from all rain-free wind vector cells shown as the error bars. a_1 data from all rainy cells are shown as empty diamonds with a fit to the data shown as a dashed line. The new IWRAP GMF from chapter 3 is shown as a solid line. 101

4.10 Normalized NRCS A_2 term (a_2) vs. wind speed, corrected for attenuation, for 21.7° and 22.4° incidence at C-band (upper panels) and 21.7° and 22.2° incidence at Ku-band (lower panels). VV-polarization responses to wind speed are in the left panels and those for HH-polarization are in the right panels. Rain-free a_2 data are shown as filled circles with the standard deviation of a_2 estimates from all rain-free wind vector cells shown as the error bars. a_2 data from all rainy cells are shown as empty diamonds with a fit to the data shown as a dashed line. The new IWRAP GMF from chapter 3 is shown as a solid line. 103

4.11 Upwind NRCS less crosswind NRCS vs. wind speed, corrected for attenuation, for 21.7° and 22.4° incidence at C-band (upper panels) and 21.7° and 22.2° incidence at Ku-band (lower panels). VV-polarization responses to wind speed are in the left panels and those for HH-polarization are in the right panels. NRCS is first normalized by A_0. Rain-free a_2 data are shown as filled circles with the standard deviation of a_2 estimates from all rain-free wind vector cells shown as the error bars. The normalized upwind/crosswind difference from the fits to the rainy data is shown as a solid line. The new IWRAP GMF from chapter 3 is shown as a dashed line. At C-band, the CMOD5.n GMF is also shown; at Ku-band, there are no GMFs near the incidence angles analyzed. 104

4.12 C-band NRCS vs. azimuth for VV-polarization at 21.7° incidence in precipitation for wind speed bins from $15\,\mathrm{m\,s^{-1}}$ to $45\,\mathrm{m\,s^{-1}}$, corrected for attenuation. The fit to the parameters are used to compute a model function, which is shown as solid lines. The new IWRAP GMF from chapter 3 is shown as dashed lines. 105

4.13 C-band NRCS vs. azimuth for HH-polarization at 22.4° incidence in precipitation for wind speed bins from $15\,\mathrm{m\,s^{-1}}$ to $45\,\mathrm{m\,s^{-1}}$, corrected for attenuation. The fit to the parameters are used to compute a model function, which is shown as solid lines. The new IWRAP GMF from chapter 3 is shown as dashed lines. 106

4.14 Ku-band NRCS vs. azimuth for VV-polarization at 21.7° incidence in precipitation for wind speed bins from $15\,\mathrm{m\,s^{-1}}$ to $45\,\mathrm{m\,s^{-1}}$, corrected for attenuation. The fit to the parameters are used to compute a model function, which is shown as solid lines. The new IWRAP GMF from chapter 3 is shown as dashed lines. 108

4.15 Ku-band NRCS vs. azimuth for HH-polarization at 22.2° incidence in precipitation for wind speed bins from $15\,\mathrm{m\,s^{-1}}$ to $45\,\mathrm{m\,s^{-1}}$, corrected for attenuation. The fit to the parameters are used to compute a model function, which is shown as solid lines. The new IWRAP GMF from chapter 3 is shown as dashed lines. 109

5.1 Diagram illustrating the rotation angle of the vector parallel to the H'-polarized electric field, γ, from horizontal. The aircraft is rolling at a $-20°$ angle and 0° pitch is assumed. The aircraft-relative unit vectors ($\hat{x'}$, $\hat{y'}$, $\hat{z'}$) are shown as dark blue dashed lines. The aircraft-relative azimuth (ϕ_a) for an incidence angle of 48°, shown as a red solid line, is 60°. This vector is perpendicular to the $\hat{\phi_a}$ vector. 118

5.2 Diagram illustrating the effects of polarization mixing on the transmit (a) and receive (b) vectors. 119

5.3 Summary from a circle pattern flown on January 24, 2011 for C-band VV-polarization. The wind speed was $22.5\,\mathrm{m\,s^{-1}}$. The CMOD5.N and the IWRAP VV-polarization GMF are also shown at the wind speeds for which they are defined. (Top) VV-polarized NRCS (A_0) versus incidence angle for all azimuthal directions. Each NRCS sample collected is shown as a gray dot. The mean NRCS is shown as a solid line. CMOD5.N is shown as a dashed line and values from the IWRAP GMF are shown as filled circles at the incidence angles for which it is valid. (Bottom) VV-polarized NRCS versus azimuth. Each NRCS sample is shown as a gray dot. All samples between 48° and 52° incidence are averaged every 5° in azimuth and are connected with a solid line. CMOD5.N is shown as a dashed line and the IWRAP GMF at 50° incidence is shown as a dash-dotted line. 122

5.4 Mean NRCS (A_0) versus incidence angle for circle patterns flown on all dates in the Winter 2011 experiment grouped by wind speed. The model functions shown are computed with the mean wind speed in each wind speed range. Mean NRCS samples at each incidence angle from each circle are shown as gray plus symbols (VV-pol) and gray diamond symbols (HH-pol). The uncertainties of these means are no greater than 0.4 dB. The mean of all samples within a wind speed bin is shown as a solid line. CMOD5.N is shown as a dashed line. The IWRAP VV-pol and HH-pol GMFs are shown as filled circles and squares, respectively, at the incidence angles for which they are valid. 123

5.5 Polarization ratio VV/HH versus incidence angle grouped by wind speed. Ratios of the mean NRCS samples at each incidence angle from each circle are shown as gray circles. The mean of these is shown as a solid line. Polarization ratio models from [6], [43], [64] are also shown for reference. 124

5.6 NRCS at an incidence angle of 50° versus wind-relative azimuth angle grouped by wind speed. The model functions shown are computed with the mean wind speed observed in each wind speed range. Mean NRCS samples at each incidence angle from each circle are shown as gray plus symbols (VV-pol) and gray diamond symbols (HH-pol). A function in the form of $A + B\cos\ \chi + C\cos\ 2\chi$ is fitted to the mean of each polarization's samples within a wind speed group and is shown as a solid line. The coefficients for each fit are reported in tables 5.3 and 5.4. CMOD5.N is shown as a dashed line and the IWRAP GMFs are shown as dash-dotted lines. 126

5.7 Polarization ratios VV/HH at incidence angle 50° versus wind-relative azimuth angle grouped by wind speed. Ratios of the mean NRCS sampled from each circle flight between 48° and 52° incidence are averaged in 5° azimuth bins and are shown as gray open circles. A function in the form of $A + B\cos\ \chi + C\cos\ 2\chi$ is fitted to the mean and is shown as a solid line. The coefficients for each fit are reported in table 5.5. The polarization ratio from Vachon and Wolfe [6] at 50° is shown for reference as a horizontal dashed line. 127

LIST OF ACRONYMS

ADC analog-to-digital converter

ADEOS Advanced Earth Observation Satellite

AOC National Oceanic and Atmospheric Administration (NOAA) Aircraft Operations Center

ASCAT Advanced Scatterometer on the MetOp satellite

DAC digital-to-analog converter

DFS Dual-Frequency Scatterometer

DR digital receiver

DRO dielectric resonator oscillator

ERS European Remote Sensing

FPGA field-programmable gate array

GMF geophysical model function

GPS global positioning system

IF intermediate frequency

ISRO Indian Space Research Organization

IWRAP Imaging Wind and Rain Airborne Profiler

LNA low-noise amplifier

LRC Langley Research Center

MIRSL Microwave Remote Sensing Laboratory

NOAA National Oceanic and Atmospheric Administration

NRCS normalized radar cross-section

NSCAT NASA Scatterometer

NWS National Weather Service

OSCAT Ocean Scatterometer on Oceansat-II

PA power amplifier

PRF pulse repetition frequency

PRT pulse repetition time

RCS radar cross-section

RF radio frequency

SAR synthetic aperture radar

SASS SEASAT-A Scatterometer

SFMR Stepped Frequency Microwave Radiometer

SNR signal-to-noise ratio

SST sea-surface temperature

$\mathbf{T_b}$ brightness temperature

TC tropical cyclone

TRMM Tropical Rainfall Measuring Mission

TS Tropical Storm

UMass University of Massachusetts Amherst

SFMR2 Simultaneous Frequency Microwave Radiometer

XOVWM Extended Ocean Vector Wind Mission

CHAPTER 1

INTRODUCTION

1.1 Scatterometry

Since 1974, when the S-193 instrument was flown on the Skylab satellite, microwave radars have been measuring ocean-surface wind vectors from space [1]. These radars, called scatterometers, transmit electromagnetic waves towards the Earth's surface and measure the average backscattered power. The primary goal of these instruments is to measure ocean surface wind vectors.

Scatterometers are specialized radars, or active remote sensing instruments: a signal is transmitted towards the object of interest and microwave energy scattered by the object is received by the same instrument. In this case the object is the ocean surface, which can be considered to be a collection of point targets. Electromagnetic waves transmitted by the scatterometer interact with any gravity-capillary waves on the ocean surface. Some power is scattered forward, away from the receiver, and some of it back towards the receiver. The amount of backscattered power is dependent on the surface wind stress and is used to infer the ocean surface wind speed and direction.

Capillary waves are believed to be in equilibrium with the wind-forced surface stress, which makes the scatterometer a reasonable estimator of surface winds [2]. The relationship between the measured surface stress and the actual wind speed at any altitude is dependent on atmospheric stability. These differences, however, are small over the open ocean and at wind speeds greater than a few meters per second. The reference altitude currently used for surface wind estimates is 10 m, and at neutral atmospheric stability it is written U_{10N}. This is the 10 m equivalent neutral

wind. While the actual wind vector at 10 m is not necessarily the same as U_{10N}, it is often very close; for this reason, the phrase "surface wind" is often used in place of "equivalent neutral wind."

Since scatterometers measure backscattered power, a method is required to translate this power into an equivalent neutral wind vector. Backscattered power measured by a radar is dependent on properties of the target, the radar, and the orientation of the two. To eliminate some of these instrumentation- and observation-related variables, power is converted to the unitless normalized radar cross-section (NRCS). In order to understand this measure more fully, a brief review of radar principles is described in section 1.2. For now it suffices to know that scatterometers measure NRCS from the sea surface and NRCS is related to the wind vector.

In order to retrieve a wind vector from NRCS, a geophysical model function (GMF) that relates NRCS to U_{10N} is employed. All operational scatterometer GMFs are empirically-derived based on ground truth measurements (often numerical weather models) closely located in time and space to an instrument's footprint. The model function can then be used to infer the most likely wind speed and direction that would produce the NRCS observed. Typically the direction has 2 to 4 ambiguities, so an external source (such as a numerical weather model) is used to make a decision. With a few exceptions, these model functions have not been specifically developed for retrieving high wind speeds. This is generally due to a combination of the lack of ground truth and few scatterometer measurements over extreme weather events.

A persistent problem of spaceborne scatterometers is making wind vector observations through an atmosphere containing precipitation. Precipitation changes the desired signal by three means: attenuation, volume scattering, and ocean-surface modification due to the impact with the surface. These effects are not easily removed or accounted for. This problem can be somewhat mitigated by collocating a radiometer with the scatterometer for rain sensing, but all of the currently-operating spaceborne

instruments do not have this luxury. In addition, it may not be possible to put a radiometer on the same platform as a scatterometer due to power or space limitations on the satellite. The precipitation problem is generally handled by detecting and flagging rainy cells so that users of the retrievals know that they cannot be trusted to the same level as the rain-free vectors. There have been many proposals on how to better handle the problem of rain within scatterometer observations, some of which are summarized in Portabella *et al.* [3] and Weissman *et al.* [4]. Overcoming the retrieval problems that precipitation presents may be more tractable if there were a better understanding of the individual effects that rain has on backscattered power.

Besides scatterometers, imaging synthetic aperture radars (SARs) have been used to retrieve ocean surface wind vectors [5], [6]. The ability to resolve small-scale features compared to scatterometers while retaining a large swath is particularly useful. However, obtaining wind direction information from SAR images is not as straightforward as from scatterometer measurements. Despite this, SAR wind speed retrievals can augment scatterometer operation or validation. Empirical scatterometer GMFs do not exist for all polarization combinations at C- and Ku-band (e.g., C-band HH-polarization), which is how SARs retrieve wind speeds. This limits the additional utility of instruments such as RADARSAT-2, which observes all linear transmit-receive polarization combinations at C-band. As a result, some attempts have recently been made to derive polarization ratio models to convert from VV- to HH-polarization at C-band [6], [7]. These polarization ratios allow wind speed retrievals to be performed from both the VV- and HH-polarization SAR images, augmenting the geophysical data record and providing a reference for satellite scatterometer winds.

Since this dissertation relies heavily on radar measurements, a brief introduction of radar principles is presented in the next section. The section following describes a short history of satellite scatterometers, and the last section of this chapter outlines the rest of this dissertation.

1.2 Radar Operation

A radar is an active sensor that generally transmits a pulse of length τ and receives signals for a time $T - \tau$ before repeating the sequence again. The time T is the pulse repetition time (PRT) while the inverse (T^{-1}) is the pulse repetition frequency (PRF). Spaceborne Earth-observing radars deviate slightly from this description due to the distances involved: multiple pulses are transmitted followed by a long receive time, but this does not significantly change the following theory.

The simplest transmit pulse is a rectangular pulse, which is a single frequency at a constant amplitude for a fixed amount of time. The echo power from a target received by the radar is a function of the peak power and duration of this pulse. In order to reduce the amount of noise in the received signal, it should be much greater than the thermal noise of the receiver. Often physical and financial considerations limit the maximum transmit power, and practical considerations limit the transmit time, so a technique called "pulse compression" is sometimes employed to increase the signal-to-noise ratio (SNR) of weak signals. This involves transmitting a long variable-frequency "chirp" decoding the received signals in software. Knowing the properties of the transmit pulse allows a matched filter to be generated and applied to the received echoes, locating them in range with a finer resolution than is possible with a simple pulse of the same length.

Pulse compression increases the effective transmit power by an amount referred to as the compression gain. The compression gain is given by $G_C = B\tau L_W$, where B is the bandwidth of the signal and L_W is the loss imposed by the window applied to the matched filter. For a radar with $B = 4\,\text{MHz}$, $\tau = 10\,\mu\text{s}$, and a Hanning window, the compression gain is $G_C = \frac{40}{4} = 10\,\text{dB}$. This window would also reduce the measured noise power by a factor of $\frac{8}{3}$ or $4.26\,\text{dB}$ (since it is incoherent noise), so the net improvement to the SNR of the received signal is $14.26\,\text{dB}$. While some of the properties of the transmitted and received signals change with pulse compression,

the remainder of this section applies to both the simple pulse and pulse-compressed modes of operation.

If an electromagnetic wave were transmitted from an isotropically-radiating antenna, the power density S_{iso} would be

$$S_{iso}(r) = \frac{P_t}{4\pi r^2} \qquad \left(\mathrm{Wm}^{-2}\right). \tag{1.1}$$

Typically antennas are focused over a narrow volume in space. The radiated power density within this volume S' can be described in terms of the isotropic power density

$$S'(r, \theta, \phi) = G(\theta, \phi) S_{iso}(r), \tag{1.2}$$

where r is the range from the antenna, θ and ϕ are angles in orthogonal coordinate systems, and G is referred to as the antenna gain. G typically encompasses losses associated with the antenna system as well as the increase over S_{iso}, such as those incurred at the feed to the antenna and through the radome. At a distance far from the antenna, the incident power density on a scatterer is

$$S_i(r, \theta, \phi) = \frac{P_t G(\theta, \phi)}{4\pi r^2}, \tag{1.3}$$

where P_t is the power input to the antenna.

When an electromagnetic wave encounters a object, the wave is scattered away from the object. To describe this generically, it is useful to think of the scatterer in terms of the power density observed by the receiver. The object can be said to have a radar cross-section (RCS) of σ, which is defined by the power density observed at the receiver (S_r) if the incident wave were scattered isotropically:

$$S_r(r, \theta, \phi) = \frac{S_i(r, \theta, \phi)\sigma(\theta', \phi')}{4\pi r^2}. \tag{1.4}$$

θ' and ϕ' describe the direction relative to the axis created by the receiver and scatterer. The RCS is the expected backscattering cross-section per unit area.

The power received by an antenna is

$$P_r(r,\theta,\phi) = S_r(r,\theta,\phi)A_e(\theta,\phi) \qquad \text{(W)}\,, \tag{1.5}$$

where $A_e = \frac{G\lambda^2}{4\pi}$, the effective area of the antenna (at wavelength λ) from a direction given by θ and ϕ. When the transmitter and receiver use the same antenna, the received power is related to the scatterer by substituting equations (1.3) and (1.4) into (1.5):

$$P_r(r,\theta,\phi) = \frac{P_t G(\theta,\phi)^2 \lambda^2}{(4\pi)^3 r^4}\sigma. \tag{1.6}$$

For scattering from a surface, the NRCS, σ^0, can be defined as the RCS that is normalized to the area being illuminated by the antenna, A_{ill}. In scatterometry σ^0 is the parameter of interest, so this so-called radar equation is usually expressed as

$$\sigma^0 = \frac{P_r(4\pi)^3 r^4}{P_t G^2 \lambda^2 A_{ill}}. \tag{1.7}$$

1.3 A Brief History of Satellite Scatterometry

In 1973, the S-193 scatterometer flew on the Skylab satellite. S-193 was the first spaceborne scatterometer, and it provided confirmation of the theory that backscattered microwave power is related to the surface wind speed. However, it did not account for wind direction so the measurements were too scattered to determine an exact relationship [8].

In 1978, the SEASAT-A satellite was launched, carrying a radar altimeter, radiometer, SAR, and Ku-band scatterometer — the SEASAT-A Scatterometer (SASS). SASS used four fanbeam antennas, two on each side of the spacecraft track, to illuminate two 475 km swaths. Though it only collected data for 3 months, retrieved

wind speeds were shown to be accurate to $\pm 2\,\mathrm{m\,s^{-1}}$ and directions to $\pm 20^\circ$ [9] at wind speeds under $24\,\mathrm{m\,s^{-1}}$. Due to the antenna geometry, estimation of the wind direction required auxiliary meteorological information to decide between four possible solutions [10].

The ERS-1 (European Remote Sensing) satellite was launched in 1991 with a C-band scatterometer similar to the design of SASS. It used fanbeam antennas mounted to view the Earth off of one side of the spacecraft. In order to improve on the wind direction sensing of SASS, it used three antennas at 45°, 90°, and 135° off of the satellite track. The swath was approximately 500 km wide, with observed Earth-incidence angles ranging from 24° to 47° [11]. ERS-2 was launched in 1995 with the same scatterometer payload in order to maintain a continuous ocean surface wind vector data stream. ERS-1 was decommissioned in 1999 and ERS-2 was eventually decommissioned in 2011.

The NASA Scatterometer (NSCAT) flew on the Japanese Advanced Earth Observation Satellite (ADEOS)/Midori satellite in 1996. It operated for 40 weeks, when an electrical failure on the platform resulted in the loss of the spacecraft. NSCAT illuminated two 600 km swaths on either side of the ADEOS track with 3 antennas each; the outer two antennas were vertically-polarized while the middle was dual-polarized. It was another Ku-band instrument, and it retrieved winds with an accuracy of $2\,\mathrm{m\,s^{-1}}$ rms (for winds from $3\,\mathrm{m\,s^{-1}}$ to $20\,\mathrm{m\,s^{-1}}$) and $<20^\circ$ rms in direction [12].

After the premature failure of the ADEOS platform, a replacement mission was expedited and launched in 1999: the SeaWinds scatterometer on QuikSCAT[13]. The hardware for this instrument was the spare components developed for the SeaWinds scatterometer on the ADEOS-II/Midori 2 satellite, due to fly in 2003. Operating at Ku-band, it was the first spaceborne "pencil-beam" scatterometer. Its one parabolic dish antenna rotated at a rate of 18 RPM in order to observe the ocean surface from multiple directions. The vertically-polarized beam had an incidence angle of 54° and

the horizontally-polarized beam 46°. QuikSCAT was designed for a 3 year operational life, but its mission ended in November 2009 when its antenna stopped spinning [14]. During its lifetime, QuikSCAT provided marine forecasters with an invaluable tool for assessing dangers due to high winds. In December of 2000, the National Weather Service (NWS) began to issue warnings for hurricane force winds (at least 64 kt or $32.9\,\mathrm{m\,s^{-1}}$) in extratropical storms as a direct result of QuikSCAT's data frequency and quality [15]. ADEOS-II was expected to continue monitoring the global oceans, but it too experienced a catastrophic failure 10 months after its launch in 2002. The data gap would need to be filled by ERS-2 and the Advanced Scatterometer on the MetOp satellite (ASCAT), which launched in October 2006.

ASCAT on MetOp-1 continued the tradition of European scatterometers that operate at C-band (5.255 GHz) with fixed fanbeam antennas. The primary purpose of this choice was that the measurement geometry and wind retrieval process for such instruments is well-developed. Similar to SASS, NSCAT, and ERS, it has three vertically polarized antennas on each side of the spacecraft at 45°, 90°, and 135° with respect to the satellite track. The swaths cover 550 km of ocean on each side of the track. Compared to the ERS scatterometers the incidence angle range extends further out (25° to 65°), which allows for a better wind direction retrieval [16]. The second MetOp satellite launched in September 2012 and the third, and final, is planned for 2018.

The Indian Space Research Organization (ISRO) launched the Oceansat-II satellite in 2009 with a scatterometer onboard, referred to as OSCAT. It had nearly the same specifications as QuikSCAT, but due to other collocated instruments operated at a slight tilt angle. This made calibration and wind vector retrievals challenging. In April 2014, OSCAT's mission came to an end when failures in the scanning mechanism in the "main chain" and the power amplifier in the "redundant chain" proved unrecoverable.

The most recent scatterometer launched is ISS-RapidScat [17], which did so in September 2014. RapidScat is QuikSCAT hardware mounted on the International Space Station and is planned to be in operation for 24 months. Due to the different orbit of the ISS and QuikSCAT, the incidence angles are slightly higher (49° and 56° for H- and V-polarization, respectively) and the swaths are smaller.

1.4 Dissertation Outline

The remainder of this dissertation will focus on different aspects of ocean wind vector scatterometry, but all are related to improving retrievals from satellite instruments. Chapter 2 describes the instrumentation used for collecting the data presented in this dissertation. Data collected using an airborne scatterometer system developed by the Microwave Remote Sensing Laboratory (MIRSL) at the University of Massachusetts Amherst (UMass), the Imaging Wind and Rain Airborne Profiler (IWRAP), is used in each chapter. A passive microwave ocean wind speed and precipitation sensor, the Stepped Frequency Microwave Radiometer (SFMR), is also used throughout this dissertation. These and the flight experiments surrounding the data collection are described in this chapter.

Chapter 3 presents observations of the ocean by the collocated IWRAP scatterometer and SFMR at high-wind speeds. Using wind speeds retrieved by the SFMR, the IWRAP geophysical model function is extended to new incidence angles at both VV- and HH-polarizations and at C- and Ku-band. The averaging and filtering schemes for the data, such as to ensure uniform observations and rain-free measurements, are described. The equations used to model NRCS from a wind-roughened sea surface are introduced. Finally, some experimental data collected between 2011 and 2014 is developed into new geophysical model functions.

Chapter 4 investigates the effects of precipitation splash on backscatter from the ocean surface at high wind speeds. Precipitation attenuates the NRCS measured from

the ocean surface, so this effect is first removed. The IWRAP C- and Ku-band radars are used in tandem to verify the ability of SFMR to estimate precipitation. Then SFMR is used to correct attenuation of NRCS in both radars. The C- and Ku-band backscattered power in both rain and rain-free circumstances are then qualitatively compared.

Chapter 5 details an experiment performed to understand the backscatter response of the ocean at VV- and HH-polarizations for incidence angles up to 60°. The data filtering and NRCS calculation methods are described. Due to the maneuvers of the aircraft for this experiment, some special corrections to the data are performed. The NRCS response at VV- and HH-polarizations to incidence angle at from $20\,\mathrm{m\,s^{-1}}$ to $36\,\mathrm{m\,s^{-1}}$ is shown. In the same wind speed range, the polarization ratios with respect to incidence angle and wind-relative azimuth are also shown.

Lastly, chapter 6 summarizes the conclusions of each chapter and makes some recommendations on future work with the IWRAP scatterometer.

CHAPTER 2

INSTRUMENTATION AND FIELD EXPERIMENT DESCRIPTIONS

2.1 The Imaging Wind and Rain Airborne Profiler

2.1.1 System Description

The Imaging Wind and Rain Airborne Profiler (IWRAP), initially described in Fernandez *et al.* [18], is a dual-frequency conically-scanning Doppler radar developed by the Microwave Remote Sensing Laboratory (MIRSL) that is routinely installed on the National Oceanic and Atmospheric Administration (NOAA) WP-3D research aircraft. IWRAP is primarily designed as a scatterometer, to study the signature of the ocean surface under wind forcing. Two pulsed radars, one C-band and one Ku-band, scan at two incidence angles each, typically between 20° and 50°. Each radar is capable of implementing up to four simultaneous beams, however, two simultaneous beams per radar has been the normal mode of operation since 2006. The radar beam widths vary depending upon the selected incidence angle, owing to properties of the frequency-scanned antenna, but are typically in the neighborhood of 10°. The antennas are mechanically scanned in azimuth, nominally at a rate of 1 Hz. A diagram of the typical configuration of IWRAP on the aircraft is shown in figure 2.1.

The receiver front-ends of each radar differ slightly due to the sensitivity of each radar to attenuation in precipitation. Since the Ku-band radar is attenuated and scattered more by rain, the low-noise amplifier (LNA) is placed as close as possible to the antenna in order to be able to observe smaller surface echoes. So although the front-ends are similar, their implementations are described separately. The specifications of the hardware components are described in more detail in Dvorsky [19].

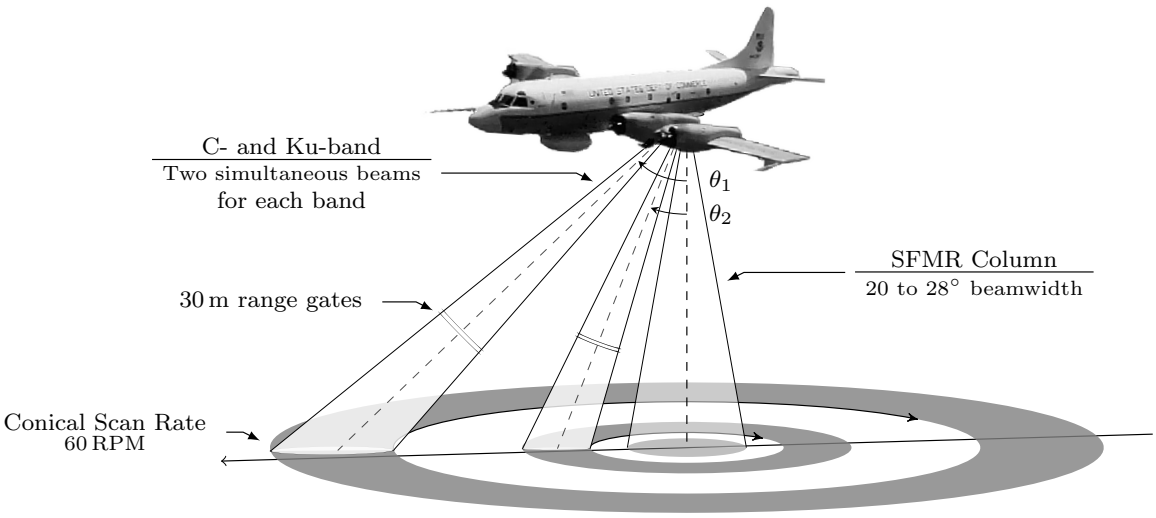

Figure 2.1. Typical configuration of the IWRAP scatterometer/profiler instrument on the NOAA WP-3D aircraft. The incidence angle, conical scan rate, transmit and receive polarizations, pulse compression mode, pulse length, and PRF, among others, are all configurable.

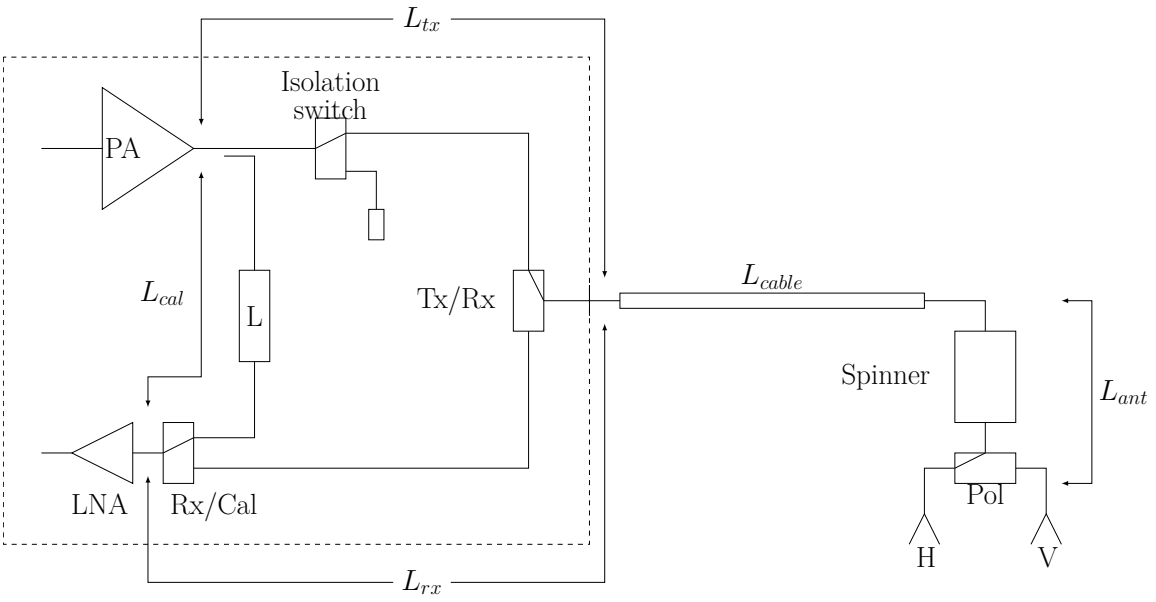

Figure 2.2. Block diagram of the IWRAP C-band front-end. The switches are configured for transmit mode. The dashed box indicates the grouping of components within a rack-mounted enclosure.

The C-band front-end, shown in transmit mode within the dashed line box in figure 2.2, is mounted near the radar operator. At the output of the power amplifier, an isolator (not shown) is connected to a 30 dB coupler, off of which the calibration pulse sample is obtained. This sample is attenuated to a level within the receiver's dynamic range and inserted into the receive chain by means of the receive/calibration (Rx/Cal) switch. This signal path is referred to as the calibration path.

When traveling through the "through" port of the coupler, also referred to as the transmit path, the signal first passes through an isolation switch. The purpose of this switch is to direct most of the transmit power into a matched load while the radar is in receive mode. This prevents noise from the power amplifier (PA) that leaks through the transmit/receive (Tx/Rx) switch from significantly contributing to the signal received from the antenna.

A low-loss cable with loss L_{cable} connects the Tx/Rx switch to a rotary joint on top of the antenna spinner. This rotary joint allows the antenna to rotate while connected to the stationary low-loss cable. A polarization switch is mounted at the bottom of the spinner assembly and is then connected to the V- and H-polarized patch antenna feeds. A slip ring allows low frequency signals and DC voltages to control the spinning polarization switch.

In receive mode, the Tx/Rx switch directs radio frequency (RF) power through the Rx/Cal switch. This switch allows the signal to pass through to the LNA and on to the transceiver, which is described below.

The Ku-band front-end is shown in figure 2.3, also in transmit mode. The bulk of the front-end is mounted below the antenna spinner, immediately above the antenna. This location puts the least amount of loss between the antenna and the LNA, resulting in a lower receiver noise figure. A radar with a low receiver noise figure can detect lower power signals. This is especially important at Ku-band due to the high

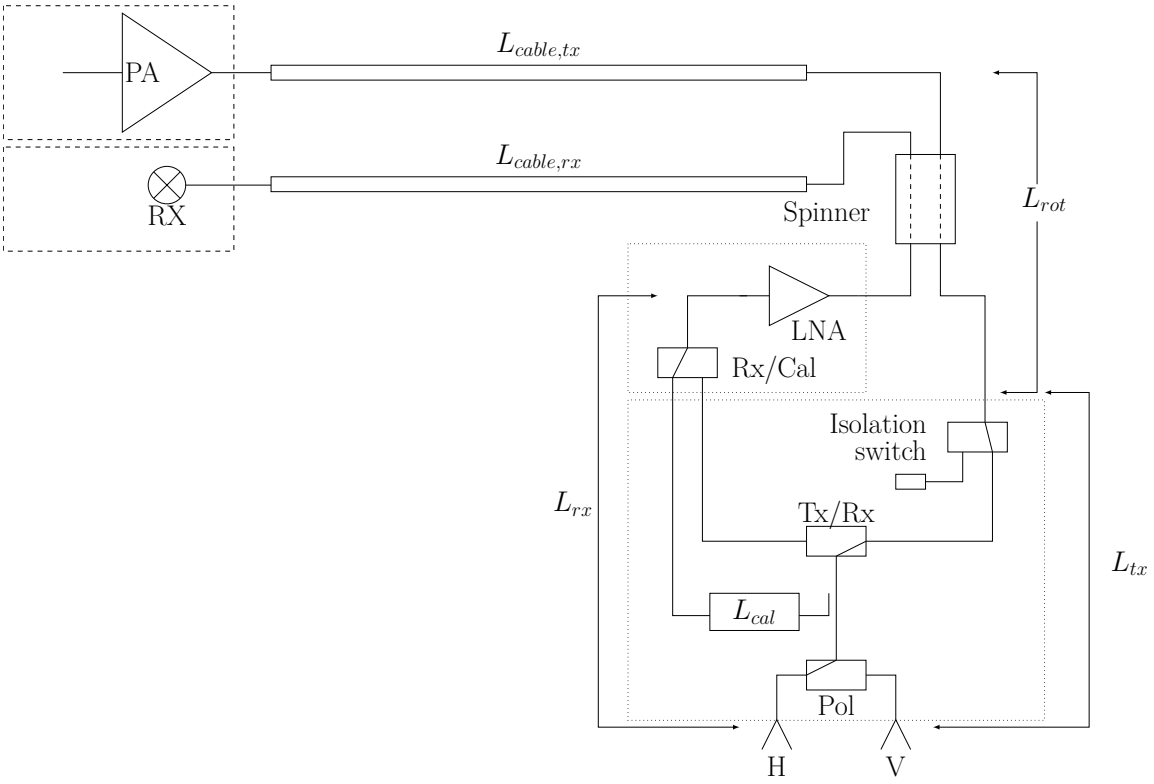

Figure 2.3. Block diagram of the current configuration of the IWRAP Ku-band front-end. The switches are configured for transmit mode. The dashed boxes indicate the grouping of components into rack-mounted enclosures, and the dotted boxes indicate components grouped into separate boxes on the front-end/antenna mounting plate.

attenuation of the received surface echo signal experienced when observing the sea surface through precipitation.

While this configuration is advantageous for measuring the surface echo, it increases the complexity of the system. Both the transmit and receive RF signals need to be separate on the rotating side of the rotary joint, so a dual-channel rotary joint is required here. The rotary joint has finite isolation that is dependent on the azimuth position of the antenna. The receiver samples the received signal with the addition of transmitter noise, less the isolation of the rotary joint. To reduce the impact of the transmitter noise, the gain of the LNA should be high enough such that the noise power from the antenna is sufficiently higher than the noise power of the transmitter when amplified by the PA. Before the 2013 hurricane season, a medium-power amplifier was installed following the LNA (not shown in figure 2.3) to achieve the necessary gain level while retaining a low noise figure. To minimize losses, the Ku-band system employs two low-loss cables running from the rotary joint to the PA and receiver input.

After each front-end the RF signals are fed to the transceiver, which is where the RF signals are converted to intermediate frequency (IF). This block is also where, on transmit, the IF is mixed up to RF before the PA. The block diagrams of the transceivers are shown in figures 2.4 and 2.5 for C-band and Ku-band, respectively. On transmit, each RF source is mixed with a 30 MHz single-sideband mixer. The lower sideband is passed on to the "Transmit RF" (or "Tx RF") switch, which is only active during transmit time, resulting in a transmitted frequency 30 MHz below the RF source. This Tx RF switch reduces the PA output during receive, so leakage through the calibration loop and Cal/Rx switch does not compete with the received signal. The remainder of the transmit path is radar-dependent, as described above.

On receive, the RF signal is split and mixed down to 30 MHz IF. The mixers use the same RF source as the transmit stage, which is split by a power divider.

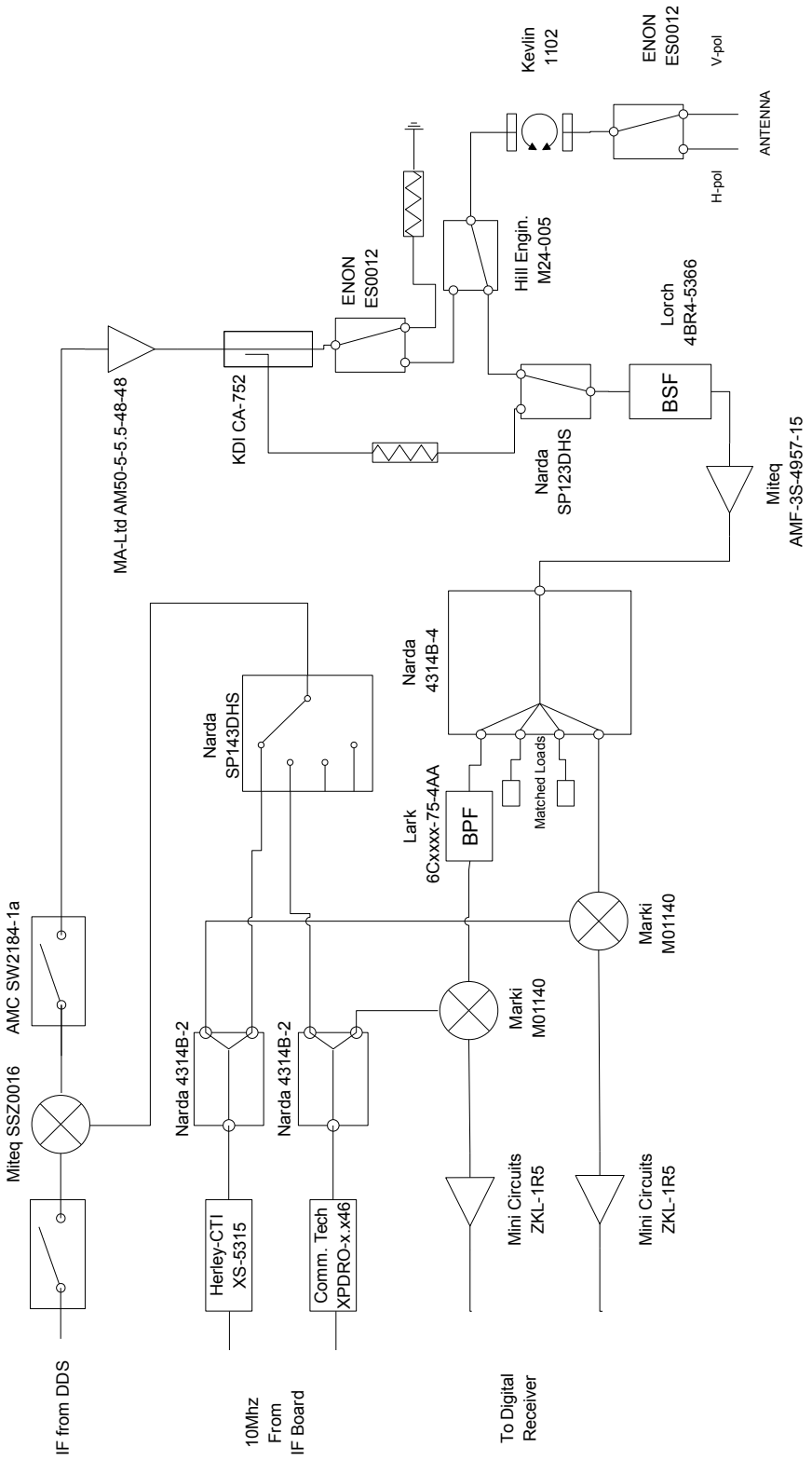

Figure 2.4. Block diagram of the current IWRAP C-band transceiver and front-end. The switches are configured for receive mode. The RF portion is also shown in figure 2.2.

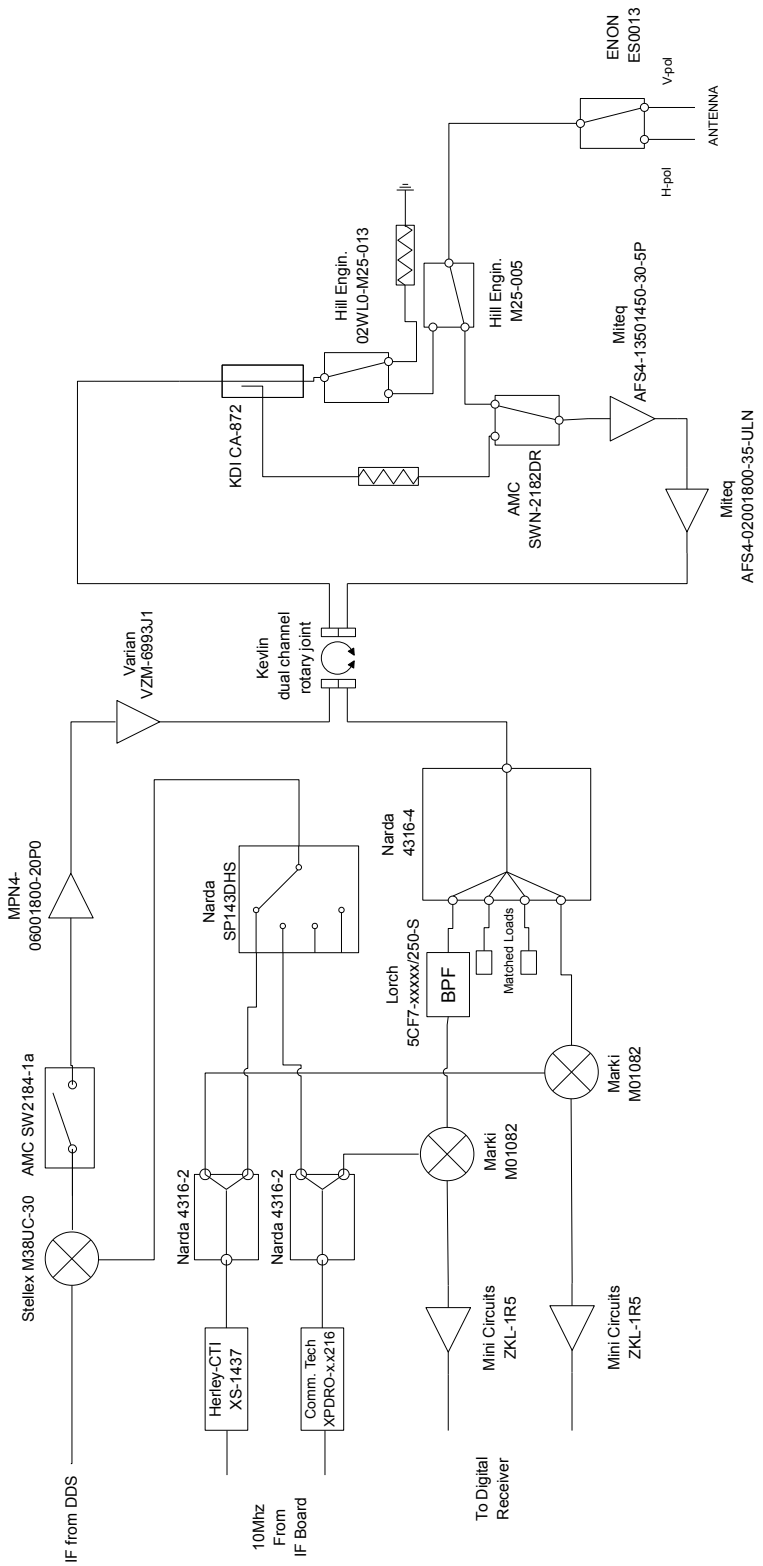

Figure 2.5. Block diagram of the current IWRAP Ku-band transceiver and front-end. The switches are configured for receive mode. The RF portion is also shown in figure 2.3.

Recall that each incidence angle is transmitted at a different frequency, so this step effectively separates incidence angles into different channels at IF. An IF amplifier then boosts each signal to be within the dynamic range of the digital receiver (DR). In-phase and quadrature components of the IF signal are sampled at a rate of 5 MHz, which makes each so-called range gate in the radar profile 30 m long. The receiver bandwidth is limited to 5 MHz by the bandpass filters in front of the DR, which are not shown in the diagrams.

2.1.2 Summary of System Changes

Since IWRAP was first introduced in 2005 [18] the instrument has been deployed on the NOAA WP-3D twice per year each year, with the exception of 2008. The experiments are separated into two seasons per year: hurricane season, with flights generally between August and October, and winter season, with flights generally during January and February. In 2008, there was no winter season. The NOAA Aircraft Operations Center (AOC) operates two WP-3D aircraft, N42RF and N43RF, and IWRAP has been installed on both. Here the experiments used in this dissertation and some of the major changes in the IWRAP subsystems since 2005 are described.

2.1.2.1 Changes to the Location of the Ku-band Front-End

Between winter 2007 and hurricane season 2007, the Ku-band front-end was moved closer to the antenna in order to improve the sensitivity of the Ku-band system [20]. Effectively, the two dotted boxes in figure 2.3 were moved from above the rotary joint to below the rotary joint. Since IWRAP could only measure co-polarized backscatter at the time, only one cable ran from the front-end to a single-channel rotary joint. An additional cable and a dual-channel rotary joint was required for this upgrade.

As mentioned in section 2.1.1, at Ku-band frequencies (12 GHz to 14 GHz) there are significant scattering and attenuation effects in precipitation. Hurricane eyewalls often contain strong rain bands, which were observed to be severe enough to attenuate

the surface echo beyond the receiver noise floor [20], [21]. The receiver noise floor is described by

$$P_n = kTBF_{rec}, \tag{2.1}$$

where k is the Boltzmann constant, $T = 290\,\mathrm{K}$, B is the receiver bandwidth (5 MHz), and F_{rec} is the receiver noise figure. In order to lower the noise floor, the noise figure F_{rec} must be reduced. The noise figure of a system with multiple gain and noise stages is

$$F_{rec} = F_1 + \frac{F_2 - 1}{G_1} + \frac{F_3 - 1}{G_1 G_2} + \ldots + \frac{F_N - 1}{\prod_{i=1}^{N-1} G_i}, \tag{2.2}$$

where G_i and F_i are the gain (or inverse loss) and noise figure, respectively, of the ith stage. The first component has the most significant impact on the total receiver noise figure. By reducing the loss of the first stage after the antenna, terms 2 through N become smaller. Along with replacing the LNA with one that has a smaller noise figure, locating the LNA closer to the antenna than the long cable (with loss of L_{cable}) more than doubled the range capability of the Ku-band system in precipitation.

2.1.2.2 Pulse Compression

Since hurricane season 2008, IWRAP has been capable of using a pulse-compressed transmit/receive mode [22], [23]. This provides better sensitivity to low surface wind speeds or rain-attenuated surface echoes, but it significantly increases the blind range of the radar. For example, the standard 200 ns pulse has a blind range of 30 m while a 10 µs chirp has a blind range of 1.5 km. The blind range is generally not a problem except when IWRAP is used as a rain profiler or when the aircraft is flown close to the ocean surface. However, only the outer incidence angle is chirped, leaving the inner channel pulsed for rain profiling. Additionally, pulse compression is only used when operating IWRAP at altitudes above 2 km to avoid issues with the blind range.

2.1.2.3 Dual- and Cross-Polarization

Prior to hurricane season 2010, IWRAP was only able to measure one co-polarized backscatter channel (VV or HH) at a time. This was primarily due to the use of single-polarization antennas and lack of a switch on the dual-polarized antennas. Since then, IWRAP has been capable of changing its polarization configuration during the flight, allowing for measurement of VV-polarization, HH-polarization, or both in a time-multiplexed mode [19].

Before the 2011 hurricane season, the polarization switch logic and hardware were also upgraded to make IWRAP capable of receiving a different polarization than it transmits. This has allowed time-multiplexed co-polarized and cross-polarized measurements (i.e., switching between VV-pol and VH-pol after a fixed number of profiles). While the ability to sample cross-polarized sea-surface normalized radar cross-section (NRCS) is promising, opportunities to make observations have been limited to date. The low isolation of the antenna (estimated from antenna patterns to be 10 dB to 12 dB) requires high wind speeds in order for the weaker cross-polarized signal to overcome the leakage of the co-polarized backscatter from the other antenna.

2.1.2.4 Software-Configurable Incidence Angles

As mentioned in section 2.1.1, IWRAP usually operates with two simultaneous incidence angles. Starting with the winter season of 2011, the frequencies dictating the outer incidence angles on the radars have been generated by compact programmable synthesizers [19]. These sources are limited in frequency range (4.9 GHz to 5.5 GHz at C-band and 12.2 GHz to 13.5 GHz at Ku-band), but they span the range over which the antenna was designed. The synthesizers require a few milliseconds to be programmed, which makes them not feasible for frequency hopping sampling techniques. The inner incidence angles continue to be generated by dielectric resonator oscillators (DROs), which are fixed-frequency sources. After this season the DROs and

frequency settings of the synthesizers have generally remained the same, resulting in several seasons of data at the same incidence angles.

2.1.2.5 Calibration and Digital Receiver Improvements

Prior to the 2012 winter storm season, the Ku-band calibration loop coupler (labeled L_{cal} in figure 2.3) was located between the bottom of the rotary joint and the isolation switch. Since the goal of the calibration loop is to sample as much of the transmit path as possible, the coupler was moved to its present location.

Dvorsky [19] describes a persistent issue with measuring the Ku-band calibration pulse: an azimuth-dependent isolation that is small enough to affect the calibration pulse. The potential for this problem was recognized by Chu [20] when the Ku-band front-end was first moved. It can be addressed with either more isolation between rotary joint channels, as was initially done, or more amplification on the receive rotary joint channel. As mentioned in section 2.1.1, a medium-power amplifier was installed following the LNA before the 2013 hurricane season. This was done for economical and practical purposes, since it avoids needing a Ku-band dual-channel rotary joint with extreme isolation requirements.

Between the winter and hurricane seasons of 2013, the digital receiver was upgraded from a Pentek 7131 to an Ettus Research USRP N210. The Pentek 7131 is a two-channel digital receiver with a PCI interface. The model used in the IWRAP system has two 14-bit analog-to-digital converters (ADCs) that sample at 80 MHz. It has a user-configurable Xilinx Virtex-II XC2V1000 field-programmable gate array (FPGA), but this feature was never used. The onboard TI/Graychip GC4016 digital downconverters were combined in pairs to obtain a 5 MHz bandwidth for each IF input. Raw I/Q data from the Pentek card is streamed to the host computer via the PCI bus. The USRP N210 is a two-channel software-defined radio with a Xilinx Spartan 3A-DSP 3400 FPGA, 100 $\mathrm{MS\,s^{-1}}$ dual ADC, and 400 $\mathrm{MS\,s^{-1}}$ dual digital-to-analog

converter (DAC). Raw I/Q data is streamed to the host computer over a Gigabit Ethernet interface.

The most significant aspect of this upgrade is that the IWRAP system is now able to properly sample the polarization switch state and antenna position associated with a profile. Compared to the Pentek FPGA, the Ettus system is also more easily modified. The primary accomplishment was to sample these switch states and insert them into the raw data. With the Pentek system, profile samples are buffered so any sampling of the switch or encoder by user space software is not matched in time with the profile. As a result, the polarization state in previous years was determined from the amplitude of the backscattered power. The control over the FPGA configuration also allowed the implementation of a profile counter in the sampling hardware.

2.2 The Stepped Frequency Microwave Radiometer

C-band radiometers have been used on aircraft for measuring high-speed ocean surface winds since 1980. Jones *et al.* [24] describes the Langley Research Center (LRC) Stepped Frequency Microwave Radiometer (SFMR), which was flown twice through Hurricane Allen on a NOAA C-130 aircraft in 1980. This instrument was used to develop an early algorithm for remotely retrieving ocean surface wind speed (at a height of 20 m). LRC SFMR was a nadir-pointing microwave radiometer operating at either two or four frequencies in the C-band, depending on the user configuration. The variation of the ocean surface and atmosphere under the aircraft allows for retrieval of surface wind speed and mean rainfall rate within the beamwidth the radiometer antenna.

The theory behind ocean wind sensing via microwave radiometry relies on the fact that all objects emit electromagnetic radiation. A perfect absorber of electromagnetic radiation is called a blackbody; being a perfect absorber also means that it is also a perfect emitter when the object is in thermodynamic equilibrium. An ideal antenna

with bandwidth B that observes only a blackbody at a temperature T can be shown to yield an output power

$$P_{bb} = kTB, \tag{2.3}$$

where k is the Boltzmann constant ($1.38 \times 10^{-23}\,\mathrm{J\,K^{-1}}$) [25]. Note that this is the same output power as is measured at the terminals of a noisy resistor at temperature T. The power available at this ideal antenna's output terminals is determined by the physical temperature of the blackbody. Since no blackbodies exist in reality, a blackbody equivalent radiometric temperature can be defined for a scene observed by an antenna. This equivalent temperature is called the brightness temperature ($\mathrm{T_b}$).

The brightness temperature of the ocean surface can be described as

$$\begin{aligned} T_{b,ocean} = &\left(\epsilon_{ocean} \cdot \mathrm{SST} + (1 - \tau_{atm})\ T_{down}\right)\ \tau_{atm} \\ &+ (1 - \tau_{atm})\ T_{up}, \end{aligned} \tag{2.4}$$

where ϵ_{ocean} is the emissivity of the ocean, SST is the sea-surface temperature, and τ_{atm} is the transmissivity of the atmosphere. The first term of (2.4) is the energy from the ocean surface (both ocean and anything covering the surface) and the reflected downwelling energy from the atmosphere ($T_{atm,down}$). The second term is the upwelling energy from the atmosphere ($T_{atm,up}$). Contributions to $\mathrm{T_b}$ from the atmosphere at the frequencies of interest in are largely due to water, both precipitating and non-precipitating.

The ocean surface influences $\mathrm{T_b}$s in two parts: the emissivity of the ocean at nadir, which is a function of SST, salinity, and frequency [26], and the so-called excess emissivity due to wind forcing. At higher wind speeds (greater than $15\,\mathrm{m\,s^{-1}}$) the excess emissivity, which is a frequency-dependent function of fractional foam coverage within the beamwidth of the instrument, is a stronger component than the smooth-surface nadir emissivity. At lower wind speeds there is little to no foam coverage. The foam covering the ocean surface in the open ocean results from breaking surface

gravity waves, which is more related to wave energy dissipation, but not necessarily wind energy input [27]. As a result, microwave emissions from the ocean surface depend on the sea state to some extent. Uhlhorn and Black [28] noted an error in wind speed retrievals from a microwave radiometer in hurricanes of about $2.5\,\mathrm{m\,s^{-1}}$, depending on the quadrant of the tropical cyclone (TC) sampled. They attribute this error to the difference in sea state in these quadrants.

After LRC SFMR, the University of Massachusetts Amherst (UMass) developed a dual-polarization, multi-frequency microwave radiometer named the Simultaneous Frequency Microwave Radiometer (SFMR2), first operated in 1999 [29]. Also a C-band instrument, SFMR2 simultaneously sampled each frequency (4.63 GHz, 5.50 GHz, 5.92 GHz, 6.34 GHz, 6.60 GHz, and 7.05 GHz) at a rate of 20 Hz. T_bs were first measured with this instrument from within TCs from a NOAA WP-3D aircraft in the fall of 1999. In 2000, the digital acquisition and switching systems within the instrument were upgraded and subsequently used by Fernandez *et al.* [30] to develop a geophysical model function (GMF) for C- and Ku-band scatterometers. The measurement precision (ΔT) of the SFMR2 is approximately 0.4 K. Fernandez *et al.* [30] averaged T_bs to 1 Hz, resulting in a ΔT of less than 0.1 K. After 2006, when SFMR was declared a national need, SFMR2 was not used regularly. It was repaired in 2009 in preparation for deployment alongside IWRAP and SFMR during the 2010 IWRAP winter season experiments. Besides some repairs in hardware, the most significant change was in transitioning the operating system from Microsoft Windows to a GNU/Linux distribution. Linux kernel modules were written to use the relatively old hardware with a then-modern kernel (in the 2.6 series), and sampling software was created in C based on the existing design in Visual Basic. Though measurements were taken during several flight experiments in the winter of 2010, it does not offer much benefit over the SFMR already installed on both NOAA WP-3D aircraft and has not been used since.

AOC operates a SFMR, developed by ProSensing, Inc. of Amherst, MA based on the design concepts of LRC SFMR. It is also a C-band nadir-pointing microwave radiometer, but it steps through six frequencies (4.74 GHz, 5.31 GHz, 5.57 GHz, 6.02 GHz, 6.69 GHz, and 7.09 GHz), dwelling at each for 0.5 s [31]. This instrument is installed on each of the NOAA WP-3D aircraft and is referred to as simply "the SFMR" hereafter. The receiver channel bandwidth is 100 MHz and the instrument has a precision of 0.5 K.

In order to develop an algorithm for retrieval, surface wind ground truth is required to map T_bs to wind speed. The reference wind speeds used to develop the algorithm for LRC SFMR were from a NOAA WP-3D flying at 450 m to 1500 m, extrapolated to a 20 m height. LRC SFMR used the brightness temperatures measured at both four and two frequencies in order to retrieve wind speed and rain rate. This algorithm was the basis of the 2003 algorithm for the SFMR, which was developed using flight-level wind speeds extrapolated to the surface and global positioning system (GPS) dropwindsondes as the ground truths [28]. In 2007, Uhlhorn *et al.* [27] revised the GMF relating excess emissivity to surface wind speed. This relationship is a critical part of retrieving wind speeds and rain rates from the SFMR; Uhlhorn *et al.* [27] found that the 2003 algorithm overestimated high wind speeds. Selected aspects of the current SFMR GMF are shown in figure 2.6. The left panel shows the change in T_bs as a function of wind speed only, the center panel shows the same as a function solely of rain rate, and the right panel shows the T_b response to SST.

The retrieval algorithm for SFMR is currently only reliable at nadir incidence. As a result, in this work retrievals are only used from data collected from incidence angles within $\pm 3^\circ$. Retrieval accuracy is dependent on the accuracy of the T_b measurements, the surface emissivity GMF, accuracy of the assumptions made about the atmosphere and ocean state, and the SFMR GMF. Any bias in T_b affects retrieved wind speed and rain rate, with the degree depending on the surface wind speed. Before beginning

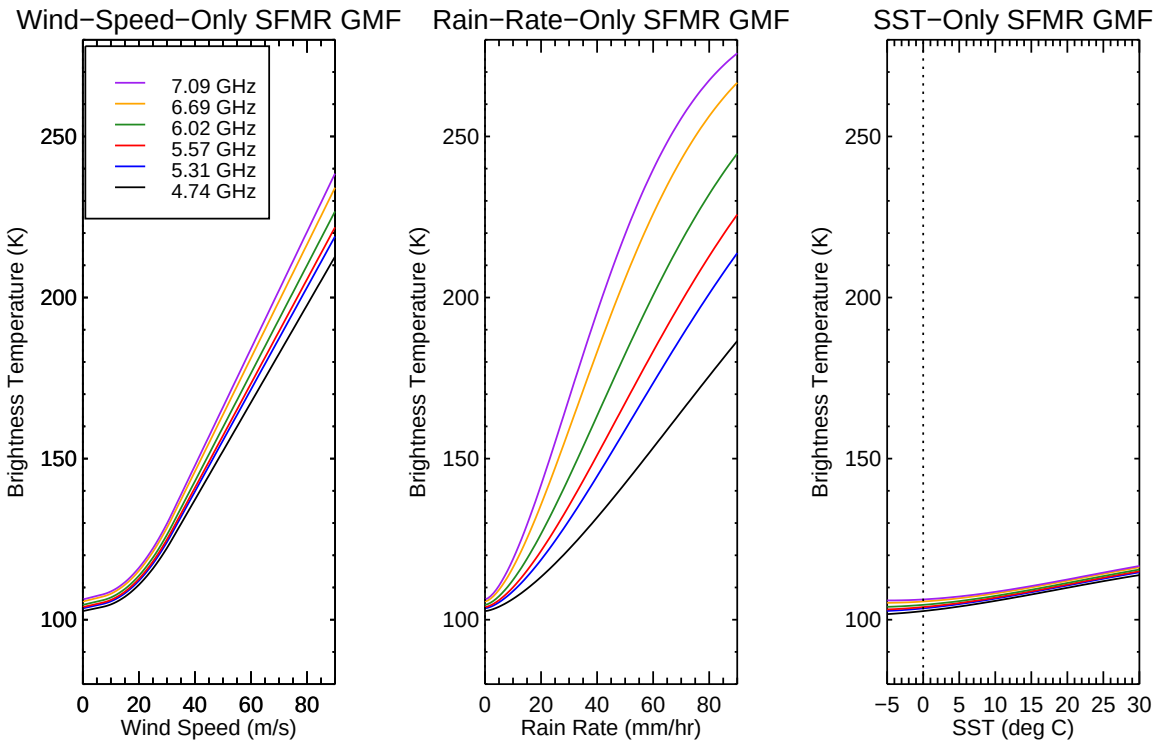

Figure 2.6. SFMR GMF developed by Uhlhorn and Black [28]. The left panel shows the change in T_bs as a function of wind speed only. The center panel shows the same as a function solely of rain rate. The right panel shows the T_b response to SST.

a season of experiments that use the SFMR, AOC will perform a calibration flight in an attempt to remove T_b biases. T_bs provided by AOC SFMR are used, assuming they have been, and remain throughout the season, well-calibrated. However, the retrievals are performed again after taking some additional steps. Removal of any residual biases of the observed T_bs with respect to the GMF are attempted first. Usually these biases are on the order of less than 1 K. Any T_b channels contaminated by RFI are omitted from the retrieval process. Finally, SST and salinity models are used as inputs to the emissivity GMF. The resulting retrievals serve as the ground truth for the rest of this dissertation.

2.3 Experiment Descriptions

In section 2.1.2, it was noted that since hurricane season 2011, the incidence angles on both the C-band and Ku-band radars have generally been the same. For this dissertation, flight experiments have been selected from between hurricane season 2011 and hurricane season 2014 that exhibit reasonable behavior of NRCS and SFMR wind speed. Additionally, as will be described in chapter 3, rain-free data at high wind speeds are needed in order to calibrate the NRCS in each flight. So the flight experiments must be filtered further so that only flights that can be calibrated are used. The following is a brief description of these flight experiments.

Although the 2011 hurricane season was an active storm season, there were not many opportunities for data collection. Between installing the equipment later than usual and problems with the aircraft, there were only three storm flights during the season. Two of these flights did not have much high-wind data, so only the flight through Hurricane Hilary in the East Pacific was used. Since most of the time was spent investigating the cross-polarization capabilities of the system, there is not much HH-polarized data from this flight.

During the 2012 winter season, IWRAP flew in the North Atlantic out of Halifax, NS, Canada. The Ku-band radar was not functioning for a few of the early flights, so there is more C-band data from this season than Ku-band. Much of this season was also devoted to operating IWRAP in alternating VV- and VH-polarization modes, so HH-polarized data at the higher wind speeds is lacking.

In the hurricane season of 2012, IWRAP was operated in two storm systems: Leslie and Sandy. These were both low-wind systems, as the aircraft was only able to reach Leslie while it was transitioning to a tropical storm. And though Sandy was called a hurricane, this was primarily for public safety purposes. During most of the time in the storm, the wind speeds were not above hurricane force. Sandy was unique in that it had large fields of relatively uniform winds, much like the winter storm systems. However, there was much more precipitation than in the typical winter storm. IWRAP observed a wide range of stratiform rain, sometimes even observing graupel. During the first flight through Sandy, the Ku-band system was non-operational.

In winter 2013, IWRAP flew again out of Halifax, NS. Though instrumentation problems cropped up occasionally, two of the flights over the Labrador Sea (January 23 and February 2) encountered surface winds over $25\,\mathrm{m\,s^{-1}}$. During one of these flights winds up to about $43\,\mathrm{m\,s^{-1}}$ were observed, which is the strength of a Category 2 hurricane.

During the hurricane season of 2013, IWRAP was flown through three different systems: Gabrielle, Ingrid, and Karen. Of the three, only Ingrid made it to hurricane status; it was almost strong enough to be in Saffir-Simpson Category 2 [32]. Gabrielle was a very disorganized and weak storm with a significant amount of precipitation. In fact, it lost tropical storm status in the second of the three missions flown through it. Because of the low winds the data were unable to be calibrated, so they are not used for this work. The first flight through Ingrid when it was a tropical storm suffered from the same circumstances. Tropical Storm (TS) Karen was characterized by low winds

and significant rain, resulting in little usable data for this dissertation. Therefore, only data from Hurricane Ingrid is used here.

The 2014 winter season was once again out of Halifax, NS. IWRAP generally observed rain-free conditions with winds in the $20\,\mathrm{m\,s^{-1}}$ to $30\,\mathrm{m\,s^{-1}}$ range. However, one of the challenges with relying on SFMR in the winter is that the retrieval algorithm does not work reliably when crossing steep SST gradients. As this was an issue this year, some flights from this season were omitted.

Effectively all of the hurricane 2014 season was able to be used for this dissertation, with the exception of flights before and after hurricanes. The season started off with a flight through AL96, which would turn into Hurricane Cristobal on August 26. Flights through Hurricane Edouard on September 15 and 16 presented the highest winds observed by IWRAP since before 2011, with wind speeds exceeding $40\,\mathrm{m\,s^{-1}}$ according to SFMR. However, Hurricane Gonzalo on October 16 and 17 had winds exceeding even Edouard, reaching $50\,\mathrm{m\,s^{-1}}$ (Category 3). At these high winds IWRAP was configured to operate in VV/VH mode, meaning they alternated between the two polarization configurations after a set number of profiles. This means that there is less HH-polarized data at the highest wind speeds. Additionally, some of the highest winds were contaminated by rain. Despite these limitations, this season provided most of the data at the high end of the wind speed range observed in all seasons, near $45\,\mathrm{m\,s^{-1}}$.

CHAPTER 3

HIGH-WIND-SPEED RAIN-FREE GEOPHYSICAL MODEL FUNCTION IMPROVEMENT

3.1 Introduction

Radar scatterometers are used to remotely sense ocean surface wind vectors. These instruments have traditionally operated in the C-band (4 GHz to 8 GHz) and Ku-band (12 GHz to 18 GHz). Since 2003, the Microwave Remote Sensing Laboratory (MIRSL) at the University of Massachusetts Amherst (UMass) has regularly operated an airborne scatterometer, the Imaging Wind and Rain Airborne Profiler (IWRAP), that utilizes both frequency bands [18]. MIRSL has a data archive from this instrument dating back to 2005.

Ocean vector wind retrievals are based on the normalized radar cross-section (NRCS), or σ^0, measured from the ocean surface. NRCS is typically modeled by the function

$$\begin{aligned}\sigma^0\left(U_{10N},\theta,\chi,p,\lambda\right) =& A_0\left(U_{10N},\theta,p,\lambda\right)\\ &+ A_1\left(U_{10N},\theta,p,\lambda\right)\cos\chi\\ &+ A_2\left(U_{10N},\theta,p,\lambda\right)\cos 2\chi,\end{aligned} \tag{3.1}$$

where χ is the wind-relative azimuth angle, θ is the incidence angle, p is the polarization, and λ is the wavelength. The geophysical model function can be used to retrieve the most likely wind speed and direction that would produce the NRCS observed.

(3.1) can also be written

$$\sigma^0 = A_0 \left(1 + a_1 \cos\chi + a_2 \cos 2\chi\right) \tag{3.2}$$

to eliminate the influence of A_0 on the higher harmonics during analysis. While the general shape of this model fits the geophysical response of the ocean surface in NRCS, the model does not match well its minima with the physical crosswind directions (90° and 270° azimuth). The locations in azimuth of the minima of the model depend on the amplitudes of both the A_1 and A_2 terms. These locations are determined by minimizing the derivative of (3.1):

$$\frac{d\sigma^0}{d\chi} = -A_1 \sin\chi - 2\,A_2 \sin 2\chi. \tag{3.3}$$

The locations of NRCS minima (where (3.3) is 0) are at the azimuth

$$\chi_{min} = \cos^{-1}\left(\frac{-A_1}{4\,A_2}\right), \tag{3.4}$$

and $360° - \chi_{min}$.

A_0 is the mean term and has a strong response to wind speed. A_1 controls the upwind/downwind anisotropy; the difference between upwind and downwind peaks (in linear units) is $2A_1$. A_1 and A_2 combine to control the upwind/crosswind difference, assuming crosswind is at χ_{min}:

$$\sigma^0_{up} - \sigma^0_{cross} = \frac{\left(A_1 + 4A_2\right)^2}{8A_2} = A_0 \frac{\left(a_1 + 4a_2\right)^2}{8a_2}. \tag{3.5}$$

If a_1 is small relative to a_2, then (3.5) becomes $2A_2$.

The parameterization of the A_0, A_1, and A_2 terms from (3.1) is chosen following the formulation in [30]:

$$\begin{aligned} A_0\left(U_{10N},\theta,p\right) = 10^{\beta(U_{10N},\theta,p)} &\cdot \left[U_{10N}\right]^{\gamma_0(U_{10N},\theta,p)} \\ &\cdot \left[U_{10N}\right]^{\gamma_1(U_{10N},\theta,p)\cdot\log(U_{10N})} \\ &\cdot \left[U_{10N}\right]^{\gamma_2(U_{10N},\theta,p)\cdot\log^2(U_{10N})}, \end{aligned} \tag{3.6}$$

$$\begin{aligned} A_1\left(U_{10N},\theta,p\right) = A_0\left(U_{10N},\theta,p\right)\cdot[\, &c_0\left(U_{10N},\theta,p\right) \\ &+ c_1\left(U_{10N},\theta,p\right)\cdot U_{10N} \\ &+ c_2\left(U_{10N},\theta,p\right)\cdot U_{10N}^2\,], \end{aligned} \tag{3.7}$$

$$\begin{aligned} A_2\left(U_{10N},\theta,p\right) = A_0\left(U_{10N},\theta,p\right)\cdot[\, &d_0\left(U_{10N},\theta,p\right) \\ &+ d_1\left(U_{10N},\theta,p\right)\cdot U_{10N} \\ &+ d_2\left(U_{10N},\theta,p\right)\cdot U_{10N}\cdot\tanh\left(\frac{U_{10N}}{d_3\left(U_{10N},\theta,p\right)}\right)], \end{aligned} \tag{3.8}$$

where U_{10N} is the 10 m equivalent neutral wind speed, θ is the incidence angle, and p is the polarization. The dependence of all these parameters on frequency band is implied. Expressed in decibel units, (3.6) may be written

$$\begin{aligned} A_0\left(U_{10N},\theta,p\right) = 10\cdot[\,&\beta + \gamma_0\left(U_{10N},\theta,p\right)\log\left(U_{10N}\right) \\ &+ \gamma_1\left(U_{10N},\theta,p\right)\log^2\left(U_{10N}\right) \\ &+ \gamma_2\left(U_{10N},\theta,p\right)\log^3\left(U_{10N}\right)\,]. \qquad \text{(dB)} \end{aligned} \tag{3.9}$$

The convention in the remainder of this document will be for A_0 to be expressed in dB units while A_1 and A_2 are in linear units.

With a few exceptions, scatterometer geophysical model function have not been specifically developed for high wind speed operation. A high-wind-speed GMF was developed in 2006 by Fernandez *et al.* [30] (hereafter referred to as the IWRAP GMF). They used data from the IWRAP airborne scatterometer in C-band and Ku-band at VV- and HH-polarization, along with surface wind speed retrievals from Stepped Frequency Microwave Radiometer (SFMR) as a reference. The data was collected from 10 hurricanes between 2002 and 2003 in wind speeds from $25\,\mathrm{m\,s^{-1}}$ to $65\,\mathrm{m\,s^{-1}}$. One of the notable observations of this work was a saturation in the backscatter response at high wind speeds: beyond a certain wind speed, the NRCS does not increase. Additionally, the HH-pol NRCS at high incidence angles appears to be the co-pol configuration that saturates at the highest wind speeds, making it a good choice for high-wind-speed retrievals.

The CMOD5.n model function [33] was developed as the latest adjustment in a long history of C-band VV-polarization model functions in the CMOD family [34]. CMOD5 is claimed to increase the maximum wind speed capability of the GMF to $35\,\mathrm{m\,s^{-1}}$ [35]. The most recent revision, CMOD5.n was developed to remove an observed $0.5\,\mathrm{m\,s^{-1}}$ underestimation of wind speed retrievals from the ERS scatterometer.

Soisuvarn *et al.* [36] developed a hybrid model function based on CMOD5.n and the saturation wind speed of the IWRAP GMF. In order to improve retrievals from ASCAT at wind speeds above $10\,\mathrm{m\,s^{-1}}$, they modified the wind speed response of the azimuthal mean term of CMOD5.n. They did not alter the performance of the GMF below $10\,\mathrm{m\,s^{-1}}$ or the directional retrieval accuracy. By requiring saturation in the GMF, disagreement with QuikSCAT and WindSat retrievals at wind speeds above $15\,\mathrm{m\,s^{-1}}$ was reduced.

Ricciardulli and Wentz [37] used data from the SeaWinds scatterometer on QuikSCAT to develop the Ku-2011 GMF at Ku-band. QuikSCAT operated at both VV and HH polarizations, each with a different incidence angle: 53° at VV-polarization and 46° at

HH. They used 7 years of rain-free winds from the WindSat polarimetric radiometer as ground truth wind speeds [38] to calibrate the scatterometer between $20\,\mathrm{m\,s^{-1}}$ and $30\,\mathrm{m\,s^{-1}}$.

With the exception of the IWRAP GMF, these model functions were designed for use at the low end of the wind speed range observed in this dissertation. Despite this, they are the closest GMFs that exist for comparison with high-wind data.

3.2 Adjustment to the Wind Speed Dependence of the IWRAP Geophysical Model Function

When the IWRAP GMF was originally developed, it used wind speeds retrieved from SFMR2 as its ground truth. In 2007, after the IWRAP GMF was developed, an adjustment was made to the SFMR excess emissivity model to correct an observed low bias at extreme wind speeds and a high bias lower than about $58\,\mathrm{m\,s^{-1}}$. The model developed in 2003 is a quadratic wind-speed-dependent model while the 2007 model is quadratic only between $7\,\mathrm{m\,s^{-1}}$ to $31.9\,\mathrm{m\,s^{-1}}$. Outside of this range it is linear. Figure 3.1 illustrates the change in retrieved wind speed due to the different emissivity model. The solid line shows the 2003 wind speed retrievals for the equivalent retrievals with the 2007 model. Additionally, AOC obtained its own SFMR for operational use on the WP-3D aircraft, making SFMR2 somewhat redundant.

In order to correct the IWRAP GMF for this adjustment to the wind speeds it depended on, the following algorithm was performed for each coefficient in (3.1) (note the term "vector" is used in the sense of linear algebra here):

1. Generate a vector of wind speeds from $25\,\mathrm{m\,s^{-1}}$ to $65\,\mathrm{m\,s^{-1}}$ in increments of $5\,\mathrm{m\,s^{-1}}$ (the "true" wind speed);

2. Compute T_bs for this vector of wind speeds (with all other parameters fixed) using the new excess emissivity GMF;

3. Perform wind speed retrievals from these T_bs using the 2003 model;

4. Compute the scatterometer GMF coefficients for these retrievals using the existing IWRAP GMF;

5. Perform a least-squares fit to these coefficients using the "true" vector of wind speeds as the dependent variable.

For the adjustment to a_2, the d_3 parameter was held constant since these were stated to have been obtained from Donnelly *et al.* [39] (though the d_3 parameter at the lowest incidence angle at each radar seems to have been interpolated from the values at the lowest two incidence angles). The final parameters obtained as a result of applying this correction are shown in tables 3.1 to 3.3. The GMF change is illustrated in figure 3.2. Note that the overestimation of wind speeds below approximately $58\,\mathrm{m\,s^{-1}}$ resulted in an increase in the NRCS as a function of wind speed and vice versa for winds above $58\,\mathrm{m\,s^{-1}}$. This correction likely also modifies the saturation wind speed at each polarization and incidence angle, but these values were not derived again.

3.3 Variability and Calibration Methods

Normalized radar cross-section of the ocean surface measured by a scatterometer varies from one pulse to the next. However, the sampled NRCS also changes with respect to SFMR wind speed during flights, between flights, and between seasons despite accounting for system changes through external calibration of the IWRAP radars. Figure 3.3 shows the NRCS as a function of SFMR wind speed from four flights during the 2014 hurricane season. The data are from the 47.4° VV-polarization C-band radar channel. The solid lines are means for each season (with one composite mean) with standard deviations shown as the error bars. The differences between data points within the same wind speed bin and between each flight are explained by variability in any of four categories: statistical variability, geophysical variability, calibration

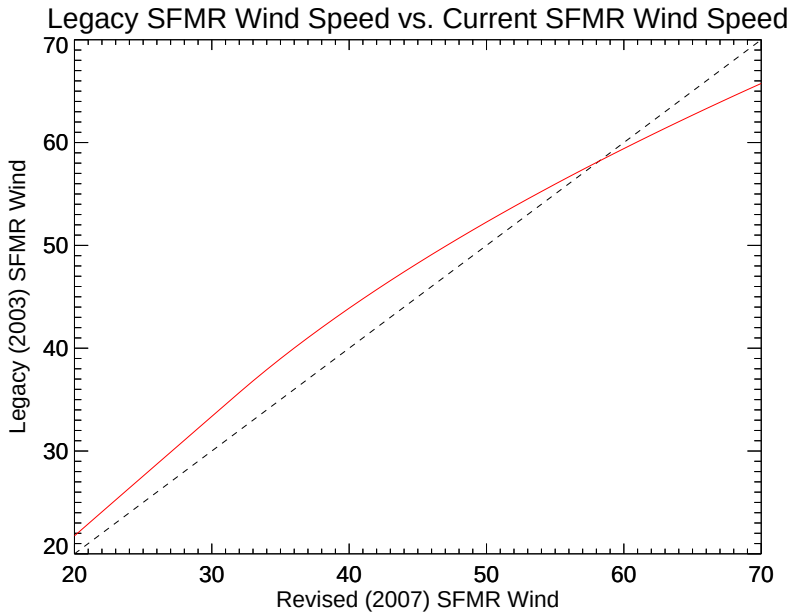

Figure 3.1. Illustration of the change in SFMR model of excess emissivity due to wind. The 2003 model overestimated wind speeds below approximately $58\,\mathrm{m\,s^{-1}}$.

Table 3.1. Remapped IWRAP GMF Coefficients: A_0 Parameters

Radar	Pol.	Incidence Angle (°)	β	γ_0	γ_1	γ_2
C-band	VV	29.0	−3.1803	3.3693	−0.9923	0
		34.0	−4.1806	4.2092	−1.1996	0
		40.0	−4.9856	4.8417	−1.3290	0
		50.0	−6.2902	6.2018	−1.7647	0
	HH	31.0	−4.2560	4.0461	−1.1776	0
		36.0	−5.3874	5.0899	−1.4213	0
		42.0	−5.9355	5.3750	−1.4185	0
		49.0	−6.6837	5.8551	−1.4971	0
Ku-band	VV	29.0	22.4580	−46.2950	30.9660	−6.8162
		34.0	3.0119	−10.0330	8.2751	−2.0871
		39.0	4.8190	−14.6660	11.7330	−2.9123
		48.0	−7.0057	7.5170	−2.5001	0.1377
	HH	29.0	−0.0529	−2.8521	3.1881	−0.9273
		35.0	−2.0343	−0.6112	2.2958	−0.8152
		41.0	0.0103	−5.5130	5.6316	−1.5354
		48.0	2.1492	−11.0850	9.5888	−2.4097

Table 3.2. Remapped IWRAP GMF Coefficients: a_1 Parameters

Radar	Pol.	Incidence Angle (°)	c_1	c_2	c_3
C-band	VV	29.0	$7.6260 \cdot 10^{-3}$	$4.9330 \cdot 10^{-3}$	$-3.1680 \cdot 10^{-5}$
		34.0	$-4.2310 \cdot 10^{-3}$	$7.6040 \cdot 10^{-3}$	$-5.7510 \cdot 10^{-5}$
		40.0	$-1.0300 \cdot 10^{-1}$	$1.2600 \cdot 10^{-2}$	$-1.2520 \cdot 10^{-4}$
		50.0	$-3.9680 \cdot 10^{-1}$	$2.1360 \cdot 10^{-2}$	$-2.2440 \cdot 10^{-4}$
	HH	31.0	$7.0380 \cdot 10^{-2}$	$3.5170 \cdot 10^{-3}$	$-2.5170 \cdot 10^{-5}$
		36.0	$-4.6340 \cdot 10^{-2}$	$1.1460 \cdot 10^{-2}$	$-1.1180 \cdot 10^{-4}$
		42.0	$9.4450 \cdot 10^{-2}$	$3.7730 \cdot 10^{-3}$	$-3.3660 \cdot 10^{-5}$
		49.0	$-1.8120 \cdot 10^{-2}$	$9.1030 \cdot 10^{-3}$	$-1.0720 \cdot 10^{-4}$
Ku-band	VV	29.0	$2.0050 \cdot 10^{-3}$	$3.2440 \cdot 10^{-4}$	$4.1830 \cdot 10^{-5}$
		34.0	$1.6810 \cdot 10^{-1}$	$-7.8220 \cdot 10^{-3}$	$1.2430 \cdot 10^{-4}$
		39.0	$4.4690 \cdot 10^{-2}$	$-9.7860 \cdot 10^{-4}$	$3.5080 \cdot 10^{-5}$
		48.0	$-5.6340 \cdot 10^{-2}$	$4.6660 \cdot 10^{-3}$	$-3.2150 \cdot 10^{-5}$
	HH	29.0	$1.4590 \cdot 10^{-1}$	$-6.1500 \cdot 10^{-3}$	$9.6960 \cdot 10^{-5}$
		35.0	$2.0460 \cdot 10^{-1}$	$-8.2260 \cdot 10^{-3}$	$1.2180 \cdot 10^{-4}$
		41.0	$1.2190 \cdot 10^{-1}$	$-4.7380 \cdot 10^{-3}$	$8.0160 \cdot 10^{-5}$
		48.0	$1.1540 \cdot 10^{-2}$	$1.0410 \cdot 10^{-3}$	$2.4830 \cdot 10^{-5}$

Table 3.3. Remapped IWRAP GMF Coefficients: a_2 Parameters

Radar	Pol.	Incidence Angle (°)	d_1	d_2	d_3	d_3
C-band	VV	29.0	$-1.7960 \cdot 10^{-1}$	$3.9680 \cdot 10^{-2}$	$-3.7520 \cdot 10^{-2}$	$3.00 \cdot 10^{1}$
		34.0	$-7.7830 \cdot 10^{-2}$	$5.9610 \cdot 10^{-2}$	$-5.7680 \cdot 10^{-2}$	$2.00 \cdot 10^{1}$
		40.0	$1.1890 \cdot 10^{-1}$	$3.5170 \cdot 10^{-2}$	$-3.6610 \cdot 10^{-2}$	$1.80 \cdot 10^{1}$
		50.0	$5.9390 \cdot 10^{-2}$	$4.1520 \cdot 10^{-2}$	$-4.1980 \cdot 10^{-2}$	$1.90 \cdot 10^{1}$
	HH	31.0	$-1.0340 \cdot 10^{-1}$	$2.9500 \cdot 10^{-2}$	$-2.8490 \cdot 10^{-2}$	$3.00 \cdot 10^{1}$
		36.0	$-2.2980 \cdot 10^{-1}$	$7.4780 \cdot 10^{-2}$	$-7.0600 \cdot 10^{-2}$	$2.00 \cdot 10^{1}$
		42.0	$1.8210 \cdot 10^{-1}$	$1.6900 \cdot 10^{-2}$	$-1.9890 \cdot 10^{-2}$	$1.80 \cdot 10^{1}$
		49.0	$7.4150 \cdot 10^{-2}$	$4.0130 \cdot 10^{-2}$	$-4.0950 \cdot 10^{-2}$	$1.90 \cdot 10^{1}$
Ku-band	VV	29.0	$-6.8130 \cdot 10^{-1}$	$1.1670 \cdot 10^{-1}$	$-1.0470 \cdot 10^{-1}$	$2.30 \cdot 10^{1}$
		34.0	$-6.3290 \cdot 10^{-1}$	$1.5330 \cdot 10^{-1}$	$-1.3960 \cdot 10^{-1}$	$2.00 \cdot 10^{1}$
		39.0	$-1.5200 \cdot 10^{-1}$	$3.1910 \cdot 10^{-1}$	$-3.1460 \cdot 10^{-1}$	$1.20 \cdot 10^{1}$
		48.0	$1.8650 \cdot 10^{-1}$	$3.6570 \cdot 10^{-1}$	$-3.6190 \cdot 10^{-1}$	$1.10 \cdot 10^{1}$
	HH	29.0	$-4.0770 \cdot 10^{-1}$	$9.5000 \cdot 10^{-2}$	$-8.5990 \cdot 10^{-2}$	$2.30 \cdot 10^{1}$
		35.0	$-5.1330 \cdot 10^{-1}$	$1.0640 \cdot 10^{-1}$	$-9.5910 \cdot 10^{-2}$	$2.00 \cdot 10^{1}$
		41.0	$-5.0670 \cdot 10^{-2}$	$2.5930 \cdot 10^{-1}$	$-2.5590 \cdot 10^{-1}$	$1.20 \cdot 10^{1}$
		48.0	$-1.0630 \cdot 10^{-1}$	$3.3980 \cdot 10^{-1}$	$-3.3530 \cdot 10^{-1}$	$1.10 \cdot 10^{1}$

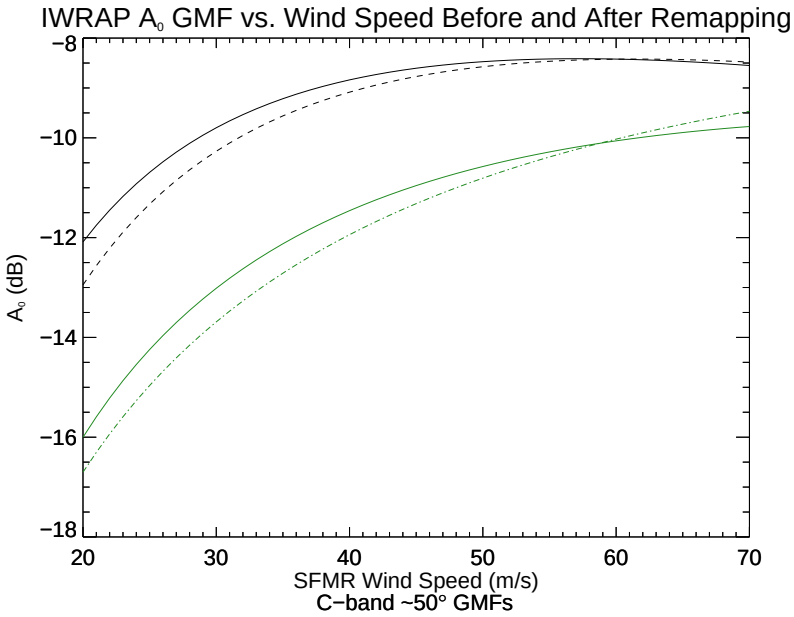

Figure 3.2. Illustration of the change in IWRAP GMF due to a change in the SFMR GMF. The upper curves are the old (dashed) and remapped (solid) C-band VV-polarization GMF at 50°. The lower curves are the old (dash-dotted) and remapped (solid) C-band HH-polarization GMF at 49°. An underestimation of SFMR wind speeds above approximately $58\,\mathrm{m\,s^{-1}}$ results in an expected lower observed NRCS.

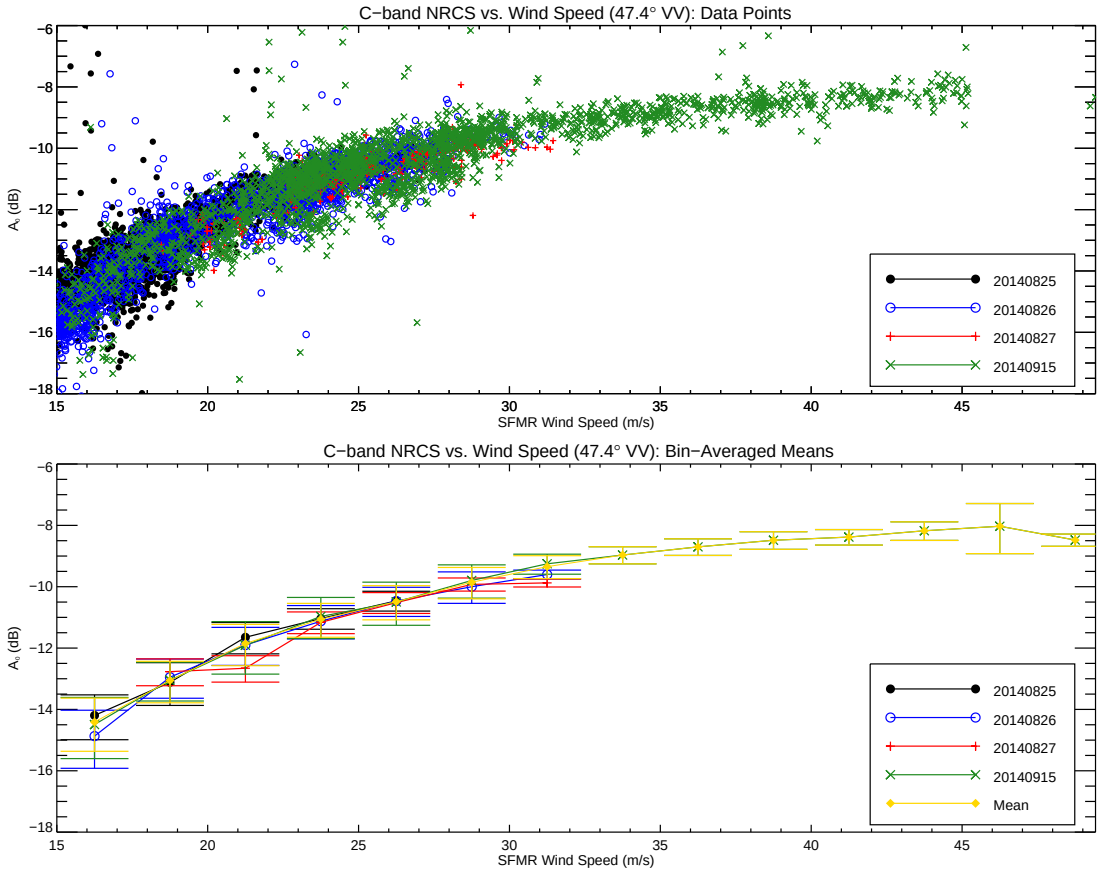

Figure 3.3. Mean IWRAP NRCS (A_0) vs. SFMR Wind Speed for four flights in the 2014 hurricane season, illustrating variability both within a flight and between flights. These data are from the outer incidence angle (47.4°) of the C-band radar at VV-polarization. The points are A_0 estimates from individual wind vector cells of alongtrack distance 0.5 km. The data are binned into 2.5 m s^{-1}-wide wind speed bins. The solid lines are the interquartile means and the error bars are the interquartile standard deviations.

uncertainty, and sampling uncertainty. Here each potential source is described and the offsets observed in the IWRAP data are explained.

3.3.1 Statistical Variability

Statistical variability is an apparent change in the observed scene due to motion of the scatterers relative to the antenna. For every measurement of the ocean surface made by a scatterometer, a spot on the surface containing multiple scatterers is illuminated. The echo measured by the radar is a vector sum of these scatterers. The

phase of the vector component of the total is related to the distance of the radar from each scatterer. Any change in antenna position relative to the illuminated area results in a different coherent average, even from the same scatterers. This phenomena is called fading, and it is the primary contributor to statistical variability.

The fading process is expected to be a zero-mean random process. Given many independent realizations of the surface NRCS, the uncertainty of the mean should be small. The effect of fading on mean NRCS should not vary much from one season to the next, or even between flights provided that there are sufficient samples in the average.

3.3.2 Geophysical Variability

Geophysical variability is a change in the observed scene due to a geophysical phenomenon other than wind speed and wind-relative antenna direction. The observed scene can either refer to the backscattered power seen by IWRAP or the brightness temperature attributed to the ocean surface wind speed by the SFMR. A change that is not accounted for in either NRCS or surface wind speed will contribute to this variability.

The ocean surface is a complex target with many features contributing to backscattered power. The widely-accepted theoretical model for scattering at C- and Ku-bands at low to moderate wind speeds is the Composite Surface Model or Composite Bragg. In this model, Bragg scatterers riding on top of waves with longer wavelengths resonate with the wavelength of the radar. However, there are other sea-surface features that could account for scattering but are not accounted for in the theoretical or most empirical models. Those features include are sea spray, plumes, sloshes or hydraulic shocks, pools of surface roughness associate with breaking waves, and wedge- or pyramid-shaped structures [40]. Sea ice is frequently observed during the winter flight experiments, but these areas are easily eliminated from consideration (in the

absence of visual confirmation of the surface, SFMR retrievals over ice are sporadic, often reporting extreme, unrealistic wind speeds). Downdrafts associated with precipitation, precipitation splash effect, and attenuation and scattering due to precipitation are accounted for in the rain-free NRCS observations. Some other variables that are neglected include:

Atmospheric stratification Air-sea temperature differences result in a different mapping between surface stress and 10 m equivalent neutral wind speed. Since scatterometers respond to wind stress, the sampled NRCS will not reflect the true wind speed at 10 m height if there is a large air-sea temperature gradient. The SFMR, however, retrieves true wind speed at 10 m [27]. This difference is estimated to be on the order of $\pm 0.5\,\mathrm{m\,s^{-1}}$ in wind speed or 0.3 dB to 0.6 dB in NRCS at low wind speeds [41]. It is not significant at high wind speeds, compared to other sources of variability. Not only does the NRCS approach saturation—so any offset in wind speed translates to smaller NRCS—but the ratio between U_{10N} and U_{10} goes to unity as U_{10} increases [2].

Ocean surface currents There is some evidence that scatterometers are affected by ocean surface currents [42]. This makes sense considering that the definition of wind stress is "the vector difference between wind and current" [41]. This effect is estimated to be less than $1\,\mathrm{m\,s^{-1}}$ in wind speed or 0.5 dB to 1 dB in NRCS at low wind speeds. The surface current component of the stress vector becomes less significant at high wind speeds compared to the wind vector, so the error due to surface current is expected to decrease as wind speed increases.

Sea state Some scatterometer observations show a dependence of NRCS on significant wave height and significant wave steepness [7], [43]. Mouche *et al.* [7] note an effect on polarization ratio ($\frac{\sigma^0_{VV}}{\sigma^0_{HH}}$) of about 1 dB over each of the ranges of wave height and steepness. Zhang *et al.* [43] find comparable effects within the

same wind speed range from other instruments, with perhaps a slightly larger dependence on significant wave height. Fetch and duration are typically neglected when analyzing scatterometer data, due to the size of the footprint of the scatterometer [44]. These phenomena, however, may be more significant at the scales observed by IWRAP and the SFMR. Powell *et al.* [45] show a variation of $\pm 2\,\mathrm{m\,s^{-1}}$ in SFMR-retrieved winds with respect to GPS dropsondes, depending on location of SFMR retrieval within a tropical cyclone (TC). This amount of wind speed error can cause up to 2 dB of error in mean NRCS. They attribute the variation to swell effects on wave breaking. When the swell and wind are moving in the same direction, fewer waves break and produce less foam; the opposite effect happens when swell and wind oppose each other.

Sea surface temperature and salinity The SFMR retrieval is dependent to a small degree on SST and salinity. Occasionally, the high-latitude winter flight experiments will cross steep SST gradients. At wind speeds above $20\,\mathrm{m\,s^{-1}}$, wind speed errors are less than $\pm 2\,\mathrm{m\,s^{-1}}$ (less than 0.6 dB in NRCS) for SST errors of $\pm 3\,^{\circ}\mathrm{C}$, and salinity errors are relatively insignificant [28]. These errors are smaller than the RMS error of the SFMR compared to GPS dropsondes ($2.5\,\mathrm{m\,s^{-1}}$), which is the wind speed bin size chosen for averaging.

Each of these could vary with season, flight, or even location in the flight pattern. The most significant geophysical variability in IWRAP observations, especially between flights, is expected to come from that of the sea state.

3.3.3 Sampling Uncertainty

The sampling uncertainty is the variability in the sampled transmit pulse peak power $P_{t,s}$ or the peak surface echo power due to the sampling frequency. Prior to the 2013 hurricane season the IWRAP digital receiver sampled at 80 MHz; since then it has sampled at 100 MHz. In both cases the receiver samples an IF signal centered

at 30 MHz with a maximum bandwidth of 4 MHz. After sampling, the data samples are decimated by a factor of 16, resulting in an output bandwidth of 4 MHz. Both the 200 ns pulse and the 10 µs chirp (at 4 MHz bandwidth) are undersampled at this rate. The bandwidth of the DR must be twice the bandwidth of the signal in order to prevent aliasing. Additionally, the DR samples at a slightly different time every time it is restarted, causing some slight apparent transmit power changes to occur. A change in P_t in (3.10) results in a change to the measured NRCS. If these apparent changes are a function of the sampling bandwidth in the digital receiver, and do not reflect a change in real transmit power, then they cause additional spread in the NRCS. Figure 3.4 shows an example of A_0 as a function of wind speed for a flight during which the measured $P_{t,s}$ changed significantly. The actual $P_{t,s}$ likely did not change by the same amount, resulting in a vertical offset of the A_0 data. This channel was not able to be calibrated for this flight, so it was omitted from analysis. Figure 3.5 shows the pulse-compressed channel from the same radar and the same flight. It does not appear to have the same issues as the pulsed channel, so it was included in the analysis.

3.3.4 Calibration Offset

The calibration offset of an IWRAP radar (C-band or Ku-band) is the difference of the mean NRCS sample with respect to the true NRCS at any given wind speed, when all other geophysical variables are considered. This can be accounted for in two variables: the PA output power at the input to the antenna (P_t) and the overall receiver gain (G_{rec}). The transmit power is used to calculate the NRCS as seen immediately above the antenna:

$$\sigma^0 = (4\pi)^3 R^4 \frac{P_r}{P_t G^2 \lambda^2 A_{ill}}, \tag{3.10}$$

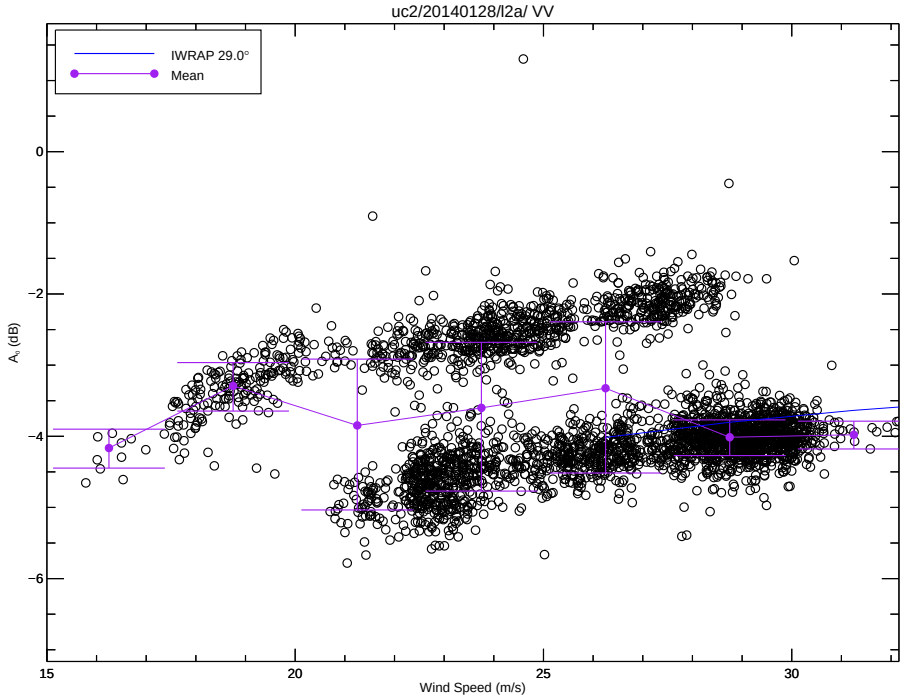

Figure 3.4. Mean NRCS (A_0) estimates, shown as empty circles, for the inner angle of the C-band radar at VV-polarization for the flight experiment on January 21, 2014. A_0 samples are grouped into wind speed bins of $2.5\,\mathrm{m\,s^{-1}}$ and averaged. The mean A_0 values for each bin are plotted as filled circles and the standard deviations are the error bars. The IWRAP GMF, which is only valid above $25\,\mathrm{m\,s^{-1}}$, is shown as a blue solid line. Note the vertically displaced cloud of NRCS measurements, which skews the mean in at least 3 wind speed bins.

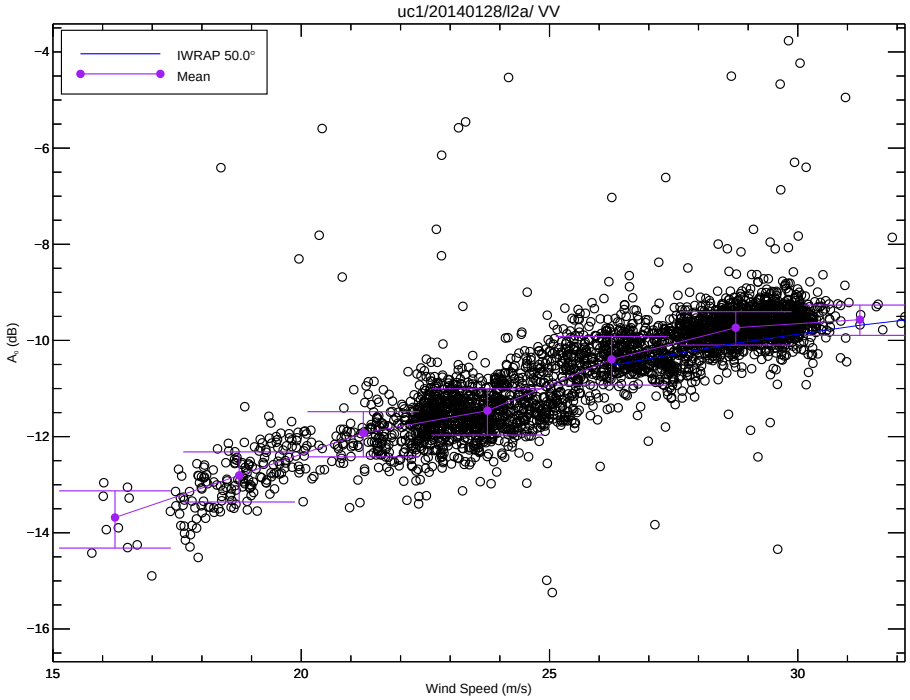

Figure 3.5. Mean NRCS (A_0) estimates, shown as empty circles, for the outer angle of the C-band radar at VV-polarization for the flight experiment on January 21, 2014. A_0 samples are grouped into wind speed bins of $2.5\,\mathrm{m\,s^{-1}}$ and averaged. The mean A_0 values for each bin are plotted as filled circles and the standard deviations are the error bars. The IWRAP GMF, which is only valid above $25\,\mathrm{m\,s^{-1}}$, is shown as a blue solid line. These NRCS measurements are consistent over the flight.

where R is the slant range to the surface, P_r is the received power, P_t is the transmitted power, G is the antenna gain, λ is the wavelength, and A_{ill} is the illuminated area. The measured receiver gain is required in order to map voltages sampled by the digital receiver to input voltages at the antenna. If either P_t or G_{rec} is measured improperly, the measured NRCS will be affected in the same way. A calibration error will appear as a systematic bias in the NRCS when compared with another radar measuring the same quantity.

Due to the fixed sampling rate, R is known to within 30 m. A_{ill} is a function of altitude, instantaneous incidence angle (which is a function of azimuth and aircraft attitude), and antenna beamwidths, which are all known quantities. And while antenna gain G is not precisely known at all frequencies, it can at least be reasonably assumed to be unchanging over time. Therefore, any change in measured NRCS over time should not be due to changing antenna gain, range uncertainty, or uncertainty about the illuminated area.

G_{rec} is the amount of gain from the input of the LNA to the output of the digital receiver. So to calculate P_r in (3.10), G_{rec} and the losses up to the LNA input from the digital receiver samples need to be removed. As shown in figures 2.2 and 2.3, the calibration loop allows for measurement of changes in PA output. In both calculations, it is assumed that L_{cal}, L_{rx}, L_{tx}, L_{cable}, and L_{ant} are static and known quantities. The sample of the transmit pulse in the measured profile combines any change in either of the two quantities P_t and G_{rec}. In other words, a change in amplitude of the sampled transmit power peak, $P_{t,s}$, cannot be attributed to a change in PA output without assuming G_{rec} is known. While G_{rec} is estimated twice each season from external measurements performed on the ground, changes to the system of unknown quantity may occur when disconnecting and reconnecting components. So G_{rec} is estimated for each profile from the sampled noise power and the computed noise power ($kTBF$) of the system.

The calibration loop loss, L_{cal}, is estimated twice each season during ground calibration of IWRAP. The transmit power is measured by a peak power meter at the same time as the digital receiver records the pulse through the calibration loop. The transmit power at the output of the PA is calculated by adding any intervening loss to the power meter measurement. The receiver gain is also estimated by injecting a signal of known power into the receiver while the digital receiver records the level. The power at the input to the LNA is estimated by subtracting the measured receiver gain from the digital-receiver-sampled peak transmit power. From this measurement and the output of the PA, L_{cal} is estimated for the season. This procedure is performed to take into account changes in the calibration loop that naturally occur when uninstalling and reinstalling the system. This is another potential source of error from season to season, as it affects $P_{t,s}$, though it is small. However, like antenna gain, it can be considered to be a constant offset for each season.

To remove the uncertainty primarily due to unknown antenna gain G, insertion loss of the antenna, and L_{cal}, an adjustment is made to the NRCS so that the mean A_0 taken over many samples within a wind speed range matches the existing IWRAP GMF. If this method truly removes the calibration bias, the measured A_0 should be comparable to the existing IWRAP GMF. This adjustment is applied to individual seasons under the assumption that once the radar is installed, the gain and insertion loss of the antennas remain consistent. The wind speed range chosen for removing calibration bias is one that is reliable in both the SFMR and the IWRAP systems, and one that is valid for both GMFs: $25\,\mathrm{m\,s^{-1}}$ to $27\,\mathrm{m\,s^{-1}}$. All NRCS A_0 estimates for rain-free wind vector cells measured at level flight within this SFMR wind speed range for each available incidence angle, frequency band, polarization, and flight are collected for the calibration procedure to be performed on each combination. For each combination of polarization and frequency (and, thus, incidence angle), this adjustment should be clustered around a central offset for each season. The scatter

is attributed to statistical and geophysical variation, and the offset can be attributed to calibration bias. However, all of this discussion relies on consistent samples of P_t and P_r. If either of these variables are inconsistently sampled—for example, if the sample timing of the transmit power changes unexpectedly—then the calibration offset cannot be determined.

3.4 Methodology for Developing a New Rain-Free Geophysical Model Function

3.4.1 SFMR Reprocessing

Though surface wind speed and rain rate are retrieved in real-time, SFMR T_bs are reprocessed using quality-controlled aircraft data (e.g., radar altitude and ambient temperature) and modeled ocean SSTs and salinities. This is done in order to remove errors due to the retrieval algorithm implemented in SFMR and mismatched real-time data from the aircraft. Errors in the SFMR retrievals due to SST and salinity are minimized by using models (NOAA/NCDC AVHRR Daily-OI-V2 and HYCOM GLBa0.08, respectively) for the time and location nearest to each point in a flight experiment.

SFMR reprocessing starts with a 5 s boxcar average performed on each T_b channel. Bias with respect to the GMF is then removed from the T_bs by the following algorithm:

1. Perform retrieval, retaining the difference ($\epsilon_i = T_{b,measured,i} - T_{b,modeled,i}$) for each retrieval;

2. Obtain mean ϵ_i ($\bar{\epsilon_i}$) for each T_b channel, after removing outliers that are more than two standard deviations away from the mean;

3. Subtract the mean of $\bar{\epsilon_i}$ from all T_b channels (i.e., one value is obtained from all $\bar{\epsilon_i}$).

Any retrievals within 10 km of land are eliminated using a landmask generated by GMT (Generic Mapping Tools) version 4.5.9 and the GSHHG (A Global Self-consistent, Hierarchical, High-resolution Geography) database.

3.4.2 IWRAP Data Processing

To develop a new rain-free geophysical model function, IWRAP measurements and SFMR surface wind speed retrievals are collocated. NRCS measurements from IWRAP are averaged into alongtrack cells of 2.5 km length. Each cell is divided into 64 track-relative azimuth bins, resulting in an average over 5.625° per bin. All radar beams for each polarization resulting in a surface echo within an alongtrack cell are averaged within these azimuth bins. Figure 3.6 illustrates the along-track averaging scheme. SFMR and some location data are associated with an alongtrack cell only when the aircraft is over the cell. Only data taken when the aircraft is level is used, in order to limit the effects of non-uniform incidence angle. Level flight is considered to be when the instantaneous incidence angle of the radar beam is within ±2° of nominal. This threshold was chosen in order to keep the number of profiles discarded solely due to incidence angle below 10 %. The percentage of profiles discarded within a wind speed bin due to incidence angle do not depend on wind speed; that is, there are not significantly more profiles discarded at high wind speeds (e.g., during hurricane eyewall penetrations). The small threshold on incidence angle also limits the effects of polarization mixing (i.e., sampling NRCS at a polarization that is not purely V- or H-polarization) due to aircraft attitude.

Before averaging, any incidence angle dependence is removed from NRCS measurements by referencing an existing GMF. Given the SFMR wind speed and flight-level wind direction, the theoretical NRCS is computed via the GMF at the nominal incidence angle and the instantaneous incidence angle. The ratio of these calculations is multiplied with the NRCS (in linear units). The GMF used at C-band is the CMOD5.n

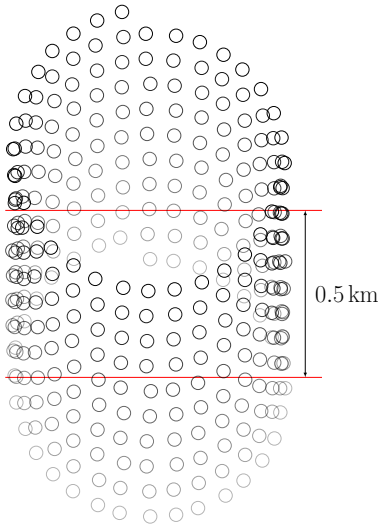

Figure 3.6. Schematic diagram of the binning scheme for one wind vector cell. Aircraft motion is upwards and illumination of the surface is shown as solid circles. An NRCS sample is included in the average if the center of the beam falls between the solid lines. Azimuthal averaging is not depicted.

GMF [35] (the polarization ratio from Vachon and Wolfe [6] is then applied for HH-pol). At Ku-band, the NSCAT2 GMF is used, which is a dual-polarization function of incidence angle.

Any NRCS values affected by rain, whether that is by attenuation and scattering or by surface modification, are discarded. Rain between the aircraft and surface is tested by way of the normalized spectral width, and values below 0.30 are flagged as rain-contaminated. Additionally, any wind vector cell with an SFMR wind speed below $15\,\mathrm{m\,s^{-1}}$ or rain rate above $5\,\mathrm{mm\,h^{-1}}$ is discarded; these are the minimum values reliably retrievable from the SFMR [28].

Some along-track cells will not have data at some azimuth angles due to aircraft attitude, the presence of rain, or other circumstances. In order to ensure a reasonable amount of confidence in the A_0 estimates, a threshold is placed on coverage in azimuth. For each 2.5 km wind vector cell, the percentage of data points missing in the azimuth dimension is calculated and cells that are missing more than 25 % of their samples in azimuth are discarded.

For each remaining along-track cell, there will be a set of NRCS values that fall into the cell, the number of which depends on the ground speed of the aircraft and the actual rotation rate of the antenna. Once collected into a cell, the NRCS samples are grouped into 64 azimuth bins (5.625° per bin). The sample standard deviation of the NRCS data for each cell is also calculated per azimuth bin. The SFMR samples from the time the aircraft was over the cell are averaged together, since it is a nadir-pointing instrument. Any SFMR samples from incidence angles exceeding 3° are discarded. Since this is a nadir-pointing instrument mounted at −2° pitch, this is largely determined by the roll of the aircraft; the WP-3D usually flies at 1.5° to 2.5° pitch. This is different than the limit placed on NRCS samples, however, since instantaneous incidence angle in the case of IWRAP is also determined by antenna azimuth. NRCS data from each cell are fit to

$$\sigma^0 = A_0 + A_1 \cos\chi + B_1 \sin\chi + A_2 \cos 2\chi + B_2 \sin 2\chi \tag{3.11}$$

to determine the surface wind direction, taken to be the maximum of the fit. The median of the wind direction over 5 cells (12.5 km) of continuous flight time is used as the true surface upwind direction for each cell.

At extreme wind speeds, the difference between upwind and downwind is sometimes masked by noise. By using the peak NRCS as upwind, over many averages this can cause a false peak at the apparent upwind and a flat section in the apparent downwind direction. This is not a geophysical response; it is a result of accumulating more peak values for the 360° scan around 0°. To help alleviate this problem, one of two numerical ocean surface wind vector models is used. If the model wind direction for a cell is more than 90° (or 16 azimuth bins) away from the NRCS-estimated direction, the estimated direction is adjusted by 180°.

These cells are grouped by SFMR wind speed in 2.5 $\mathrm{m\,s^{-1}}$ bins beginning at 15 $\mathrm{m\,s^{-1}}$. 2.5 $\mathrm{m\,s^{-1}}$ was chosen to account for the uncertainty of the SFMR retrievals

with respect to GPS dropsondes [28]. The data are shifted so upwind is at 0° azimuth and are averaged within azimuth bins, resulting in 64 points per wind speed bin.

These points are fit to the model described by (3.1). For each frequency, polarization, and incidence angle, one term from (3.1) is selected for fitting. This term is estimated for each $2.5\,\mathrm{m\,s^{-1}}$-wide bin via a least squares fit of (3.1). Parameters of the selected term are derived using separate least squares fits to these estimates, with the independent vector chosen to be the center wind speeds of each bin. Except for d_3 and γ_2, all parameters are allowed to vary as required to minimize the χ^2 error. This process is repeated for each term.

As mentioned in section 3.2, in the development of the original d_3 parameter in (3.8) for the IWRAP GMF was taken from Donnelly *et al.* [39]. This parameter, along with d_2, determines the wind speed at which a_2 reaches a maximum. By setting d_3 to a constant, (3.8) becomes a linear equation but does not drastically impact the shape of the resulting fit. So for development of this GMF, the d_3 values given in Donnelly *et al.* [39] are used.

The results of (3.9) are in decibel units, which is a logarithmic expression of power. The dependent variable of (3.9) is a logarithm, so the equation is cubic in log-log space. In Fernandez *et al.* [30], the cubic term (with parameter γ_2) was added to the Ku-band A_0 parameterization in order to better model the fast decrease in A_0 at the highest wind speeds. It has also been included here, but since the same extreme wind speeds are not observed any changes to the Ku-band model should be minimized. To accomplish this, a least-squares fit to the data is performed, fixing γ_2 at the value from the IWRAP GMF at the closest incidence angle. After this fit is complete another fit is performed, allowing γ_2 to vary while fixing the other parameters. As C-band did not require this parameter, it remains fixed at 0.

3.5 Results of the New Rain-Free Geophysical Model Function

Here the results of carrying out the methodology described in the previous section for IWRAP data from selected flights between 2011 and 2014 are reported. During these seasons, the frequencies used to generate the particular incidence angles on the IWRAP instrument were kept consistent—approximately 22° and 48° for both C- and Ku-band radars. The exact incidence angle for a given frequency was determined by minimizing the difference between the estimated incidence angle (the arc cosine of the altitude divided by the slant-range distance to the peak in surface echo power) and the computed incidence angle (based on an initial angle estimate and aircraft attitude) over many samples. The flights selected represent a variety of rain-free ocean conditions, including those of high-latitude winter storms and Category 3 hurricanes.

Multiple aspects of the NRCS GMF are highlighted. The azimuthal response to the ocean surface wind vector is illustrated first to provide context for the rest of the chapter. The GMF is then separated into the mean and higher order components in order to derive functions of wind speed.

3.5.1 NRCS Response to Azimuth and Wind Speed

Figures 3.7 to 3.10 show NRCS as a function of azimuth for C-band at both VV and HH polarizations from $15\,\mathrm{m\,s^{-1}}$ to $45\,\mathrm{m\,s^{-1}}$. Along with the data, shown as black circles, and uncertainties of the mean, some GMFs and the fit to (3.1) are shown. The GMFs are CMOD5.n [35], CMOD5.h [36], IWRAP [30], and C-2013 (personal communication with L. Ricciardulli, Remote Sensing Systems). As these are all VV-polarization GMFs, with the exception of the IWRAP GMF, the polarization ratio from [6] is applied to the GMFs when comparing with HH-polarized data. The IWRAP GMF was developed at four incidence angles, so the model function at the closest incidence angle to the data is shown. Interpolation of parameters between

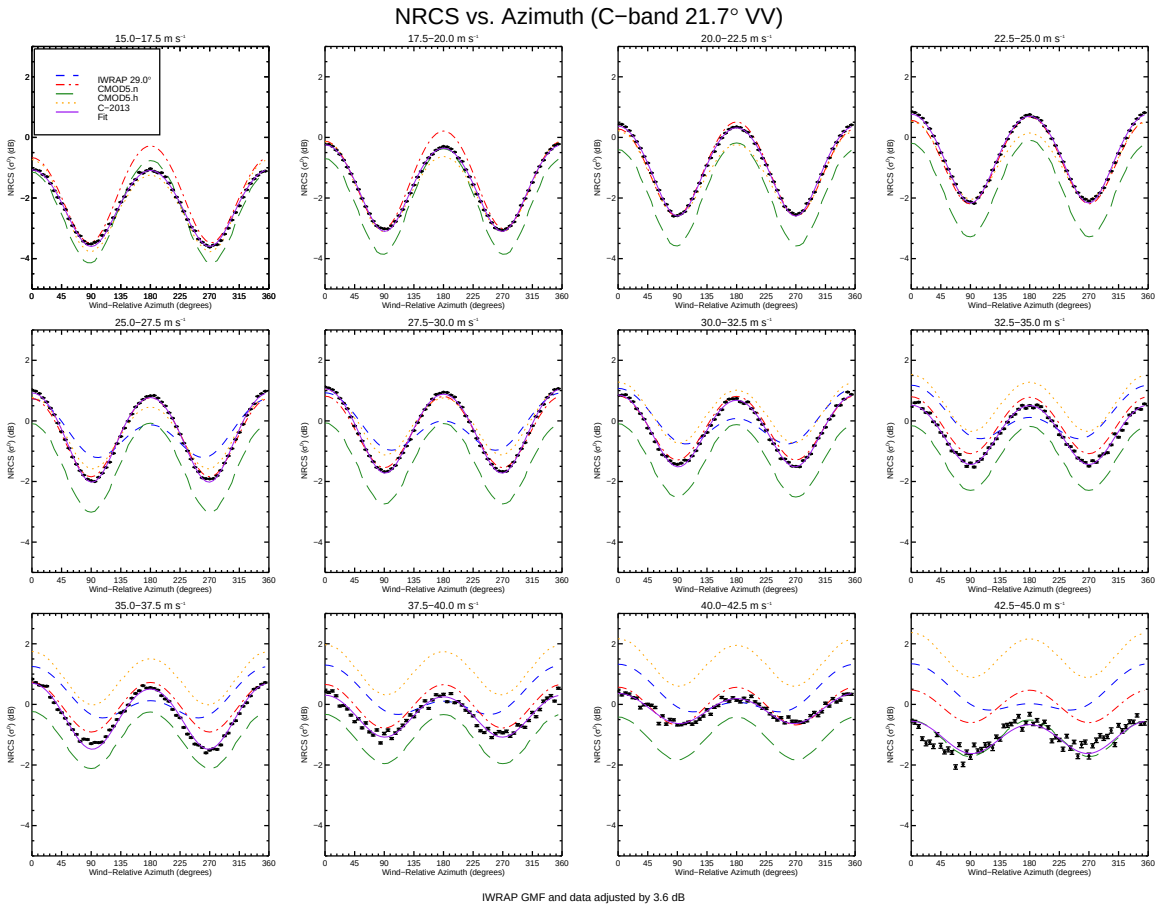

Figure 3.7. C-band NRCS vs. azimuth for VV-polarization at 21.7° incidence for wind speed bins from $15\,\mathrm{m\,s^{-1}}$ to $45\,\mathrm{m\,s^{-1}}$. Each wind speed bin is $2.5\,\mathrm{m\,s^{-1}}$ wide. Several GMFs are shown alongside the fit to the data, which is shown as a purple line. The IWRAP GMF was not designed to be used below $25\,\mathrm{m\,s^{-1}}$, so it is not shown in this region.

incidence angles to obtain a function at the exact incidence angle of the data is not performed. The remaining GMFs have a form that is a continuous function of incidence angle, so they can be compared directly. However, since the instrument that was used to develop these GMFs (ASCAT) does not sample NRCS below 25° incidence, an exact match at the lower incidence angle is not expected.

Figures 3.11 to 3.14 show NRCS as a function of azimuth for Ku-band at both VV and HH polarizations from $15\,\mathrm{m\,s^{-1}}$ to $45\,\mathrm{m\,s^{-1}}$. The GMFs shown are the NSCAT2, Ku-2011 [37], and IWRAP GMFs. Ku-2011 was developed from QuikSCAT data for

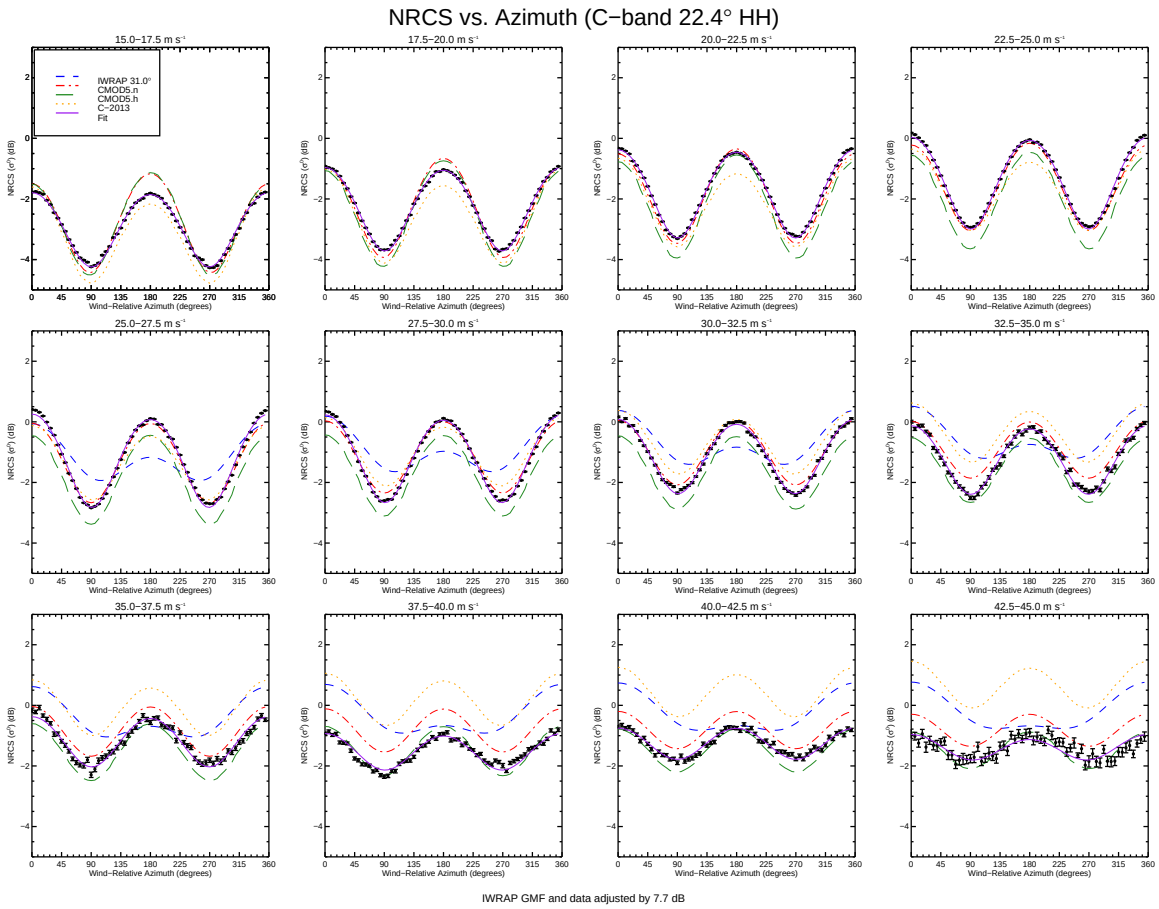

Figure 3.8. C-band NRCS vs. azimuth for HH-polarization at 22.4° incidence for wind speed bins from $15\,\mathrm{m\,s^{-1}}$ to $45\,\mathrm{m\,s^{-1}}$. Each wind speed bin is $2.5\,\mathrm{m\,s^{-1}}$ wide. Several GMFs are shown alongside the fit to the data, which is shown as a purple line. The IWRAP GMF was not designed to be used below $25\,\mathrm{m\,s^{-1}}$, so it is not shown in this region.

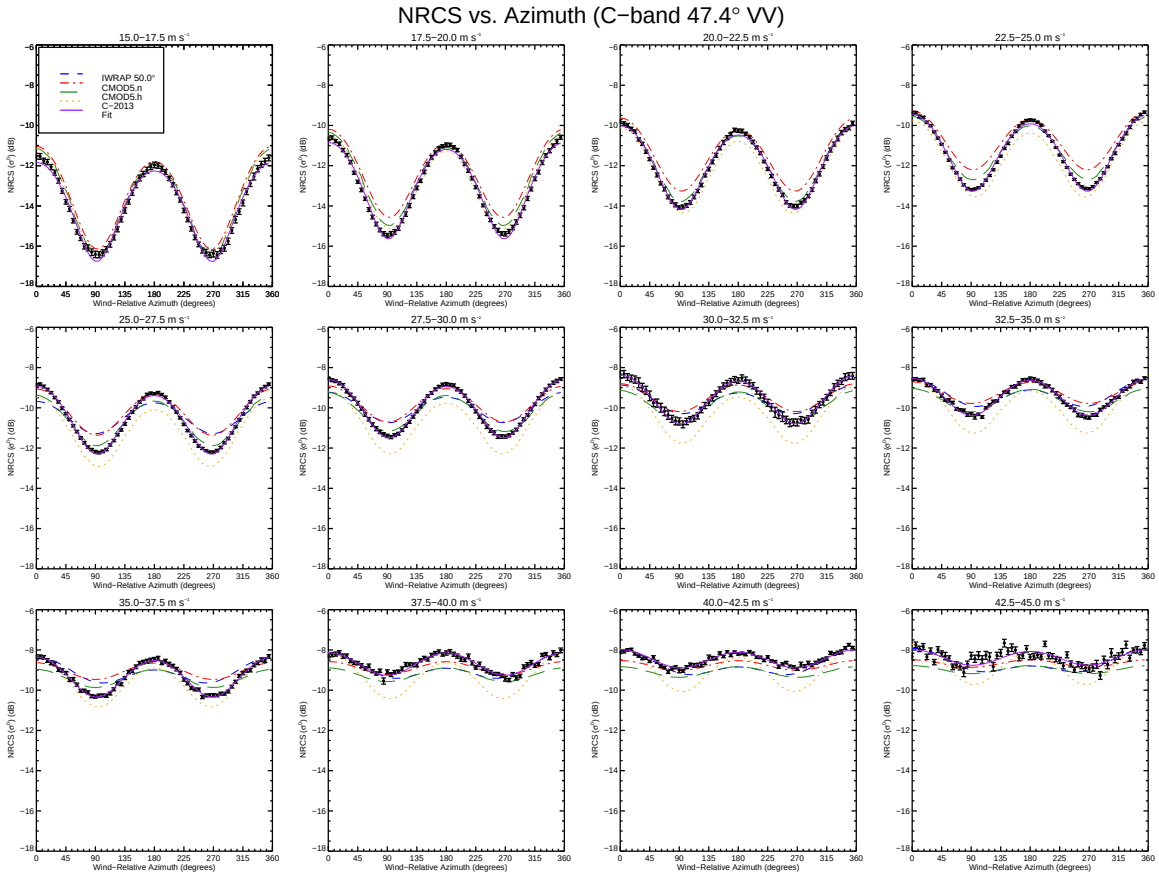

Figure 3.9. C-band NRCS vs. azimuth for VV-polarization at 47.4° incidence for wind speed bins from $15\,\mathrm{m\,s^{-1}}$ to $45\,\mathrm{m\,s^{-1}}$. Each wind speed bin is $2.5\,\mathrm{m\,s^{-1}}$ wide. Several GMFs are shown alongside the fit to the data, which is shown as a purple line. The IWRAP GMF was not designed to be used below $25\,\mathrm{m\,s^{-1}}$, so it is not shown in this region.

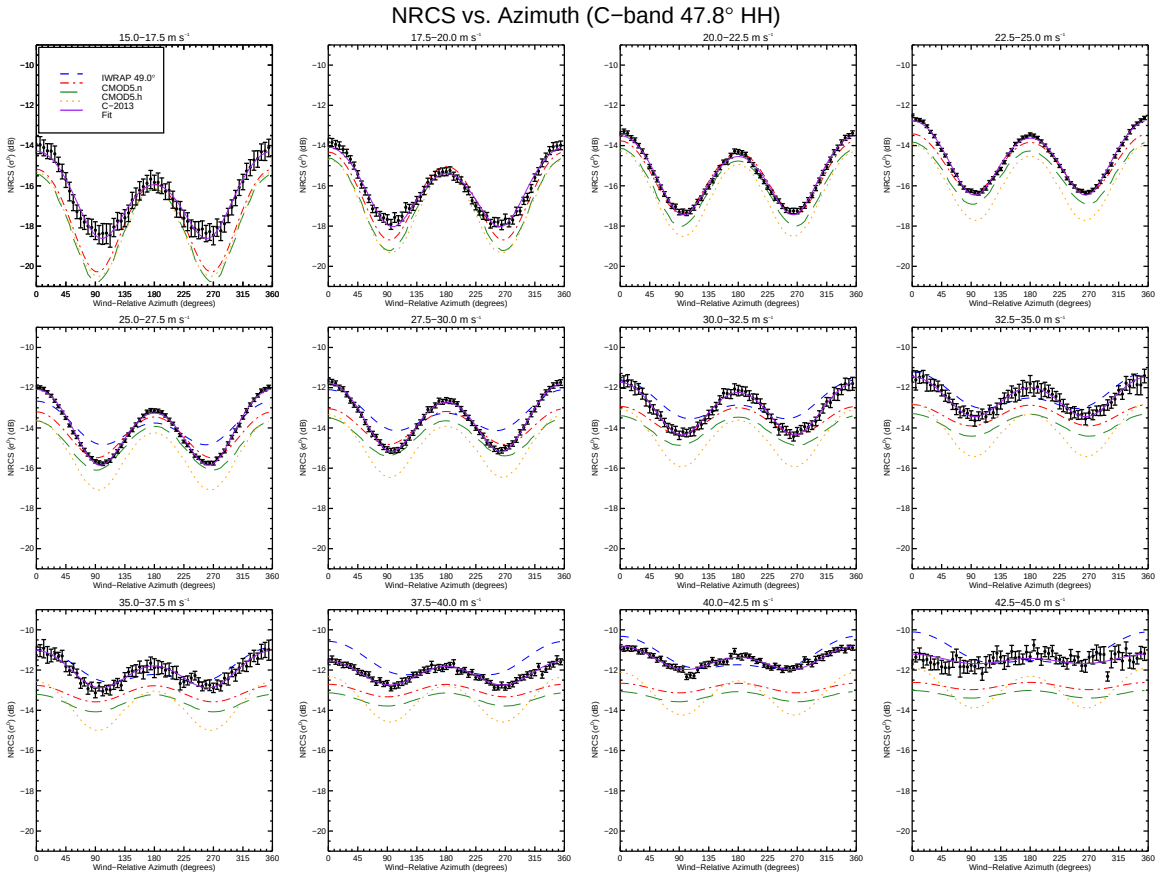

Figure 3.10. C-band NRCS vs. azimuth for HH-polarization at 47.8° incidence for wind speed bins from $15\,\mathrm{m\,s^{-1}}$ to $45\,\mathrm{m\,s^{-1}}$. Each wind speed bin is $2.5\,\mathrm{m\,s^{-1}}$ wide. Several GMFs are shown alongside the fit to the data, which is shown as a purple line. The IWRAP GMF was not designed to be used below $25\,\mathrm{m\,s^{-1}}$, so it is not shown in this region.

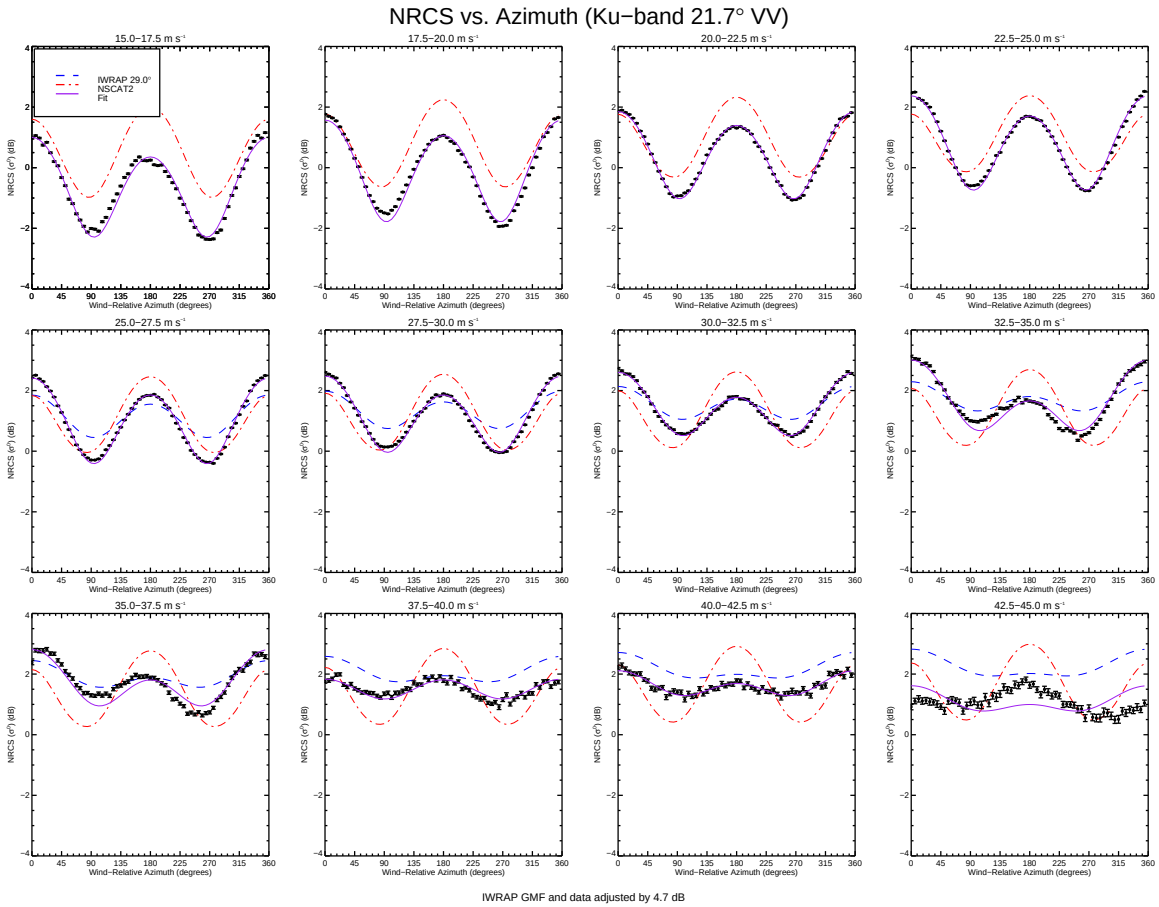

Figure 3.11. Ku-band NRCS vs. azimuth for VV-polarization at 21.7° incidence for wind speed bins from $15\,\mathrm{m\,s^{-1}}$ to $45\,\mathrm{m\,s^{-1}}$. Each wind speed bin is $2.5\,\mathrm{m\,s^{-1}}$ wide. Several GMFs are shown alongside the fit to the data, which is shown as a purple line. The IWRAP GMF was not designed to be used below $25\,\mathrm{m\,s^{-1}}$, so it is not shown in this region.

one incidence angle at VV (53°) and HH polarizations (46°), so the GMF for the appropriate polarization is shown at the larger incidence angles. The data are shown as circles with the uncertainty of the mean plotted as the error bars.

3.5.2 Mean NRCS Response to Wind Speed

Figure 3.15 shows the C-band A_0 estimates from the previous plots, GMFs, and the least-squares fits to the estimates. The parameters to the fits are given in table 3.4. The upper panels are labeled with a vertical offset that is applied to both the IWRAP

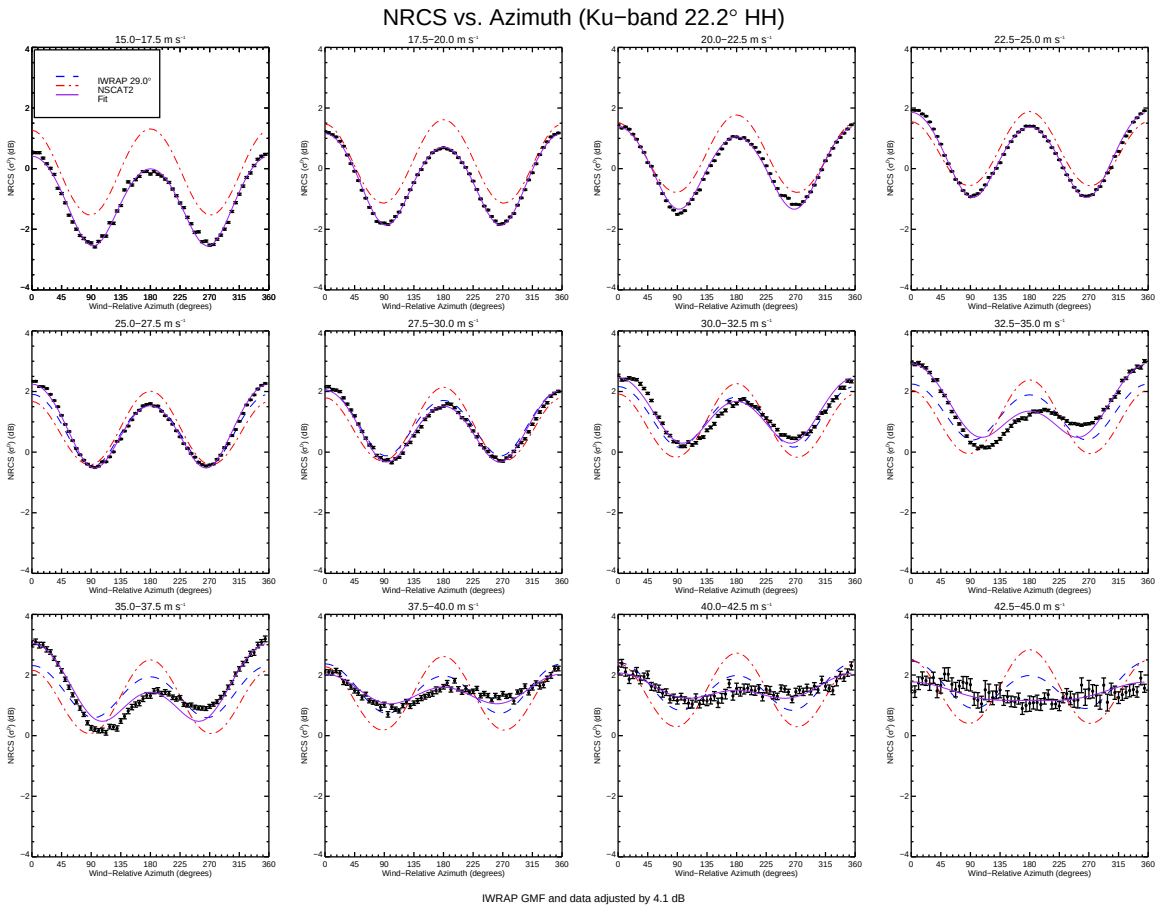

Figure 3.12. Ku-band NRCS vs. azimuth for HH-polarization at 22.2° incidence for wind speed bins from $15\,\mathrm{m\,s^{-1}}$ to $45\,\mathrm{m\,s^{-1}}$. Each wind speed bin is $2.5\,\mathrm{m\,s^{-1}}$ wide. Several GMFs are shown alongside the fit to the data, which is shown as a purple line. The IWRAP GMF was not designed to be used below $25\,\mathrm{m\,s^{-1}}$, so it is not shown in this region.

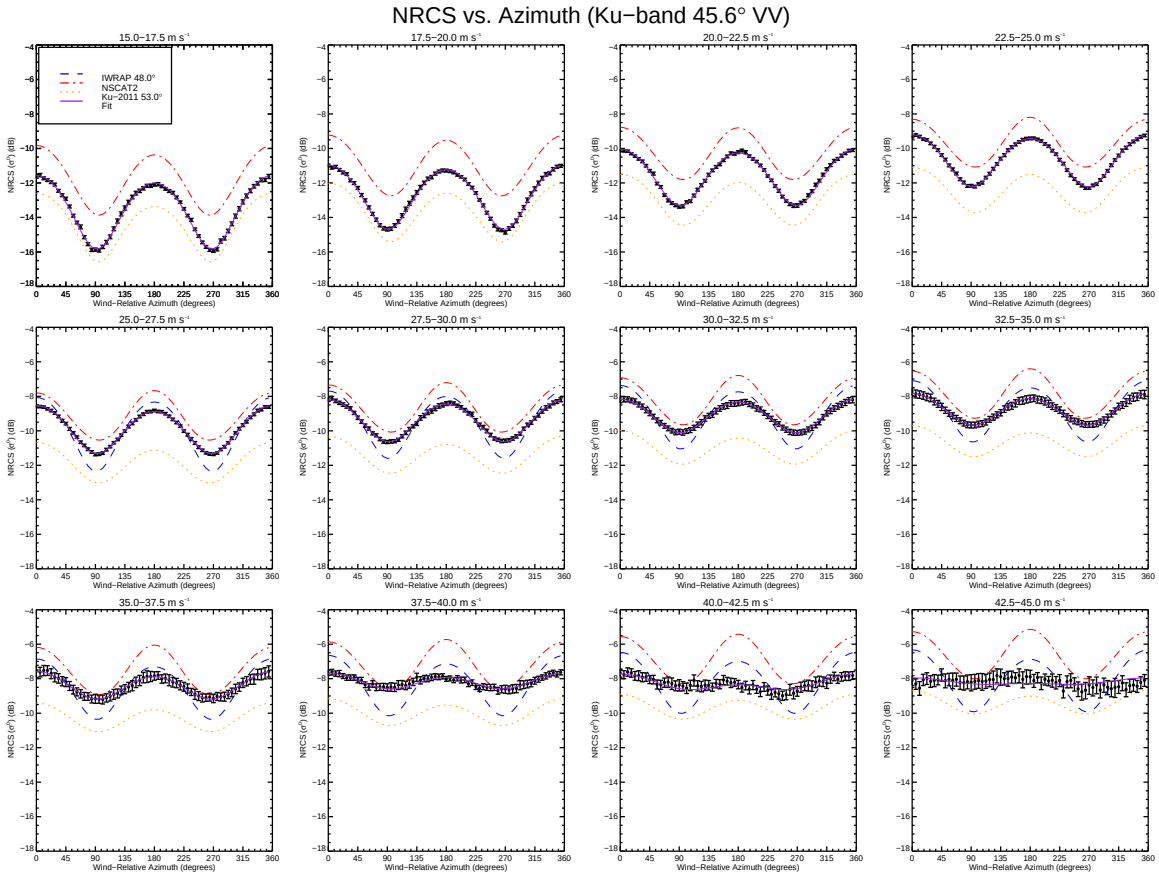

Figure 3.13. Ku-band NRCS vs. azimuth for VV-polarization at 45.6° incidence for wind speed bins from $15\,\mathrm{m\,s^{-1}}$ to $45\,\mathrm{m\,s^{-1}}$. Each wind speed bin is $2.5\,\mathrm{m\,s^{-1}}$ wide. Several GMFs are shown alongside the fit to the data, which is shown as a purple line. The IWRAP GMF was not designed to be used below $25\,\mathrm{m\,s^{-1}}$, so it is not shown in this region.

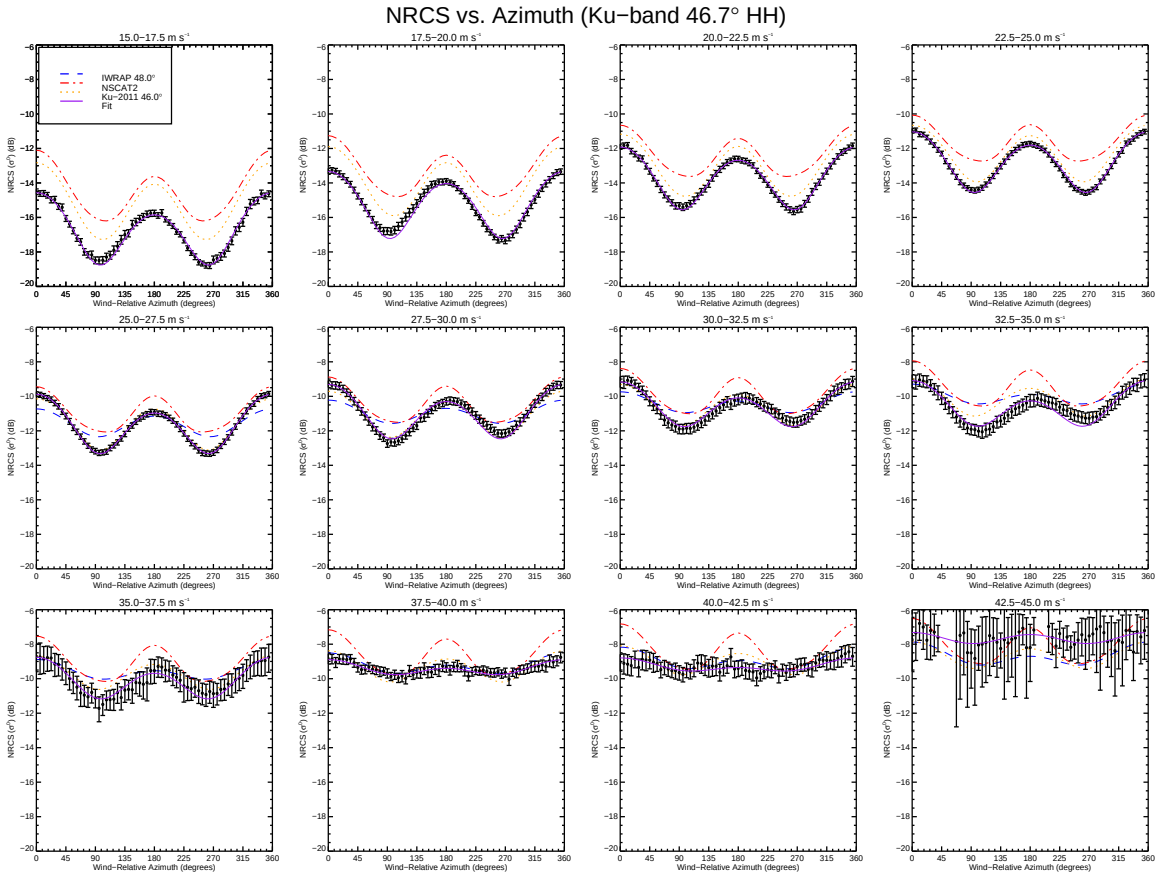

Figure 3.14. Ku-band NRCS vs. azimuth for HH-polarization at 46.7° incidence for wind speed bins from $15\,\mathrm{m\,s^{-1}}$ to $45\,\mathrm{m\,s^{-1}}$. Each wind speed bin is $2.5\,\mathrm{m\,s^{-1}}$ wide. Several GMFs are shown alongside the fit to the data, which is shown as a purple line. The IWRAP GMF was not designed to be used below $25\,\mathrm{m\,s^{-1}}$, so it is not shown in this region.

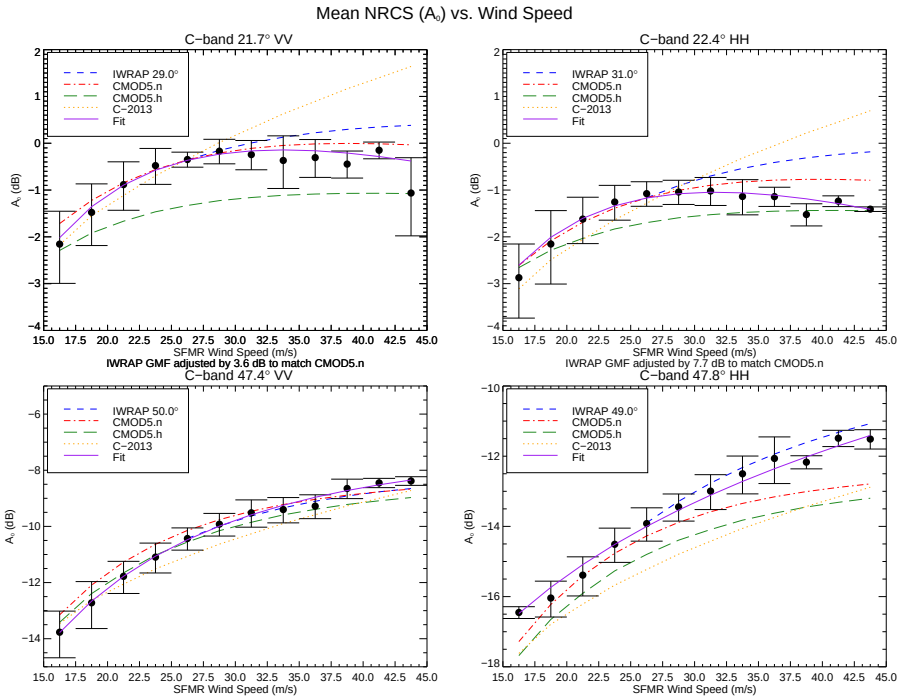

Figure 3.15. C-band mean NRCS vs. wind speed (A_0 term) for 21.7° and 22.4° incidence (upper panels) and 47.4° and 47.8° incidence (lower panels), VV-polarization (left panels) and HH-polarization (right panels). A_0 data are shown as filled circles with the standard deviation of A_0 estimates from all wind vector cells shown as the error bars. GMFs shown where valid are IWRAP (dashed), CMOD5.n (dash-dotted), CMOD5.h (long dashes), and C-2013 (dotted). The new IWRAP GMF is shown as a solid line.

GMF and the data. As described in section 3.3.4, A_0 estimates within a small wind speed range from each season are aligned vertically to match an existing IWRAP GMF in an attempt to remove calibration errors. The closest GMFs to the data at 22° is the 29° (VV) and 31° (HH) IWRAP models. While this procedure makes the calibration offset of each flight experiment the same, it does not necessarily remove the offsets. In this case these GMFs may not represent the mean NRCS at 22°, so some residual calibration error remains. Here it is assumed that the CMOD5.n GMF more closely approaches the true A_0 value in the $25\,\mathrm{m\,s^{-1}}$ to $27.5\,\mathrm{m\,s^{-1}}$ wind speed range, so the data and IWRAP GMFs in this range are aligned to CMOD5.n. At HH-polarization, the alignment includes the polarization ratio from Vachon and Wolfe [6].

Backscatter from the ocean surface by near-nadir-looking radars have been modeled well with quasi-specular scattering models. As the incidence angle draws closer to nadir, increasing roughness (e.g., due to the wind speed increasing) results in less power being scattered back to the radar. Somewhere between 0° and 10° to 20°, backscatter from the ocean surface is produced by a mixture of specular and tilted Bragg resonance diffraction processes [46]. At about 20°, the transition between the geometric optics (or facet-scattering) and Composite Bragg regimes occurs. In these two regimes there is a wind speed that, depending on the incidence angle, is the upper limit for increase in NRCS [30], [46]. The inner incidence angles show this saturation at low wind speeds, relative to the other incidence angles shown, with a continuing decrease in mean NRCS as wind speed increases.

The new data do not match the existing IWRAP GMF at the low incidence angles, as there is a significant difference in incidence angle between the GMF and observation angle. CMOD5.n slightly overestimates the mean NRCS, but the GMF was not developed with data for incidence angles less than 25°.

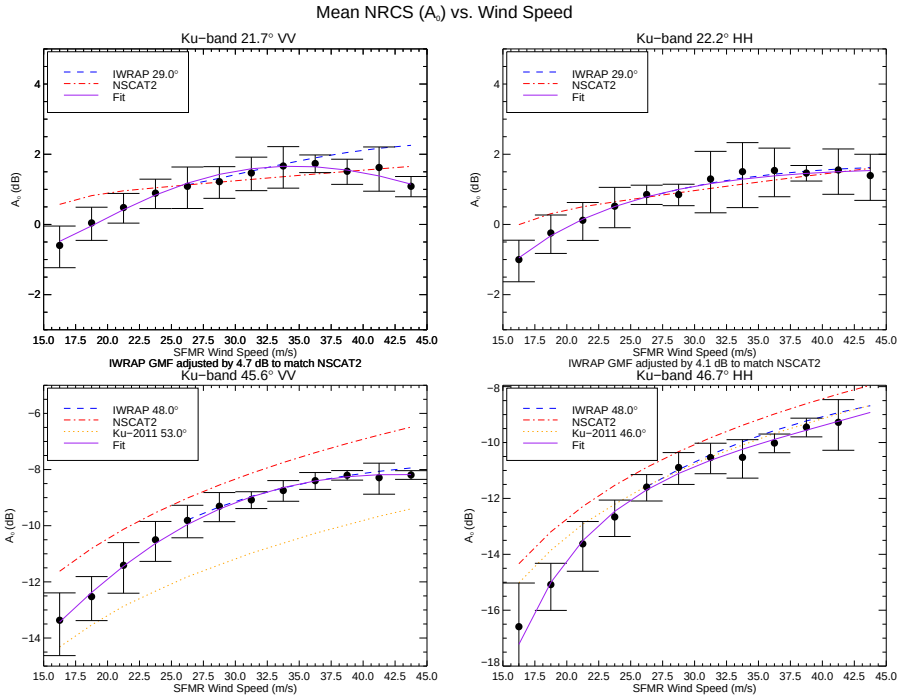

Figure 3.16. Ku-band mean NRCS vs. wind speed (A_0 term) for 21.7° and 22.2° incidence (upper panels) and 45.6° and 46.7° incidence (lower panels), VV-polarization (left panels) and HH-polarization (right panels). A_0 data are shown as filled circles with the standard deviation of A_0 estimates from all wind vector cells shown as the error bars. GMFs shown where valid are IWRAP (dashed), NSCAT2 (dash-dotted), and Ku-2011 (dotted). The new IWRAP GMF is shown as a solid line.

The polarization ratio applied to obtain HH-polarized C-band model functions is a simple one that is only dependent on incidence angle and not wind speed. As a result, it will not have an effect on the shape of the GMF as shown here; it is only a vertical shift. The difference in backscattered power between the two co-polarized signals is small at low incidence angles. The model used here predicts approximately 0.3 dB at 22° incidence. As the incidence angle decreases, VV- and HH-polarized NRCS should increase in similarity as there are fewer differences between the orientation of the fields with respect to the ocean surface. The observations indicate that saturation wind speeds at both polarizations are similar at approximately $30\,\mathrm{m\,s^{-1}}$. Beyond the saturation wind speed, HH-polarization shows a marked decrease in A_0 while VV-polarization shows a slight decrease.

Figure 3.16 shows the Ku-band A_0 estimates, Ku-band GMFs, and fits to the estimates. As above, the Ku-2011 GMF is shown for the outer incidence angles even though they are not the same as what was measured by IWRAP. They are all close enough for comparison at the outer incidence angle HH-polarization. The NSCAT2 algorithm is shown as a dash-dotted line and is used as the final calibration offset, like CMOD5.n is used above.

The saturation effect is less obvious at Ku-band. Unlike at C-band, Ku-band HH-polarized data better match the nearest IWRAP GMFs despite the large difference in incidence angle. Though this is not the expected geophysical behavior, the Ku-band HH-pol IWRAP GMF has a flatter response than does the VV-pol GMF. Both GMFs saturate at the same wind speed, but the VV-pol GMF is steeper than HH-pol both below and above the saturation speed. It is known that as the incidence angle draws closer to nadir, the slope of the A_0 response to wind speed becomes negative, which results in higher NRCS at lower wind speeds. Near 20° incidence, this effect may begin to manifest itself as a lower saturation wind speed and a low slope in A_0 with wind speed. As a result, for low incidence angle measurements at Ku-band the IWRAP HH-pol GMF will be closer to the data than the VV-pol GMF. This is primarily due to the relatively low slope of the IWRAP HH-pol A_0 GMF. More data is needed to verify the results at the highest wind speeds observed.

As at C-band, the outer incidence angles closely follow the high-incidence-angle IWRAP GMFs above $25\,\mathrm{m\,s^{-1}}$. The VV-polarization data may start saturating around $40\,\mathrm{m\,s^{-1}}$, which is not predicted by any of the models shown (though IWRAP 48° is close). On the low end of the data, the fit to the means has a steeper slope than either Ku-2011 or NSCAT2. This is unexpected since GMFs developed from space-borne scatterometers typically have good skill at wind speeds below $25\,\mathrm{m\,s^{-1}}$. While this may be due to the use of SFMR winds at these speeds, as the brightness temper-

ature dependence on wind speed is relatively weak in this region, the close correlation with satellite-based GMFs at C-band seem to refute this explanation.

3.5.3 Response of Higher-Order Coefficients to Wind Speed

Figure 3.17 shows C-band a_1 estimates, a fit to these estimates, and the IWRAP GMF a_1 function. The fit uses the parameterization of (3.7) and the parameters to the fits are given in table 3.5. A_1 is first normalized by A_0 (i.e. $a_1 = \frac{A_1}{A_0}$) by convention. With either A_1 or a_1 the effect of wind speed on the upwind/downwind anisotropy can be observed.

CMOD5.n uses a slightly different model for NRCS with respect to the wind-relative azimuth, χ:

$$\begin{aligned} \sigma^0(\chi) &= \left(\sum_{i=0}^{2} B_{i_Z} \cos(i\,\chi) \right)^{1.6} \\ &\approx B_{0_Z}^{1.6} \left(1 + 1.6\,H + 0.48\,H^2 \right), \end{aligned} \tag{3.12}$$

where $H = b_{1_Z} \cos(\chi) + b_{2_Z} \cos(2\chi)$ [11]. The subscript Z indicates the coefficient is in "z-space" as opposed to NRCS-space of the traditional formulation. Reducing the terms to single harmonics, they obtain an NRCS equation with five harmonics, the highest four of which are

$$b_1 = 1.6 b_{1_Z} + 0.48 b_{1_Z} b_{2_Z} \tag{3.13}$$

$$b_2 = 1.6 b_{2_Z} + 0.24 b_{1_Z}^2 \tag{3.14}$$

$$b_3 = 0.48 b_{1_Z} b_{2_Z} \tag{3.15}$$

$$b_4 = 0.24 b_{2_Z}^2. \tag{3.16}$$

The fourth and fifth harmonics are small, so they are neglected in the upwind/downwind and upwind/crosswind analyses. Note that these curves are the same as what they

would be for CMOD5.h, since both GMFs have identical b_1 and b_2 behavior. As these lower angles are beyond the designed incidence angle range of CMOD5.n, it is not expected to be an excellent physical description. It is close enough, however, to provide a confirmation of the validity of the derived models.

The a_1 term for the inner incidence angles are almost 0 for all wind speeds observed. This can be seen in the nearly equal peaks of figures 3.7 and 3.8. The Ku-band response in figure 3.18 is about the same. The outer angles show a general downward trend with increasing wind speed. The upwind and downwind peaks are expected to get closer with increasing wind speed, which would result in an a_1 term approaching 0. The methodology used in this dissertation prevents a_1 from going negative, since the peak NRCS in a wind vector cell is assumed to be the upwind direction. As a result, a geophysical change in the response with wind speed of the first harmonic may be masked. Any negative a_1 presented here can be attributed to statistical variation.

In both figures 3.19 and 3.20, there is a trend downward towards 0 with wind speed after an initial peak within $15\,\mathrm{m\,s^{-1}}$ to $22.5\,\mathrm{m\,s^{-1}}$. Fits to the data are also shown as a solid line, the parameters for which are listed in table 3.6. Since the a_2 coefficient affects the resulting NRCS most when combined with a_1, these results are examined more closely as the normalized upwind/crosswind difference. This measure is calculated from a combination of a_1 and a_2, in figures 3.21 and 3.22. This is also performed with the existing GMFs when possible.

In figure 3.21, the slope of the VV curves of the fits to the data at C-band are similar to those of CMOD5.n across the wind speed range. However, the IWRAP GMF is predicting different behavior in all polarization and incidence angle configurations. Both CMOD5.n and the recent data show a consistent decrease in upwind/crosswind sensitivity after approximately $27.5\,\mathrm{m\,s^{-1}}$, while the IWRAP GMF shows a slight increase. At the higher incidence angles, the decrease in this difference begins at a higher wind speed in HH-polarization relative to VV. However, once the upwind and

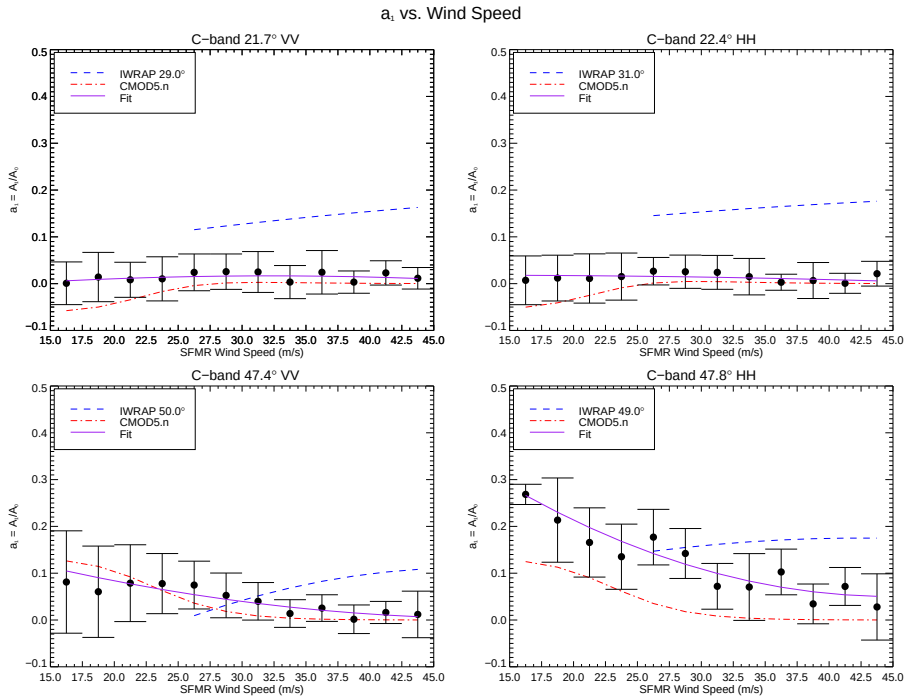

Figure 3.17. C-band a_1 term ($\frac{A_1}{A_0}$) of the NRCS vs. wind speed for 21.7° and 22.4° incidence (upper panels) and 47.4° and 47.8° incidence (lower panels), VV-polarization (left panels) and HH-polarization (right panels). a_1 data are shown as filled circles with the standard deviation of a_1 estimates from all wind vector cells shown as the error bars. GMFs shown where valid are IWRAP (dashed) and CMOD5.n (dash-dotted). Note that CMOD5.h has the same a_1 response as CMOD5.n. The new IWRAP GMF is shown as a solid line.

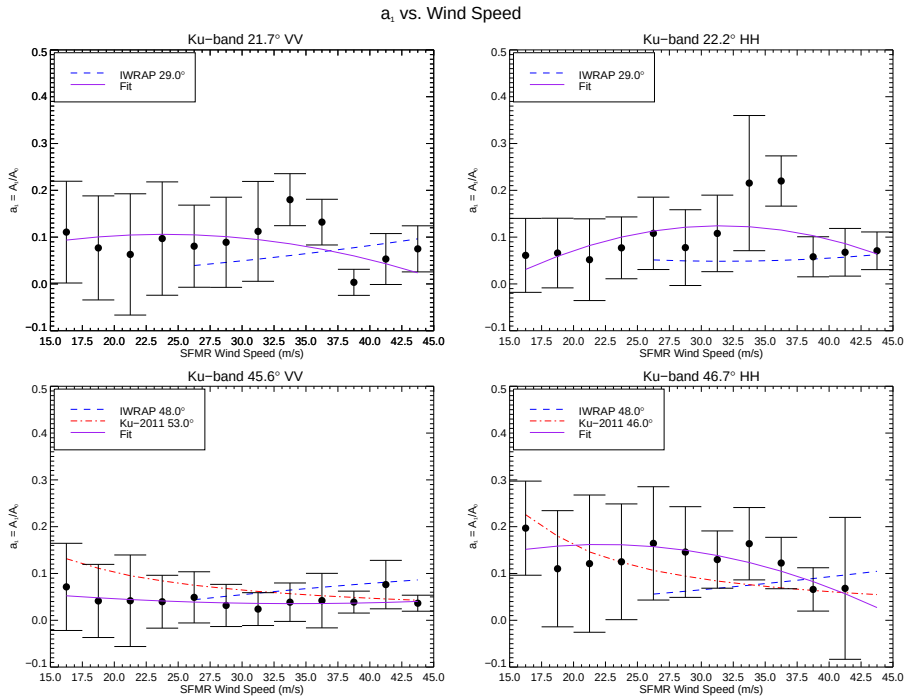

Figure 3.18. Ku-band a_1 term ($\frac{A_1}{A_0}$) of the NRCS vs. wind speed for 21.7° and 22.2° incidence (upper panels) and 45.6° and 46.7° incidence (lower panels), VV-polarization (left panels) and HH-polarization (right panels). a_1 data are shown as filled circles with the standard deviation of a_1 estimates from all wind vector cells shown as the error bars. GMFs shown where valid are IWRAP (dashed) and Ku-2011 (dash-dotted). The new IWRAP GMF is shown as a solid line.

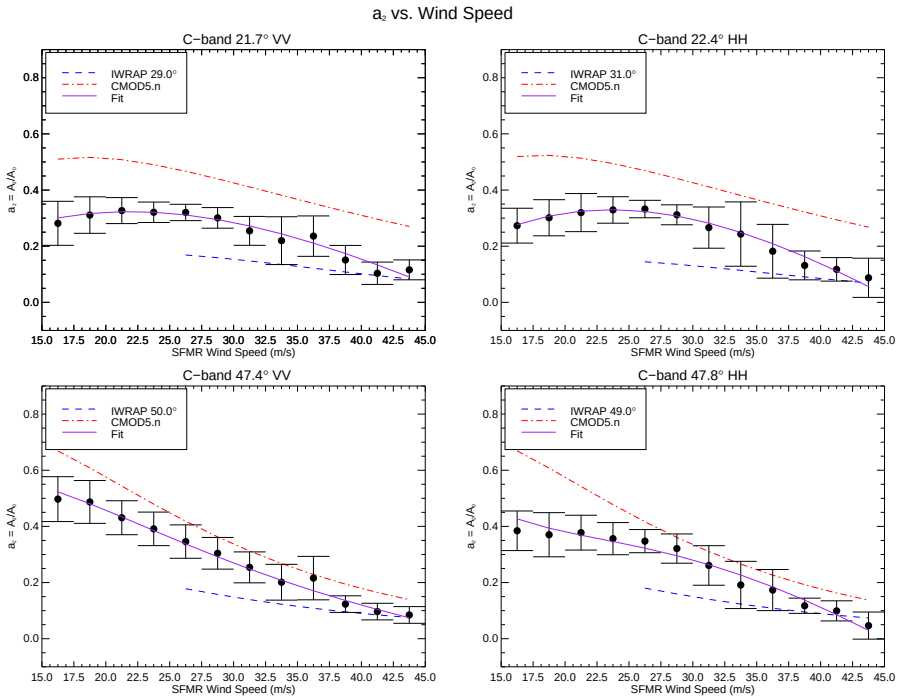

Figure 3.19. C-band a_2 term ($\frac{A_2}{A_0}$) of the NRCS vs. wind speed for 21.7° and 22.4° incidence (upper panels) and 47.4° and 47.8° incidence (lower panels), VV-polarization (left panels) and HH-polarization (right panels). a_2 data are shown as filled circles with the standard deviation of a_2 estimates from all wind vector cells shown as the error bars. GMFs shown where valid are IWRAP (dashed) and CMOD5.n (dash-dotted). Note that CMOD5.h has the same a_1 response as CMOD5.n. The new IWRAP GMF is shown as a solid line.

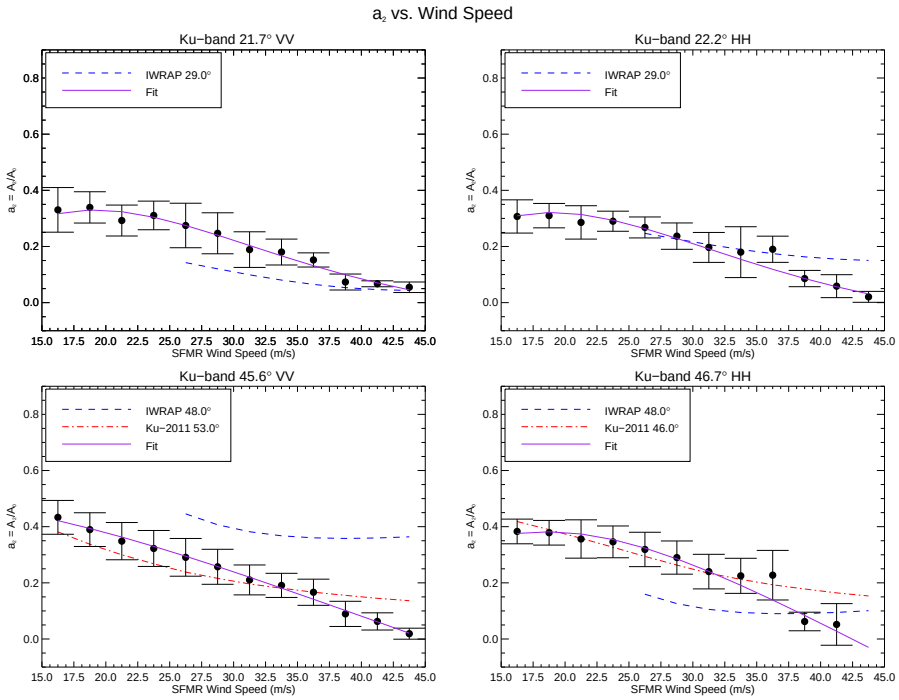

Figure 3.20. Ku-band a_2 term ($\frac{A_2}{A_0}$) of the NRCS vs. wind speed for 21.7° and 22.2° incidence (upper panels) and 45.6° and 46.7° incidence (lower panels), VV-polarization (left panels) and HH-polarization (right panels). a_2 data are shown as filled circles with the standard deviation of a_2 estimates from all wind vector cells shown as the error bars. GMFs shown where valid are IWRAP (dashed) and Ku-2011 (dash-dotted). The new IWRAP GMF is shown as a solid line.

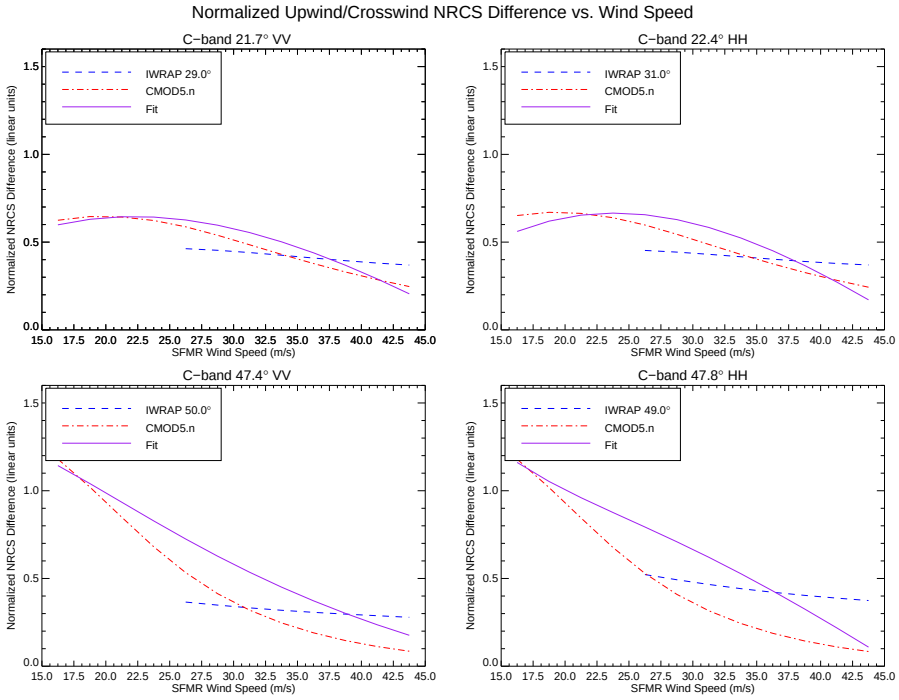

Figure 3.21. C-band upwind NRCS less crosswind NRCS vs. wind speed, calculated according to (3.5). σ^0 is divided by A_0 (in linear units) for ease of display. The new IWRAP GMFs are shown as a solid line. The existing IWRAP GMFs are shown as a dashed line and CMOD5.n is shown as a dash-dotted line. The trend of the new IWRAP GMFs matches better with CMOD5.n than with the existing IWRAP GMFs.

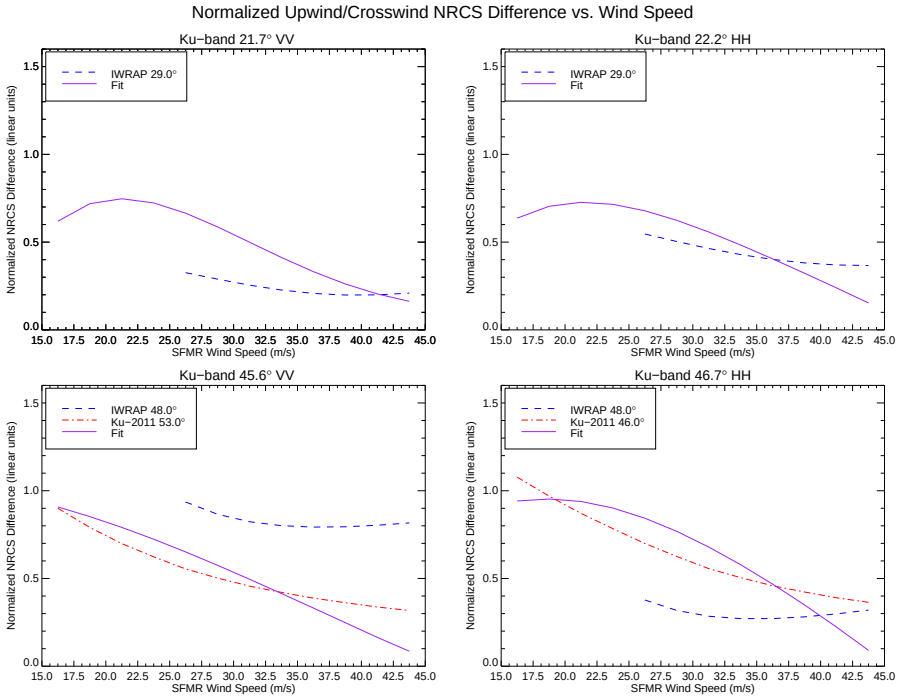

Figure 3.22. Ku-band upwind NRCS less crosswind NRCS vs. wind speed, calculated according to (3.5). σ^0 is divided by A_0 (in linear units) for ease of display. The new IWRAP GMFs are shown as a solid line. The existing IWRAP GMFs are shown as a dashed line and Ku-2011 is shown as a dash-dotted line. The trend of the new IWRAP GMFs matches better with Ku-2011 than with the existing IWRAP GMFs.

crosswind peaks start to converge (towards a difference of 0), they do so at about the same rates for each polarization. The inner incidence angles show nearly the same response, with the exception of a slight increase with wind speed under $22.5\,\mathrm{m\,s^{-1}}$.

At Ku-band, there are no suitable GMFs at low incidence angles with which the data and existing IWRAP GMF can be compared. At the outer incidence angles, the parameters of the Ku-2011 GMF are available though they are not an exact incidence angle match. With the possible exception of the inner angle HH-polarization behavior, the IWRAP GMF indicates that upwind and crosswind are only beginning to diverge at the highest wind speeds observed here. These data, however, indicate that the opposite is happening (the upswing at the tail end of the 22.2° HH-polarization and outer incidence angle curves are probably anomalous and due to the small a_2 values in the denominator of (3.5)). As at C-band, the peaks of the revised Ku-band GMF at the inner incidence angles diverge as wind speed increases up to approximately $30\,\mathrm{m\,s^{-1}}$, at which point they start converging. The outer incidence angles are converging as expected at high wind speeds. Though the incidence angles do not match, the new GMF is nearly on top of the Ku-2011 VV-polarization model. HH-polarization is a little further from the trend of Ku-2011, even though the incidence angles are closer. This is probably due to the more pronounced errors in a_2 at HH-polarization compared with VV. Overall, combined with figures 3.17 and 3.18 these figures show that the new GMFs are flattening appropriately in azimuth as wind speed increases.

3.6 Conclusion

The sources of variability in NRCS were discussed and of them, the three sources that likely have the largest effect are sea state, calibration offset, and sample timing. All IWRAP data with apparent NRCS or SFMR discrepancies have been discarded. Calibration offset has been addressed by adjusting the mean NRCS within a wind speed bin of each flight to a fixed point. Sea state remains a variable unaccounted for.

Table 3.4. IWRAP-2014 GMF Coefficients: A_0 Parameters

Radar	Pol.	Incidence Angle (°)	β	γ_0	γ_1	γ_2
C-band	VV	21.7	−4.3615	5.6893	−1.8614	0.0000
		47.4	−5.8167	5.4379	−1.4637	0.0000
	HH	22.4	−4.2825	5.5676	−1.8549	0.0000
		47.8	−3.1785	1.3264	−0.0516	0.0000
Ku-band	VV	21.7	14.7260	−34.8520	26.8530	−6.7277
		45.6	7.1943	−23.0350	19.2220	−4.9728
	HH	22.2	−3.5759	4.9144	−1.8948	0.1736
		46.7	−33.1650	59.6370	−37.5150	8.0182

Table 3.5. IWRAP-2014 GMF Coefficients: a_1 Parameters

Radar	Pol.	Incidence Angle (°)	c_1	c_2	c_3
C-band	VV	21.7	$-2.6469 \cdot 10^{-2}$	$2.6808 \cdot 10^{-3}$	$-4.1653 \cdot 10^{-5}$
		47.4	$2.2374 \cdot 10^{-1}$	$-8.7238 \cdot 10^{-3}$	$8.6215 \cdot 10^{-5}$
	HH	22.4	$1.6379 \cdot 10^{-2}$	$2.7388 \cdot 10^{-4}$	$-1.1686 \cdot 10^{-5}$
		47.8	$5.7984 \cdot 10^{-1}$	$-2.3559 \cdot 10^{-2}$	$2.6196 \cdot 10^{-4}$
Ku-band	VV	21.7	$-1.3531 \cdot 10^{-2}$	$9.9988 \cdot 10^{-3}$	$-2.0911 \cdot 10^{-4}$
		45.6	$9.6345 \cdot 10^{-2}$	$-3.5504 \cdot 10^{-3}$	$5.1868 \cdot 10^{-5}$
	HH	22.2	$-2.7357 \cdot 10^{-1}$	$2.5252 \cdot 10^{-2}$	$-4.0074 \cdot 10^{-4}$
		46.7	$1.7809 \cdot 10^{-2}$	$1.2974 \cdot 10^{-2}$	$-2.9164 \cdot 10^{-4}$

Table 3.6. IWRAP-2014 GMF Coefficients: a_2 Parameters

Radar	Pol.	Incidence Angle (°)	d_1	d_2	d_3	d_3
C-band	VV	21.7	$-6.1008 \cdot 10^{-2}$	$3.7422 \cdot 10^{-2}$	$-4.8253 \cdot 10^{-2}$	$5.00 \cdot 10^{1}$
		47.4	$3.3084 \cdot 10^{-1}$	$5.4715 \cdot 10^{-2}$	$-6.1795 \cdot 10^{-2}$	$1.90 \cdot 10^{1}$
	HH	22.4	$-3.0359 \cdot 10^{-1}$	$5.7838 \cdot 10^{-2}$	$-7.0479 \cdot 10^{-2}$	$5.00 \cdot 10^{1}$
		47.8	$1.4737 \cdot 10^{0}$	$-1.4053 \cdot 10^{-1}$	$1.0970 \cdot 10^{-1}$	$1.90 \cdot 10^{1}$
Ku-band	VV	21.7	$-6.6809 \cdot 10^{-1}$	$1.2550 \cdot 10^{-1}$	$-1.1700 \cdot 10^{-1}$	$2.60 \cdot 10^{1}$
		45.6	$7.3953 \cdot 10^{-1}$	$-4.8272 \cdot 10^{-2}$	$3.1864 \cdot 10^{-2}$	$1.10 \cdot 10^{1}$
	HH	22.2	$-6.5264 \cdot 10^{-1}$	$1.2300 \cdot 10^{-1}$	$-1.1506 \cdot 10^{-1}$	$2.60 \cdot 10^{1}$
		46.7	$1.0235 \cdot 10^{0}$	$-1.8434 \cdot 10^{-1}$	$1.6037 \cdot 10^{-1}$	$1.10 \cdot 10^{1}$

A change in the wind speed retrieval algorithm of the SFMR and how this affected the development of the original IWRAP GMF was also described. At wind speeds below about $58\,\mathrm{m\,s^{-1}}$, the existing IWRAP GMF overestimates the wind speed and above $58\,\mathrm{m\,s^{-1}}$ it underestimates the wind speed. The coefficients were then remapped using the new SFMR wind-speed dependent excess emissivity model to correct this behavior.

Existing scatterometer geophysical model functions at C- and Ku-band do not cover incidence angles below 25°. Spaceborne, near-nadir meteorological radars, such as the Precipitation Radar (PR) on the Tropical Rainfall Measuring Mission (TRMM), have observed NRCS from nadir up to about 20°. Scattering from the ocean in the incidence angle region between 20° and 25° has not been studied extensively. The IWRAP GMF has been extended down to 22° for both C- and Ku-band and VV- and HH-polarizations, bringing to light some interesting scattering effects. The geometric optics model may help to explain relatively early onset of saturation and subsequent reduction in C-band NRCS at 22°, compared to the higher incidence angles. The same effect is not obvious at these angles for the Ku-band radar, but saturation still occurs between $30\,\mathrm{m\,s^{-1}}$ and $40\,\mathrm{m\,s^{-1}}$.

The A_0 term of the existing IWRAP GMF at approximately 50° generally matches the more recent data up to $45\,\mathrm{m\,s^{-1}}$, within the uncertainty of the measurements. However, the new a_1 and a_2 terms at these incidence angles disagree with the existing IWRAP model. The new data are more similar to the a_1 and a_2 terms of the CMOD5.n and Ku-2011 GMFs, models developed using data from spaceborne instruments. The methodology limits a_1 to a positive number, but this is likely a valid assumption for these incidence angles and wind speeds. Close agreement of the new upwind/crosswind difference to these satellite-based GMFs was also observed, and this difference also disagrees with the existing IWRAP GMF. Overall, evidence presented here supports

maintaining the A_0 IWRAP model and revising the a_1 and a_2 models at the incidence angles close to 50° at both C- and Ku-band.

CHAPTER 4

PRECIPITATION SPLASH EFFECTS ON HIGH-SPEED OCEAN-SURFACE WIND VECTOR MEASUREMENTS

4.1 Introduction

Backscattered electromagnetic power from the ocean surface is, in the most basic sense, a measure of roughness at a specific wavelength. At incidence angles between approximately 20° and 70°, a smooth surface scatters most of the power forward, away from the transmitter, while rougher surfaces scatter an increasing amount of power back towards the source. Scatterometers operate within these incidence angles so they can reliably measure the rough ocean surface. The surface roughness also depends on the wavelength of the electromagnetic wave being used to observe the ocean. At these incidence angles primarily used by scatterometers, the main source of scattering is the small-scale waves on the order of half of the wavelength of the transmitted wave (1.875 cm to 3.75 cm at C-band and 0.9375 cm to 1.25 cm at Ku-band). This is called the Composite Surface Model or Composite Bragg Model. In this model, the scatterers on top of the larger waves, which increase with wind speed, resonate with the radar wave and scatter power back to the radar.

In the absence of precipitation, surface wind is one of the main drivers of ocean roughness observed by radar scatterometers, with surface currents and other ocean features (e.g., wave height) providing a secondary effect. Precipitation corrupts scatterometer measurements by (1) attenuating the signal both to and from the surface; (2) scattering the signal both to and from the surface; and (3) making the surface appear rougher than if it were a result of wind forcing alone (i.e., the splash effect).

As a result, a variety of methods have been developed to exclude precipitation from measurements made by spaceborne scatterometers so the ocean surface wind vector can be retrieved in a predictable manner [4]. The effect of precipitation on the ocean surface is complicated, with additional features such as ring waves and stalks being created as a result of the impact [47], [48]. These features modify the roughness that was once largely due to wind speed, but the degree to which these modifications impact wind vector retrieval, especially at high wind speeds, are still uncertain. A recent summary article on the effects of precipitation on satellite sensors of ocean winds states that "there is a significant need for improved wind speed and wind stress calculations, along with more accurate rain-flagging techniques [4]."

Radar scatterometers that operate in the Ku-band can provide spatially sensitive ocean-surface observations compared to C-band instruments. However, electromagnetic waves at Ku-band wavelengths are more sensitive to attenuation and scattering by rain than are those at C-band. Recent studies of Ku-band scatterometers have shown that at low wind speeds, the impact of precipitation on the surface increases the observed normalized radar cross-section (NRCS) and the influence is greater as the incidence angle increases [47], [49]. They also show that rain effects are isotropic and tend to increase the error in wind direction retrieval. However, the effect on wind speed is not necessarily of the same magnitude. At higher wind speeds, the modulation of NRCS in azimuth is small enough that any disturbance will impact the direction retrieval, but the effect on the mean NRCS in azimuth may not be significantly different. Weissman and Bourassa [50] have investigated the impact of rainfall in high winds on ocean-surface NRCS observed by satellite, and they see a limit to the roughening effect due to precipitation splash. They also note an apparent splash effect on HH-polarized NRCS up to wind speeds in the $30\,\mathrm{m\,s^{-1}}$ to $35\,\mathrm{m\,s^{-1}}$ range, but no apparent effect on VV-polarized NRCS.

There are varied results in the literature for C-band scatterometers. A preliminary study of data from the Imaging Wind and Rain Airborne Profiler (IWRAP) concluded that C-band HH-polarized NRCS is not significantly affected by the splash of rain on the ocean surface [51]. A recent study using data from ASCAT show a degradation of quality in satellite-retrieved winds for rain rates above $6\,\mathrm{mm\,h^{-1}}$. They do not rule out splash effects, but suggest that this could also be due to "rain-induced wind-related effects, such as downbursts and/or convergence [3]."

Even at C-band, where attenuation by precipitation is generally neglected, the splash effect on backscattered power in high winds is not well understood. In high winds, where the modification of the ocean-surface roughness by precipitation can probably be neglected, the attenuation and scattering of the Ku-band signal both to and from the surface are significant. To overcome the known limitations of Ku-band scatterometers while retaining the benefits, future scatterometer designs (e.g., the Dual-Frequency Scatterometer (DFS) [52] and proposed Extended Ocean Vector Wind Mission (XOVWM) solutions [53]) will likely incorporate both C- and Ku-band into the system design. The hypothesis in this chapter is that there is a limit on wind speed, above which the effect of splash due to precipitation on the ocean surface NRCS is negligible.

4.2 Remote Sensing of Precipitation

4.2.1 Volume Scattering

Sampling a volume of scatterers is slightly different than surface scattering. Assuming that the receiver bandwidth is at least an order of magnitude larger than τ, each sample taken by a radar after transmitting a rectangular pulse will contain echoes from only those objects within a range of $\frac{c\tau}{2}$. However, there is now a volume of contributors to the echo power bounded in elevation and azimuth by the beamwidths

of the antenna. In order to normalize this value, a backscattering cross-section per unit volume, or reflectivity, is defined as

$$\eta(r) = \int_0^\infty \sigma(D) N(D, r)\, \mathrm{d}D, \tag{4.1}$$

where $\sigma(D)$ is the expected RCS for a hydrometeor of diameter D and $N(D, r)$ is the drop size distribution at a range r. The mean signal power from the volume is

$$\bar{P}(r_0) = \int_0^{r_2} \int_0^{\pi} \int_0^{2\pi} \eta(r) I(r_0, r) r^2\, \mathrm{d}r \sin\theta\, \mathrm{d}\theta\, \mathrm{d}\phi, \tag{4.2}$$

where $I(r_0, r)$ is the range-weighting function or pulse shape. When the range to the volume is large compared to $\frac{c\tau}{2}$, the antenna beam is a two-dimensional Gaussian, and it is assumed that the reflectivity and attenuation due to hydrometeors is constant, (4.2) can be simplified to

$$\bar{P(r_0)} \approx \frac{P_t G^2 \lambda^2\, \eta(r_0)\, \pi \theta_e \phi_a}{(4\pi)^3 r_0^2\, l(r_0)^2\, (8 \ln 2)} \tag{4.3}$$

where l is the one-way loss due to attenuation and scattering and θ_e and ϕ_a are the elevation and azimuthal beamwidths, respectively. The $8 \ln 2$ factor in the denominator is a factor to normalize the antenna gain across the Gaussian-shaped beam, so this only applies for pencil-beam radars.

When the diameter of a hydrometeor of diameter D is small compared to the wavelength λ, the Rayleigh approximation can be made for the RCS of the drop [54]:

$$\sigma(D) \approx \frac{\pi^5}{\lambda^4} |K_m^2| D^6, \tag{4.4}$$

where $K_m = \frac{m^2 - 1}{m^2 + 2}$ and $m = n - jn\kappa$, the complex refractive index of water. n is the refractive index of water and κ is the attenuation index. Substituting (4.4) into (4.1),

$$\eta(r) = \frac{\pi^5}{\lambda^4} |K_m^2| Z_e, \tag{4.5}$$

where Z_e is called the "equivalent reflectivity factor." Because the Rayleigh approximation may not apply at the wavelengths used in the IWRAP systems, the term "equivalent" (and subscript e) is used. Z_e is the meteorological parameter of interest, though η could just as easily be chosen. Equations (4.3) and (4.5) are used to express Z_e in terms of the measured average power of a volume in range:

$$Z_e(r_0) = \frac{P(\bar{r}_0)\, l(r_0)^2\, r_0^2}{P_t} \frac{\lambda^2 2^{10} \ln 2}{G^2 \theta_e \phi_a c\tau |K_w|^2 \pi^3}. \tag{4.6}$$

Note that most of (4.6) is only dependent on the radar and not the observed scene. This is sometimes referred to as the "radar constant" in discussions of measured reflectivity factors.

4.2.2 Dual-Frequency Attenuation Estimation

In section 4.1, it was noted that precipitation modifies scatterometer measurements in three ways: attenuation of the round-trip signal, scattering of the same, and the splash effect. Also worth repeating is that Ku-band frequencies are more sensitive to the former two effects and C-band scatterometers are relatively unaffected. So in order to evaluate the effect of precipitation impact on sea-surface NRCS, any attenuation of the backscattered power from the surface echo at Ku-band must be corrected. To do so, the mean attenuation rate per unit range ($\bar{K}_s$) of the intervening volume must be known. While it is possible to accomplish this with just the Ku-band radar (c.f. Fujita and Satake [55]), some parameters in the Z–R and K_s–R relationships must be assumed. Since the parameters in Z–R relationships are dependent on precipitation type and local climate, this would likely introduce some error into the analysis. However, $\bar{K}_s$ can be derived from two collocated radars without assuming any other parameters. The two radars must measure a similar volume within a short amount of time of each other, and one of them must be non-attenuating [56]. Here both the C- and Ku-band radars on IWRAP are used to evaluate the rain rate re-

trievals of Stepped Frequency Microwave Radiometer (SFMR). Doing so, $\bar{K}_s$ models can also be evaluated as functions of SFMR rain rate. Hail is assumed to be absent so that all scatterers can be assumed to be in the Rayleigh regime. As a result of this Rayleigh assumption, the equivalent reflectivity factors at both C- and Ku-band are assumed to be equal in the absence of attenuation. That is, the l component of (4.6) is neglected.

The attenuation factor A in the backscattered power observed by the radar over the range r_0 to $r_1\,(= r_0 + s)$ is

$$A = 10^{\left(-0.2 \int_{r_0}^{r_1} K_s(r)\,\mathrm{d}r\right)}, \tag{4.7}$$

where K_s is the one-way specific attenuation in dB per unit range, the units of which are taken to be km. The attenuation observed at each range gate is a function of the media through which the radar is observing; if there is a varying amount of precipitation in the region s, then K_s will not be constant. The average, or effective, amount of attenuation observed will be sufficient for the analysis here since the goal is to understand how the precipitation is measured by SFMR.

The mean backscattered powers P_{C} and P_{Ku} from an illuminated volume at a range r_1 (km) are given by

$$P_{\mathrm{C}}(r_1) = \frac{C_{\mathrm{C}}}{r^2}\, Z(r_1) \tag{4.8}$$

$$P_{\mathrm{Ku}}(r_1) = \frac{C_{\mathrm{Ku}}}{r^2}\, Z(r_1) \cdot 10^{\left(-0.2 \int_{r_0}^{r_1} K_s(r)\,\mathrm{d}r\right)}, \tag{4.9}$$

where C_{C} and C_{Ku} are the radar constants including any attenuation up to r_0, the observed volume is contained in the range r_0 and r_1, Z is the (non-attenuated) equivalent reflectivity factor, and K_s is the one-way specific attenuation, assumed to be applicable only at Ku-band.

The logarithm of the ratio of (4.8) to (4.9) yields an expression for $\bar{K_s}$ over the volume sampled from range r_0 to r_1,

$$10\log\left(\frac{\left(\frac{P_{\mathrm{C}}(r_1)}{C_{\mathrm{C}}}\right)}{\left(\frac{P_{\mathrm{Ku}}(r_1)}{C_{\mathrm{Ku}}}\right)}\right) = 2\int_{r_0}^{r_1} K_s(r)\,\mathrm{d}r, \tag{4.10}$$

but the constants C_{C} and C_{Ku} still remain. These constants are difficult to determine, even with precise calibration. At a more distant range ($r_2 = r_1 + s'$), the specific attenuation can be written as the sum of two integrals,

$$2\int_{r_0}^{r_1} K_s(r)\,\mathrm{d}r + 2\int_{r_1}^{r_2} K'_s(r)\,\mathrm{d}r = 10\log\left(\frac{\left(\frac{P_{\mathrm{C}}(r_2)}{C_{\mathrm{C}}}\right)}{\left(\frac{P_{\mathrm{Ku}}(r_2)}{C_{\mathrm{Ku}}}\right)}\right), \tag{4.11}$$

where K'_s is the incremental attenuation rate from r_1 to r_2, and $P_{\mathrm{C}}(r_2)$ and $P_{\mathrm{Ku}}(r_2)$ are the mean backscattered powers measured at range r_2. Note that the equation still represents the attenuation from r_0, so $P_{\mathrm{C}}(r_2)$ and $P_{\mathrm{Ku}}(r_2)$ are still divided by the same constants C_{C} and C_{Ku}, respectively.

By subtracting (4.10) from (4.11), the mean incremental specific attenuation $\bar{K'_s}$ can be extracted while eliminating the radar constants (and, thus, any effect of attenuation up to r_0):

$$\begin{aligned}
2\int_{r_1}^{r_2} K'_s(r)\,\mathrm{d}r &= 10\log\left(\frac{\left(\frac{P_{\mathrm{C}}(r_2)}{C_{\mathrm{C}}}\right)}{\left(\frac{P_{\mathrm{Ku}}(r_2)}{C_{\mathrm{Ku}}}\right)}\right) - 10\log\left(\frac{\left(\frac{P_{\mathrm{C}}(r_1)}{C_{\mathrm{C}}}\right)}{\left(\frac{P_{\mathrm{Ku}}(r_1)}{C_{\mathrm{Ku}}}\right)}\right) \\
&= 10\log\left(\frac{\left(\frac{P_{\mathrm{C}}(r_2)}{C_{\mathrm{C}}}\right)}{\left(\frac{P_{\mathrm{Ku}}(r_2)}{C_{\mathrm{Ku}}}\right)} \cdot \frac{\left(\frac{P_{\mathrm{Ku}}(r_1)}{C_{\mathrm{Ku}}}\right)}{\left(\frac{P_{\mathrm{C}}(r_1)}{C_{\mathrm{C}}}\right)}\right) \\
&= 10\log\left(\frac{P_{\mathrm{C}}(r_2)}{P_{\mathrm{C}}(r_1)} \cdot \frac{P_{\mathrm{Ku}}(r_1)}{P_{\mathrm{Ku}}(r_2)}\right) \\
&= 2\bar{K'_s}s'.
\end{aligned} \tag{4.12}$$

To obtain the one-way mean specific attenuation $\bar{K_s}$ at Ku-band in $\mathrm{dB\,km^{-1}}$ through the volume sampled between ranges r_1 and r_2, the results of (4.12) are used:

$$\bar{K_s} = \frac{1}{2s'} 10 \log \left(\frac{P_{\mathrm{C}}(r_2)}{P_{\mathrm{C}}(r_1)} \cdot \frac{P_{\mathrm{Ku}}(r_1)}{P_{\mathrm{Ku}}(r_2)} \right) \qquad \left(\mathrm{dB\,km^{-1}} \right). \tag{4.13}$$

In the IWRAP data, profiles of the attenuated equivalent reflectivity factor, Z_e, are sometimes more readily available than those of the backscattered power. In this case, equations (4.8) and (4.9) can be rewritten in terms of Z_e as

$$Z_{e,C}(r_1) = Z(r_1) \tag{4.14}$$

$$Z_{e,Ku}(r_1) = Z(r_1) \cdot 10^{\left(-0.2 \int_{r_0}^{r_1} K_s(r)\, \mathrm{d}r \right)}. \tag{4.15}$$

Doing so, any $\frac{P}{C}$ term in the previous equations can be replaced by the corresponding Z_e. (4.13) can be rewritten as

$$\bar{K_s} = \frac{1}{2s'} 10 \log \left(\frac{Z_{e,C}(r_2)}{Z_{e,C}(r_1)} \cdot \frac{Z_{e,Ku}(r_1)}{Z_{e,Ku}(r_2)} \right) \qquad \left(\mathrm{dB\,km^{-1}} \right) \tag{4.16}$$

4.2.3 Reducing the Uncertainty of the $\bar{K_s}$ Measurement

Using only two samples in range from each radar beam to compute (4.16) results in a noisy measurement of $\bar{K_s}$. Multiple samples can be averaged in range and in volume to improve measurement accuracy [56]; however, this decreases the spatial resolution. The number of range-averages performed can be increased by making the region s' small (but no smaller than the pulse width τ—independent samples in range are required).

Consider a measurement of $\bar{K_s}$ calculated over a region s from independent samples of $Z_{e,C}$ and $Z_{e,Ku}$ at ranges r_1 and r_2 each. An independent measurement of $\bar{K_s}$, $\bar{K_s'}$, is performed at $(r_1' = r_1 + \frac{c\tau}{2})$ and $(r_2' = r_2 + \frac{c\tau}{2})$. This region has the same length as, and may even overlap with, the previous one, but because the samples of $Z_{e,C}$ and $Z_{e,Ku}$ used to compute $\bar{K_s'}$ are independent of $\bar{K_s}$, the result is an independent estimate of mean specific attenuation for the given profile.

4.3 Experiment Methodology

4.3.1 Path-averaged Specific Attenuation-SFMR Rain Rate Model

In evaluating path-averaged specific attenuation models and their performance as a function of SFMR rain rate, the rainy profiles observed by IWRAP must be isolated from the rain-free profiles. In order to have confidence that the ocean surface is being rained upon when rain is observed by the SFMR, observations are limited to incidence angles below 30°. For a typical altitude of 2.5 km, this keeps the azimuthal distance from the radar under 0.75 km even when considering the maximum pitch and roll of the aircraft allowed for this data set. SFMR retrieves rain rate within its beamwidth below the aircraft over all azimuths. Occasionally the aircraft flies near enough to a rain cell so that SFMR retrieves a non-zero rain rate, but IWRAP beams do not intersect with much of the cell. These collocations should be removed since the two instruments are not measuring the same event, so rain-flagged IWRAP samples are required in at least 75 % of each full scan.

The presence of rain in a particular profile is determined by way of a threshold on the range-averaged normalized Doppler spectrum width, $\hat{\sigma_{vn}}$ [21], [54]. This is calculated by

$$\hat{\sigma_{vn}} = \frac{1}{(R_2 - R_1 + 1)\pi\sqrt{2}} \sum_{i=R_1}^{R_2} \sqrt{-\ln \rho[i]}, \tag{4.17}$$

where R_1 and R_2 are the range gates closest to the aircraft and closest to the surface, respectively, and $\rho[i]$ is the pulse-pair correlation coefficient at range gate i. The threshold on $\hat{\sigma_{vn}}$ used for this analysis is 0.30, below which the radar beam is considered to be observing precipitation.

In aggregating the data, a correction to the NRCS is performed first based on instantaneous incidence angle. Chapter 5 shows the dependence of mean NRCS on incidence angle. Any small pitch or roll difference from horizontal results in an azimuthal modulation that is not a function of wind direction. In order to remove this modulation, the difference in modeled NRCS between the nominal incidence angle

and the instantaneous incidence angle is calculated. This difference is then added to the measured NRCS. At this point data is removed that is taken when the instantaneous incidence angle is more than $\pm 2^\circ$ off of the nominal incidence angle. This results in removal of less than 10 % of the available profiles.

The data is then organized into 360° scans to be paired between the C-band and Ku-band radars. Scans are only ever used once and are paired based on the minimum time and distance between observations. Once scans are paired based on minimum time and distance, the pairs are filtered based on time and distance between each observation. Since both antennas scan independently, only pairs that observe approximately the same scene are retained. The ideal scan period of either antenna is 1 s and the maximum ground speed (v_g) of the WP-3D is no greater than 200 m s^{-1}. So the range of scan periods allowed is 50 RPM to 70 RPM (1.2 s to 0.86 s per scan). If both antennas are pointing at opposite azimuth angles and spinning at the slowest scan period allowed, they will cover a similar volume within 0.6 s and 120 m of each other. If one antenna is spinning at 50 RPM and the other at 70 RPM, the slower antenna covers about 80 m more ground distance than the faster antenna. Therefore, scans between radars are considered to be collocated only if the mean time between observations is at most 0.6 s and both the minimum and maximum along-track distances between scans is at most 0.8 km. Figure 4.1 illustrates these requirements.

Finally, the data is grouped into 64 azimuth bins. Within each azimuth bin within each scan Z_e and σ_{vn}, among other aircraft variables and SFMR retrievals, are averaged together to form the analysis data set. Here the decision is made to keep or discard the scan, based on the fraction of precipitation observed by the radars in azimuth. If the scan contains at least 75 % of rainy profiles for both radars (using the threshold above), it is kept. An example of a rainy scan is shown in figure 4.2. It is a significant challenge to require the rain to be uniform, so the 75 % criteria is an

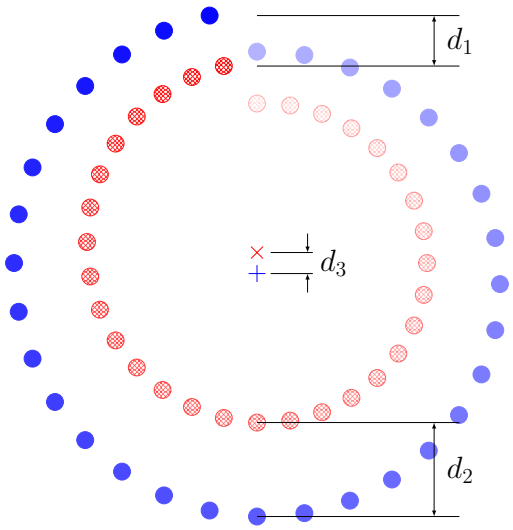

Figure 4.1. Schematic diagram of the limits placed on collocated C-band and Ku-band 360° scans. The C-band scans have the smaller scan radius with crosshatched circles representing the ocean surface illumination. The filled circles represent the surface illumination at Ku-band. The `X` symbol is the mean position of the aircraft during the C-band scan and the `+` symbol is the same for the Ku-band scan. The two scans shown here are offset in time by 0.5 s, illustrating a scenario in which the positions of the two antennas are not synchronized. For the two scans shown here, d_1 and d_2 must be at most 0.8 km each. This keeps the volumes of each scan close at typical altitudes (between 2 km and 3.4 km) and incidence angles of this dataset. Additionally, the time taken to traverse d_3 (e.g., $t = v_g \cdot d_3$) must be less than 0.6 s.

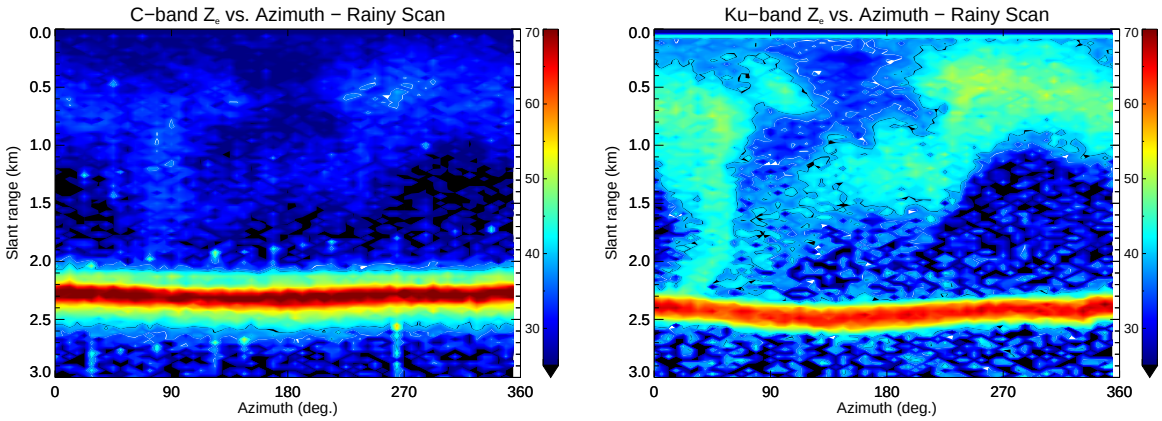

Figure 4.2. A rainy scan, having significant precipitation in at least 75 % of the scan. The left panel shows the equivalent reflectivity (Z_e) of the C-band radar, and the right panel shows the same for the Ku-band radar. The top of the plot is the range bin of the aircraft and the high-reflectivity horizontal stripe between 2 km to 2.5 km is the surface echo.

attempt to ensure the aircraft is in a rain cell. In this example, most of the scan has moderate precipitation between 1 km and 1.5 km.

Any reflectivity profiles that are not flagged as containing rain in this scan are removed. The remainder of the data are discarded; figure 4.3 shows an example of a discarded pair of scans. There is some rain in the profiles, but not heavy enough in the 90° to 270° range to be able to classify the scan as observing precipitation. The vertical stripes in range in the C-band scan is likely noise due to the lower fuselage radar operating on the WP-3D aircraft, which is also a C-band radar.

After collocating equivalent reflectivity profiles from the C- and Ku-band radars, the algorithm described in sections 4.2.2 and 4.2.3 is applied for entire scans. $\bar{K_s}'$ is averaged in range for about 0.7 km from the aircraft to obtain one value of $\bar{K_s}$ per azimuth bin. Then these $\bar{K_s}$ values are averaged over entire scans in azimuth to obtain the dataset used for matching with SFMR rain rates.

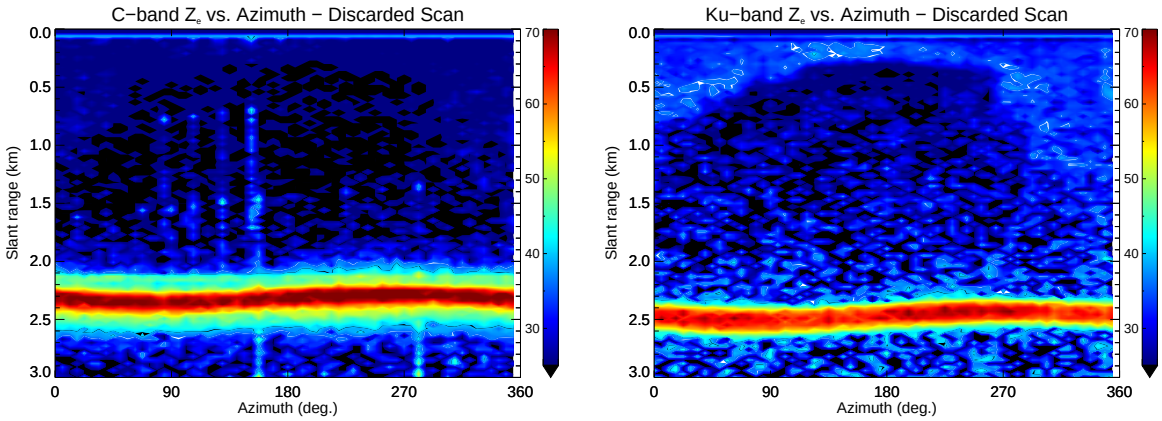

Figure 4.3. A discarded scan due to the presence of precipitation, but not in 75 % of the scan. The left panel shows the equivalent reflectivity (Z_e) of the C-band radar, and the right panel shows the same for the Ku-band radar. The top of the plot is the range bin of the aircraft and the high-reflectivity horizontal stripe between 2 km to 2.5 km is the surface echo.

4.3.2 Splash Effect

In order to analyze the effect of precipitation impact on NRCS, an approach is used similar to that in chapter 3. For the inner incidence angles of both IWRAP radars, collocated SFMR retrievals and IWRAP NRCS measurements are averaged into alongtrack cells of 2.5 km length. Each cell is divided into 64 track-relative azimuth bins, resulting in an average over 5.625° per bin. SFMR and some location data is associated with an alongtrack cell only when the aircraft is over the cell. Only radar data taken when the aircraft is level (incidence angle is within ±2° of nominal) is used. Before averaging NRCS samples, any incidence angle dependence is removed by referencing an existing geophysical model function (GMF).

In addition to collecting rain-free data, rainy data is also collected along with the SFMR-retrieved rain rate. Any data with a surface-echo SNR less than 5 dB is discarded to eliminate situations in which precipitation completely attenuates the signal. Only alongtrack cells with at least 75 % valid NRCS measurements are kept, so a good wind direction estimate can be obtained. These are then averaged and stored according to azimuth, SFMR wind speed, and SFMR rain rate. The wind speed and

rain rate bins into which data are stored are very fine: $0.5\,\mathrm{m\,s^{-1}}$ for wind speed and $1\,\mathrm{mm\,h^{-1}}$ for rain rate. This is done in order to make the datasets manageable while keeping specific information about the conditions with the NRCS. The bins can be (and are) averaged together into coarser bins later. The rain rate information is useful when correcting for attenuation due to precipitation.

Attenuation and scattering experienced by the electromagnetic waves in precipitation must first be removed in order to approach the splash effect. All NRCS measured in precipitation—that is, where the mean SFMR rain rate for a scan is at least $5\,\mathrm{mm\,h^{-1}}$—is corrected for attenuation. The correction is based on attenuation models: for Ku-band, the model is the Atlas $\lambda = 1.778\,\mathrm{cm}$ $10\,^{\circ}\mathrm{C}$ model [57] shown in section 4.4; for C-band the model is the Recommendation ITU-R P.838-3 model [58] at the appropriate frequency and polarization. Since both of these models are one-way predictors of K_s, which has units of $\mathrm{dB\,km^{-1}}$, the mean slant range to the surface is retained for each alongtrack cell used. After first computing the model using the rain rate bin of the sample, the mean range to the surface is multiplied to the output and is then doubled. This is then added to the fine-binned NRCS to obtain the attenuation-corrected NRCS measurements. These corrected NRCS measurements are then be averaged into wider wind speed and rain rate bins.

For analysis, rain retrievals are grouped into three categories: rain-free (SFMR rain rate $\leq 5\,\mathrm{mm\,h^{-1}}$), light rain ($5\,\mathrm{mm\,h^{-1}} <$ SFMR rain rate $< 10\,\mathrm{mm\,h^{-1}}$), and heavy rain (SFMR rain rate $\geq 10\,\mathrm{mm\,h^{-1}}$). The attenuation-corrected NRCS are partitioned after correction so the adjustment is based on the SFMR-retrieved rain rate and not these coarse partitions. The Fourier coefficients of (3.1) are estimated again using the corrected NRCS.

4.4 Analysis of Observed NRCS with Respect to Reference NRCS

In this section the effect of precipitation impact with the ocean surface on NRCS is evaluated by comparing IWRAP observations, corrected for attenuation, with GMFs developed in chapter 3 using SFMR retrievals as the ground truth. The ocean surface roughness is modified as a function of rain rate and wind speed [47]. However, the effect of ocean splash at higher wind speeds is not well understood. When observing the ocean surface through precipitation, the rain attenuates, scatters, and absorbs the electromagnetic waves twice: once before they impinge on the surface and once during the return trip to the radar. The amount of attenuation experienced by the radar can be modeled as a power law function of rain rate,

$$K_s = aR^b, \tag{4.18}$$

where R is the intervening rain rate and a and b are constants. To determine K_s in different levels of rain, four models of specific attenuation as a function of rain rate, or K_s–R models, are evaluated using the dual-frequency technique described in sections 4.2.2 and 4.2.3. Once SFMR is established as a reliable method for determining rain rate, data from the flight experiments of chapter 3 are used to evaluate IWRAP observations at C- and Ku-band for a splash effect.

4.4.1 K_s–R Models vs. SFMR Rain Rate

Here data from one flight experiment, flown on August 31, 2008 through Hurricane Gustav, is used to evaluate the performance of SFMR with respect to some K_s–R models. This flight was chosen because it contains a wide range of wind speeds and rain rates (it was a Category 3 hurricane at the time), the sensitivity of both radars is high enough to observe differences in rain rates down to $10\,\mathrm{mm\,h^{-1}}$, and the reflectivity of both radars is consistent throughout the flight. After applying the methodology

described in section 4.3.1, the dataset contains 8838 scans. 75.5 % of the scans are rain-free (less than 5 mm h^{-1} SFMR rain rate), 14.6 % of the scans are rainy (greater than 10 mm h^{-1}), and the remainder are discarded.

Figure 4.4 shows the IWRAP-measured path-averaged Ku-band attenuation ($\bar{K}_s$) data from Gustav as a function of SFMR rain rate. To obtain this plot, $\bar{K}_s$ samples are grouped into 2.5 mm h^{-1}-wide rain rate bins and averaged together, starting at 10 mm h^{-1}. The averaging is performed with the variable in units of dB km^{-1}. A least-squares fit is performed to the mean $\bar{K}_s$ values for a function of the form $\bar{K}_s = aR^b$, where R is the rain rate. This fit is shown as a solid line and closely matches the $\lambda = 1.778$ cm ($f = 16.87$ GHz) model from Atlas and Ulbrich [57]. SFMR retrievals are estimates of the mean conditions observed within its columnar beamwidth over a fixed flight time. In the next section, the Atlas $\lambda = 1.778$ cm model and SFMR rain rate will be used to correct for round-trip attenuation of the NRCS at Ku-band. Any attenuation at C-band should be small, but it is still corrected using the ITU-R P.838-3 model [58] at the frequency of the inner incidence angle channel (5.42 GHz).

4.4.2 Effect of Precipitation on NRCS

For this investigation, the wind speed and rain rate observed by the SFMR is assumed to be representative of that which is observed by all IWRAP beams at all azimuth angles. As stated in section 4.3.2, NRCS measurements are available in 5.625° azimuth bins and 2.5 km alongtrack cells. For each cell, there is an associated SFMR wind speed and rain rate. The alongtrack cells containing NRCS measurements are used to estimate the wind direction. If the direction is more than ±90° different than the direction indicated by a surface wind vector model, the NRCS-estimated direction is adjusted by 180°. The NRCS is shifted azimuthally so that upwind is at 0° and is grouped into wind speed and rain rate bins. The wind speed bins are 2.5 m s^{-1} wide and are determined according to SFMR. The rain rate bins, also determined

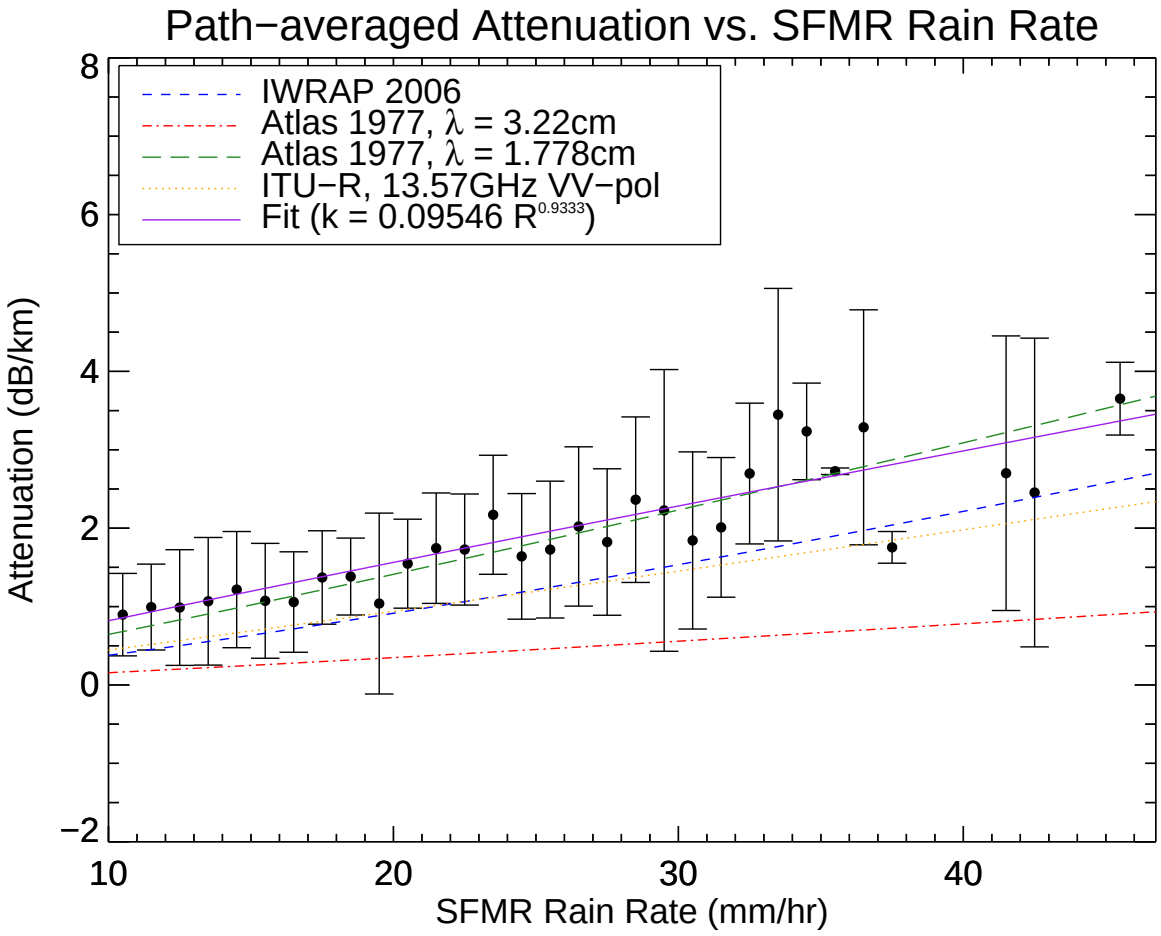

Figure 4.4. Path-averaged attenuation ($\bar{K}_s$) at Ku-band vs. SFMR rain rate for the flight experiment through Hurricane Gustav on August 31, 2008. Each rain rate bin is $1\,\mathrm{mm\,h^{-1}}$ wide. The error bars show one standard deviation of the data on either side of the mean. Several GMFs are shown alongside the fit to the data, which is shown as a purple line. The model derived from IWRAP and SFMR data in 2006 is shown as a dashed line. Two models at wavelengths near Ku-band from Atlas and Ulbrich [57] are shown as long-dashed and dash-dotted lines. The ITU-R P.838-3 model [58] at Ku-band is shown as a dotted line.

by SFMR, separate precipitation into categories: rain-free, light rain, and heavy rain. In each wind speed and rain rate bin, the NRCS measurements are averaged within azimuth bins and a curve is fit to the data in the form of (3.1). From this curve, the coefficients of (3.1) are estimated.

Figure 4.4 points out some potential ambiguity in the K_s–R model used to estimate K_s, which is used to correct the NRCS for attenuation. Neglecting the model at $\lambda = 3.22\,\mathrm{cm}$ ($f = 9.32\,\mathrm{GHz}$) due to frequency, the models shown in figure 4.4 all have similar shapes. The specific attenuation models could plausibly be off by a small amount in the vertical direction. This analysis allows for this by assuming that there is no splash effect in the light rain scenario for wind speeds above $15\,\mathrm{m\,s^{-1}}$. For each flight experiment season, a fit to the A_0 estimates in light rain is performed in the same way as it was for the rain-free data in chapter 3. The data for each season are adjusted such that the A_0 fit for that season matches the new IWRAP GMF in the $25.0\,\mathrm{m\,s^{-1}}$ to $27.5\,\mathrm{m\,s^{-1}}$ bin. Since this is applied to each season, an exact match of the fit to the aggregated data in this bin is not necessarily expected. This adjustment, which is independent of wind speed and rain rate, is then applied to all rainy data after correcting for attenuation. Figure 4.5 shows the A_0 data both in light rain and in rain-free conditions before correcting for attenuation and K_s–R model inaccuracies. Figure 4.6 shows the data after both corrections have been applied. Combined, this rain-rate-independent adjustment and the correction for K_s can be considered the whole attenuation correction. At both C- and Ku-band the data from light rain is nearly on top of the rain-free data, indicating that the assumption of no splash effect at these rain rates is reasonable.

4.4.2.1 Effect of Precipitation on Fourier Coefficients

Figure 4.7 shows the mean NRCS, or A_0 term of the NRCS GMF, for the C- and Ku-band VV- and HH-polarization 22° incidence angles as a function of wind speed.

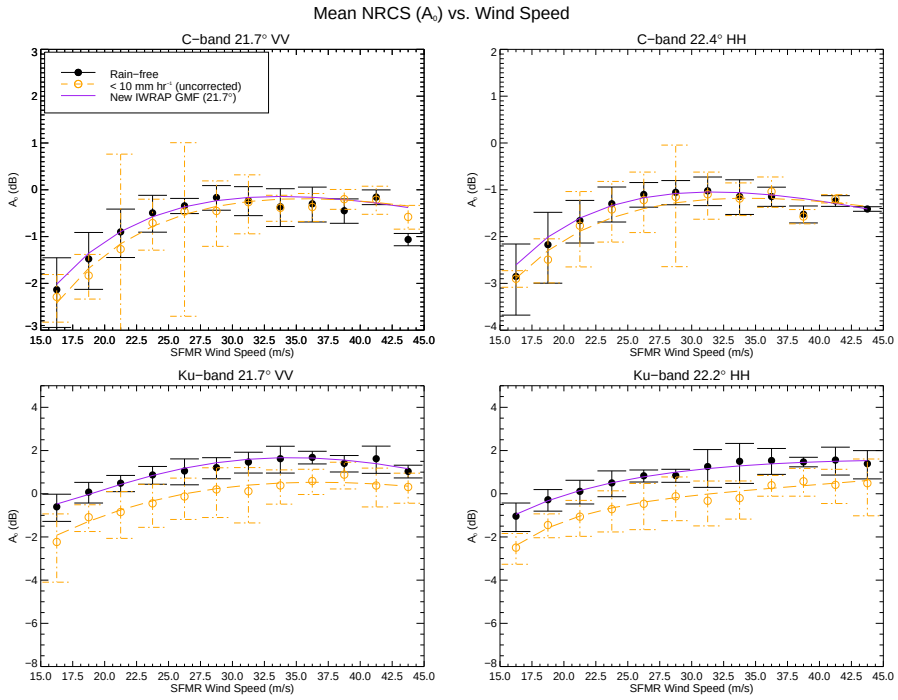

Figure 4.5. Mean NRCS vs. wind speed (A_0 term), uncorrected, for 21.7° and 22.4° incidence at C-band (upper panels) and 21.7° and 22.2° incidence at Ku-band (lower panels). VV-polarization responses to wind speed are in the left panels and those for HH-polarization are in the right panels. Rain-free A_0 data are shown as filled circles with the standard deviation of A_0 estimates from all rain-free wind vector cells shown as the error bars. A_0 data from light rain are shown as empty circles with a fit to the data shown as a dashed line. The new IWRAP GMF from chapter 3 is shown as a solid line.

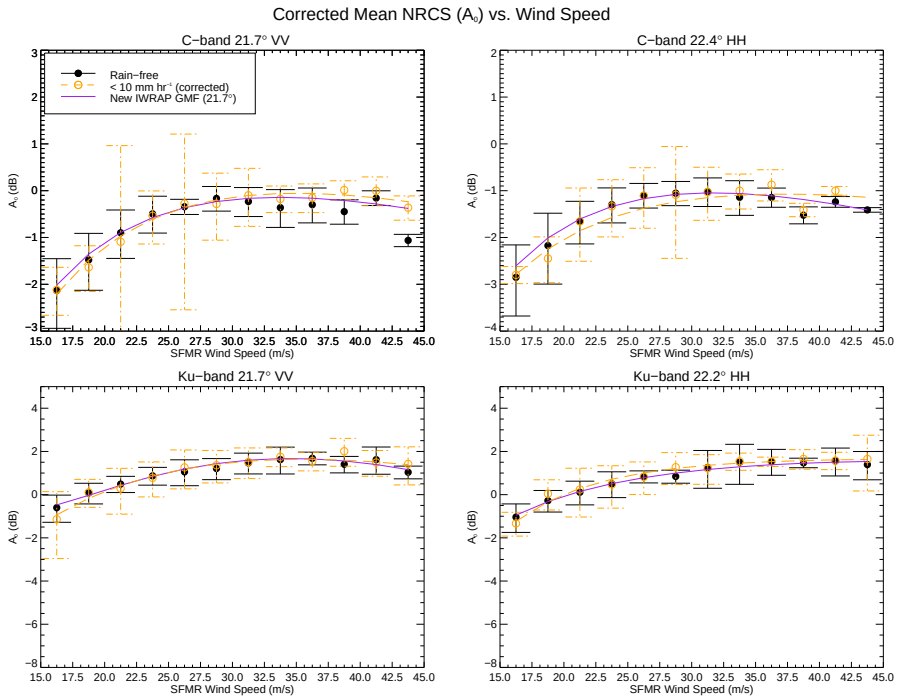

Figure 4.6. Mean NRCS vs. wind speed (A_0 term), corrected for attenuation, for 21.7° and 22.4° incidence at C-band (upper panels) and 21.7° and 22.2° incidence at Ku-band (lower panels). VV-polarization responses to wind speed are in the left panels and those for HH-polarization are in the right panels. Rain-free A_0 data are shown as filled circles with the standard deviation of A_0 estimates from all rain-free wind vector cells shown as the error bars. A_0 data from light rain are shown as empty circles with a fit to the data shown as a dashed line. The new IWRAP GMF from chapter 3 is shown as a solid line.

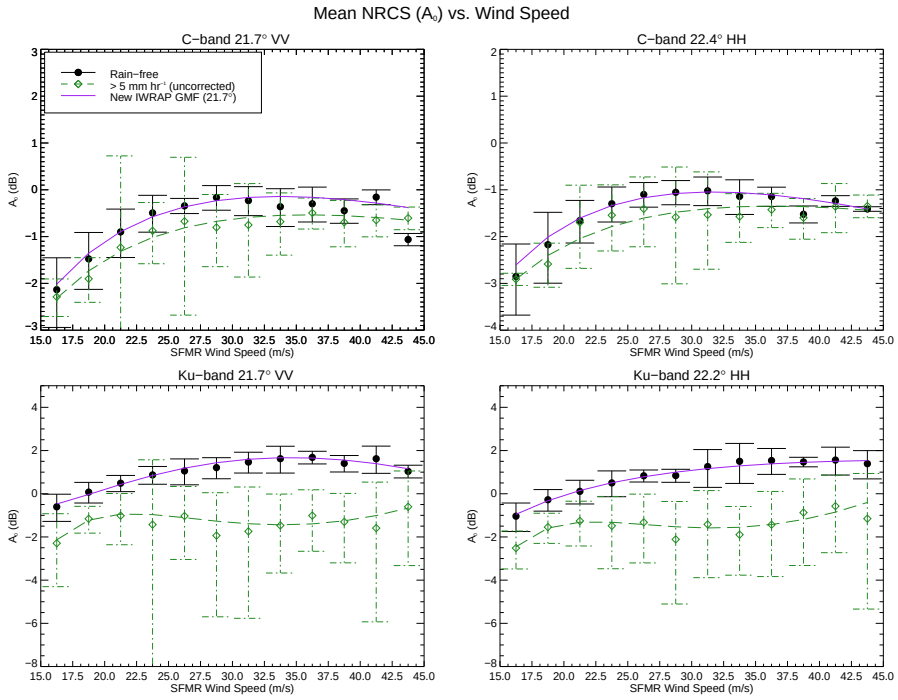

Figure 4.7. Mean NRCS vs. wind speed (A_0 term), uncorrected, for 21.7° and 22.4° incidence at C-band (upper panels) and 21.7° and 22.2° incidence at Ku-band (lower panels). VV-polarization responses to wind speed are in the left panels and those for HH-polarization are in the right panels. Rain-free A_0 data are shown as filled circles with the standard deviation of A_0 estimates from all rain-free wind vector cells shown as the error bars. A_0 data from all rainy cells are shown as empty diamonds with a fit to the data shown as a dashed line. The new IWRAP GMF from chapter 3 is shown as a solid line.

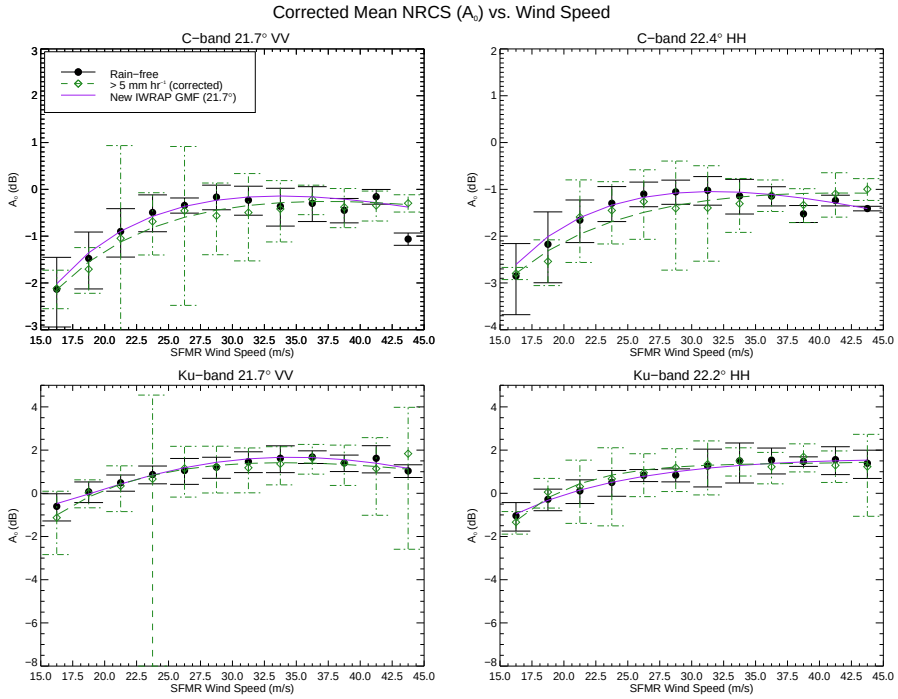

Figure 4.8. Mean NRCS vs. wind speed (A_0 term), corrected for attenuation, for 21.7° and 22.4° incidence at C-band (upper panels) and 21.7° and 22.2° incidence at Ku-band (lower panels). VV-polarization responses to wind speed are in the left panels and those for HH-polarization are in the right panels. Rain-free A_0 data are shown as filled circles with the standard deviation of A_0 estimates from all rain-free wind vector cells shown as the error bars. A_0 data from all rainy cells are shown as empty diamonds with a fit to the data shown as a dashed line. The new IWRAP GMF from chapter 3 is shown as a solid line.

Along with the rain-free data, all rainy data (SFMR rain rate at least $5\,\mathrm{mm\,h^{-1}}$) are also shown. The new IWRAP GMF developed in chapter 3 is shown as a solid line. The mean of the fits to the azimuthally-varying NRCS in each wind speed bin are shown as filled circles (for the rain-free cells) or empty diamonds (for the rainy cells). The error bars are the standard deviation of A_0 estimates from all alongtrack cells. The general shape of the C-band A_0 curves with respect to wind speed is about the same in rainy conditions as well as rain-free, but there is some modification of the signal occurring. As expected, the mean Ku-band NRCS is severely affected by precipitation in both scatter about the mean and response to wind speed.

Figure 4.8 shows the mean NRCS as a function of wind speed after correcting for attenuation. There is little change in the C-band plots. The rainy data are shifted up slightly, but not by a significant amount. At Ku-band, the flattened NRCS observed in figure 4.8 is removed. Additionally, the means of the corrected A_0 are now nearly on top of the rain-free data and the fit is almost the same as the new IWRAP GMF.

Figure 4.9 shows the a_1 term of the NRCS, after the attenuation correction has been applied, as a function of wind speed. In order to obtain the corrected a_1 term, attenuation correction is applied to the azimuth-binned NRCS before the fit is performed. As expected, there is no noticeable change in a_1 after correcting for attenuation, except that the variance becomes smaller. As a result, the uncorrected data is not shown.

Section 3.4.2 explains that A_1 controls the upwind/downwind anisotropy of the NRCS azimuthal signature; the difference between upwind and downwind peaks in linear units is $2A_1 = A_0 \cdot 2a_1$. The normalized a_1 is the amplitude difference between the two peaks with the change in A_0 removed. In other words, it is the difference between NRCS observed upwind and NRCS observed downwind without the amplitude change caused by A_0. Normalization is most necessary when analyzing trends with wind speed, since the additional effect of A_0 will mask the a_1 signal. Figure 4.9 indicates that the upwind/downwind difference may still change with wind speed, but it is independent of a_1 and can be completely represented by A_0.

Figure 4.10 shows the a_2 term of the NRCS, after the attenuation correction has been applied, as a function of wind speed. In order to obtain the corrected a_2 term, attenuation correction is applied to the azimuth-binned NRCS before the fit is performed. In general all curves follow the same trend, but the magnitude of a_2 is smaller when in precipitation.

A decrease in the ability of the scatterometer to retrieve direction is expected. Portabella *et al.* [3], among others, point out that for low winds in precipitation,

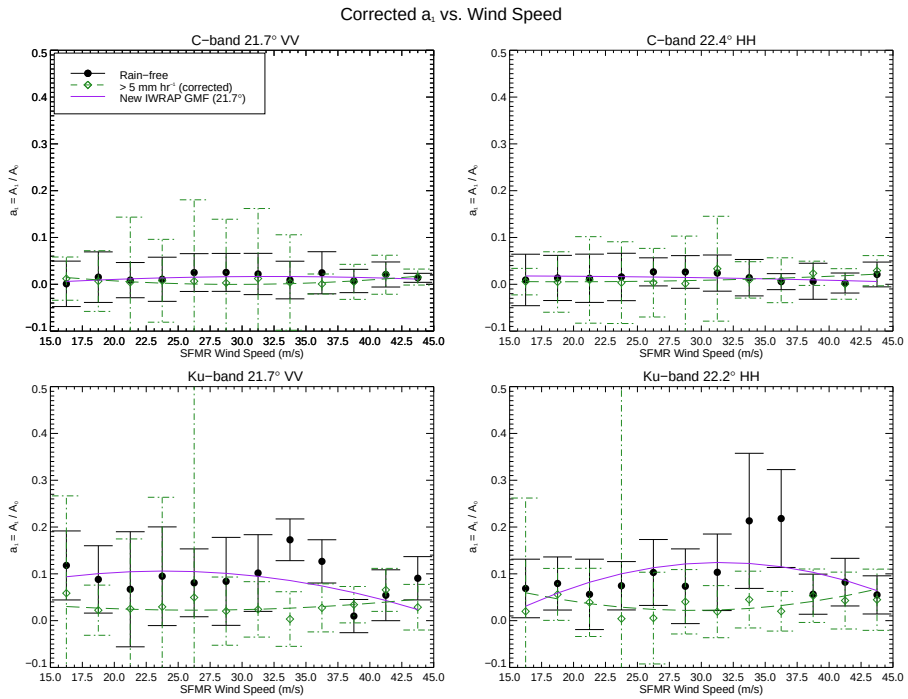

Figure 4.9. Normalized NRCS A_1 term (a_1) vs. wind speed, corrected for attenuation, for 21.7° and 22.4° incidence at C-band (upper panels) and 21.7° and 22.2° incidence at Ku-band (lower panels). VV-polarization responses to wind speed are in the left panels and those for HH-polarization are in the right panels. Rain-free a_1 data are shown as filled circles with the standard deviation of a_1 estimates from all rain-free wind vector cells shown as the error bars. a_1 data from all rainy cells are shown as empty diamonds with a fit to the data shown as a dashed line. The new IWRAP GMF from chapter 3 is shown as a solid line.

the wind direction retrieval from ASCAT data tends to produce direction estimates perpendicular to the actual wind direction. While the azimuthal signature does not become this corrupted at the lower wind speeds observed here, there is additional noise in the azimuthal signature. This could be sufficient to introduce more ambiguities in the direction retrieval.

Since a_1 is not affected by precipitation, a splash effect appears to manifest itself in the a_2 term. Figure 4.11, which shows the difference between upwind and crosswind NRCS, makes clearer how precipitation impacts wind direction retrievals. This difference is subdued at all wind speeds in precipitation. When the difference between upwind and crosswind becomes smaller, the overall modulation of NRCS with azimuth is diminished. Using measurements from ERS scatterometer, Nie and Long [59] show that the backscatter tends to become more isotropic in precipitation. This is supported at high winds by the observed decrease in a_2 and the upwind/crosswind signature.

Section 3.4.2 also describes the effect of A_2 and a_2 on the overall NRCS azimuthal signature. a_2 can be combined with a_1 to describe the normalized upwind/crosswind asymmetry. However, when a_1 is relatively constant over the wind speeds observed, as it is at these incidence angles, the a_2 behavior will dominate this effect. There is some decrease in the amplitude of a_2 in precipitation, though the general shape remains the same. As with a_1, since this term is normalized to A_0, the amplitude is theoretically independent of the effect of precipitation on the mean NRCS. Based on figure 4.10, there should be some flattening of the NRCS in precipitation; the a_2 behavior shows that the upwind peak and crosswind trough are closer to each other than in the rain-free conditions. This can be observed more clearly in section 4.4.2.2.

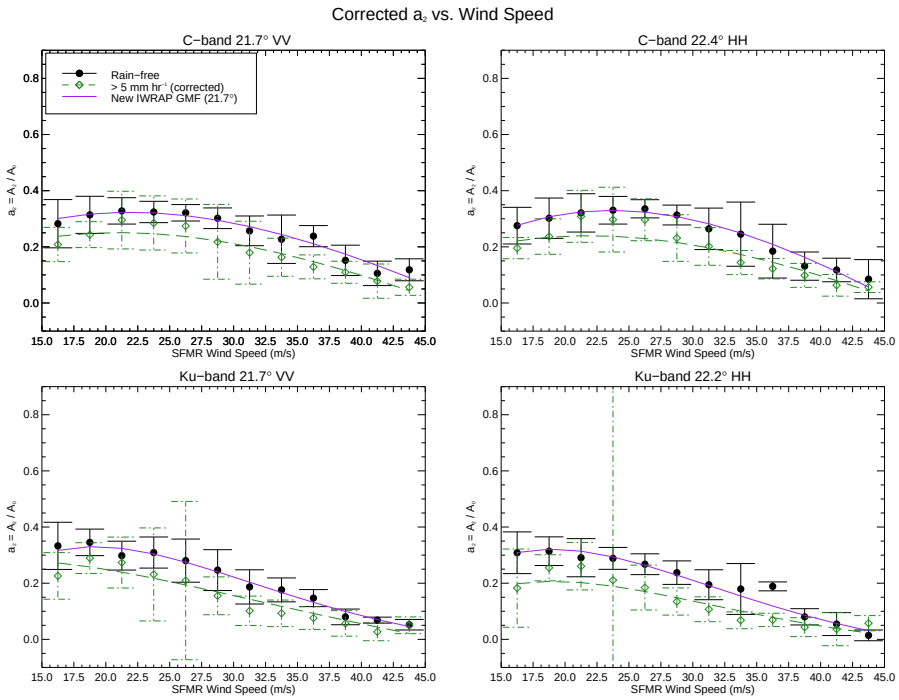

Figure 4.10. Normalized NRCS A_2 term (a_2) vs. wind speed, corrected for attenuation, for 21.7° and 22.4° incidence at C-band (upper panels) and 21.7° and 22.2° incidence at Ku-band (lower panels). VV-polarization responses to wind speed are in the left panels and those for HH-polarization are in the right panels. Rain-free a_2 data are shown as filled circles with the standard deviation of a_2 estimates from all rain-free wind vector cells shown as the error bars. a_2 data from all rainy cells are shown as empty diamonds with a fit to the data shown as a dashed line. The new IWRAP GMF from chapter 3 is shown as a solid line.

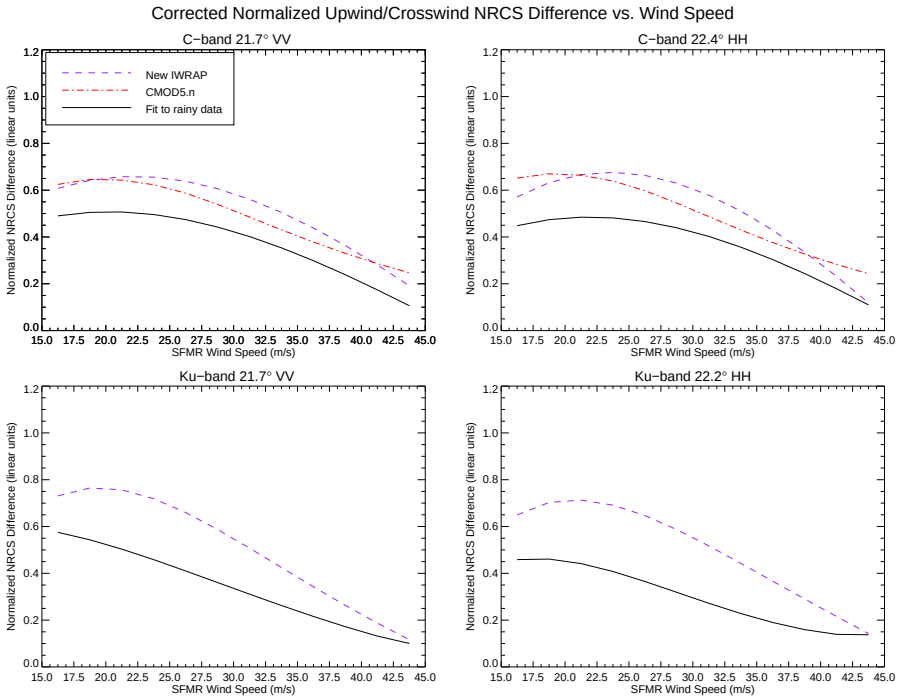

Figure 4.11. Upwind NRCS less crosswind NRCS vs. wind speed, corrected for attenuation, for 21.7° and 22.4° incidence at C-band (upper panels) and 21.7° and 22.2° incidence at Ku-band (lower panels). VV-polarization responses to wind speed are in the left panels and those for HH-polarization are in the right panels. NRCS is first normalized by A_0. Rain-free a_2 data are shown as filled circles with the standard deviation of a_2 estimates from all rain-free wind vector cells shown as the error bars. The normalized upwind/crosswind difference from the fits to the rainy data is shown as a solid line. The new IWRAP GMF from chapter 3 is shown as a dashed line. At C-band, the CMOD5.n GMF is also shown; at Ku-band, there are no GMFs near the incidence angles analyzed.

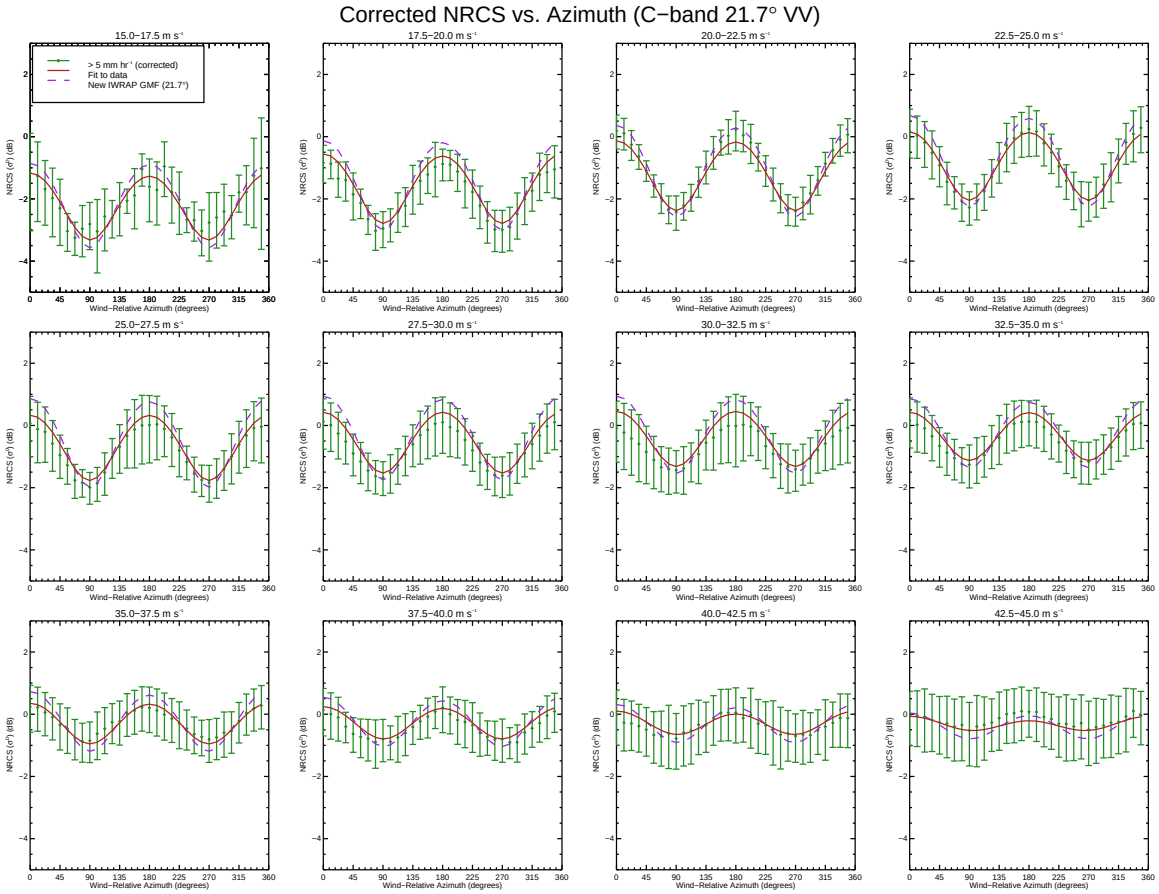

Figure 4.12. C-band NRCS vs. azimuth for VV-polarization at 21.7° incidence in precipitation for wind speed bins from $15\,\mathrm{m\,s^{-1}}$ to $45\,\mathrm{m\,s^{-1}}$, corrected for attenuation. The fit to the parameters are used to compute a model function, which is shown as solid lines. The new IWRAP GMF from chapter 3 is shown as dashed lines.

4.4.2.2 Azimuthal Behavior

Figures 4.12 to 4.15 show the response of attenuation-corrected NRCS in precipitation at different wind speeds as a function of wind-relative azimuth. The data points are shown as empty circles with the standard deviations as error bars. The fit to the A_0, a_1, and a_2 parameters of figures 4.8 to 4.10 are used to create a model; this is shown as solid lines. The new IWRAP GMF developed in chapter 3 is shown as dashed lines.

Compared to the new IWRAP GMF, the C-band NRCS measured in precipitation generally has more damped upwind and downwind peaks at both polarizations. There

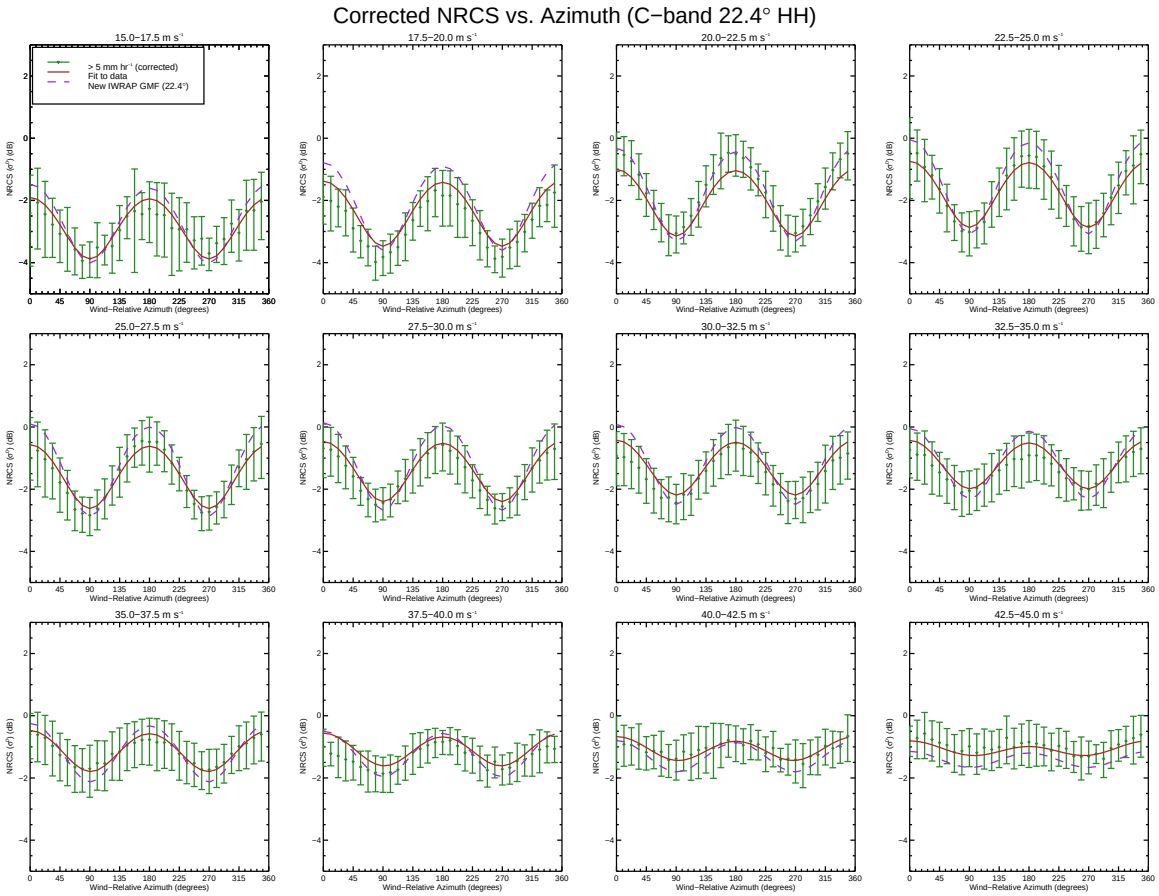

Figure 4.13. C-band NRCS vs. azimuth for HH-polarization at 22.4° incidence in precipitation for wind speed bins from $15\,\mathrm{m\,s^{-1}}$ to $45\,\mathrm{m\,s^{-1}}$, corrected for attenuation. The fit to the parameters are used to compute a model function, which is shown as solid lines. The new IWRAP GMF from chapter 3 is shown as dashed lines.

are a few wind speed bins, notably the $22.5\,\mathrm{m\,s^{-1}}$ to $25.0\,\mathrm{m\,s^{-1}}$ bin, in which the mean crosswind peak exceeds the upwind peak. This indicates a possible decrease in a_1 below 0, but, as can also be observed in figure 4.9, the model fit does not reflect this. This is due to one of the assumptions made here about the geophysical phenomena that a_1 is non-negative at these wind speeds. This was necessary due to the lack of reliable external surface wind direction information at the 2.5 km resolution in hurricanes. In rain-free conditions it is expected that the peak NRCS is in the upwind direction, but this may not be a valid assumption in rainy conditions. This effect may also be due to the amount of noise in the measurements, which seems more likely since it is significantly more than the rain-free measurements in all wind speed bins.

At Ku-band, a possible negative a_1 can also be observed in some wind speed bins (particularly the $30.0\,\mathrm{m\,s^{-1}}$ to $32.5\,\mathrm{m\,s^{-1}}$ bin at VV-polarization and the $27.5\,\mathrm{m\,s^{-1}}$ to $30.0\,\mathrm{m\,s^{-1}}$ bin at HH-polarization).

At Ku-band, the directional signature of the NRCS is dimished almost to the point of nonexistence by $37.5\,\mathrm{m\,s^{-1}}$ to $40.0\,\mathrm{m\,s^{-1}}$. At C-band, a slight modulation is maintained up to at least $42.5\,\mathrm{m\,s^{-1}}$ at both polarizations. This is a reflection of the damping of the a_2 parameter in precipitation. With a_1 remaining the same in precipitation, the change in upwind/crosswind difference is influenced only by a_2. The compressing of the NRCS extremes is apparent in precipitation.

4.5 Conclusion

The effect of precipitation impact on sea-surface NRCS at wind speeds from $15\,\mathrm{m\,s^{-1}}$ to $45\,\mathrm{m\,s^{-1}}$ was analyzed. One IWRAP flight experiment through Hurricane Gustav on August 31, 2008 was used to evaluate the ability of SFMR to retrieve rain rate. Wind speeds from $27.5\,\mathrm{m\,s^{-1}}$ to $50\,\mathrm{m\,s^{-1}}$ both with and without rain were observed by the C-band radar at HH-polarization and the Ku-band radar at VV-polarization. Since the C-band and Ku-band radars are not necessarily synchronized,

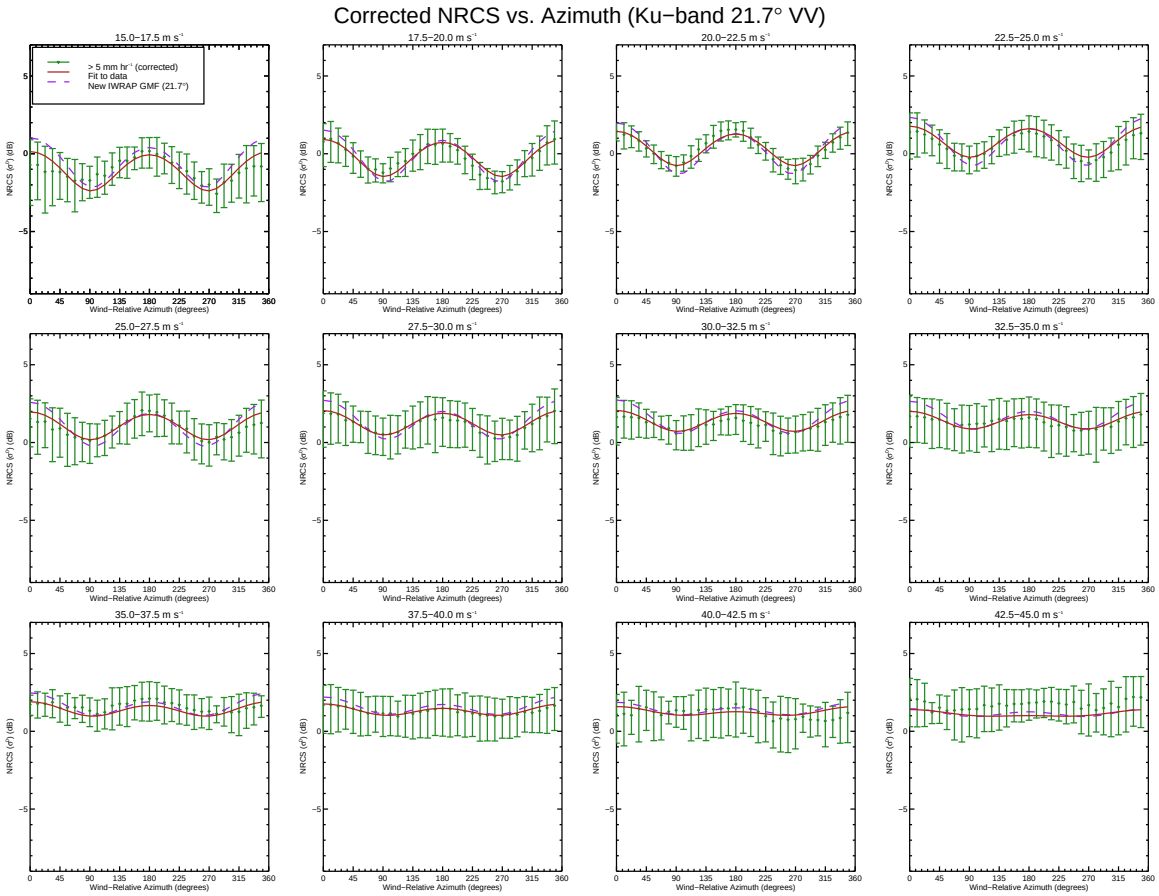

Figure 4.14. Ku-band NRCS vs. azimuth for VV-polarization at 21.7° incidence in precipitation for wind speed bins from $15\,\mathrm{m\,s^{-1}}$ to $45\,\mathrm{m\,s^{-1}}$, corrected for attenuation. The fit to the parameters are used to compute a model function, which is shown as solid lines. The new IWRAP GMF from chapter 3 is shown as dashed lines.

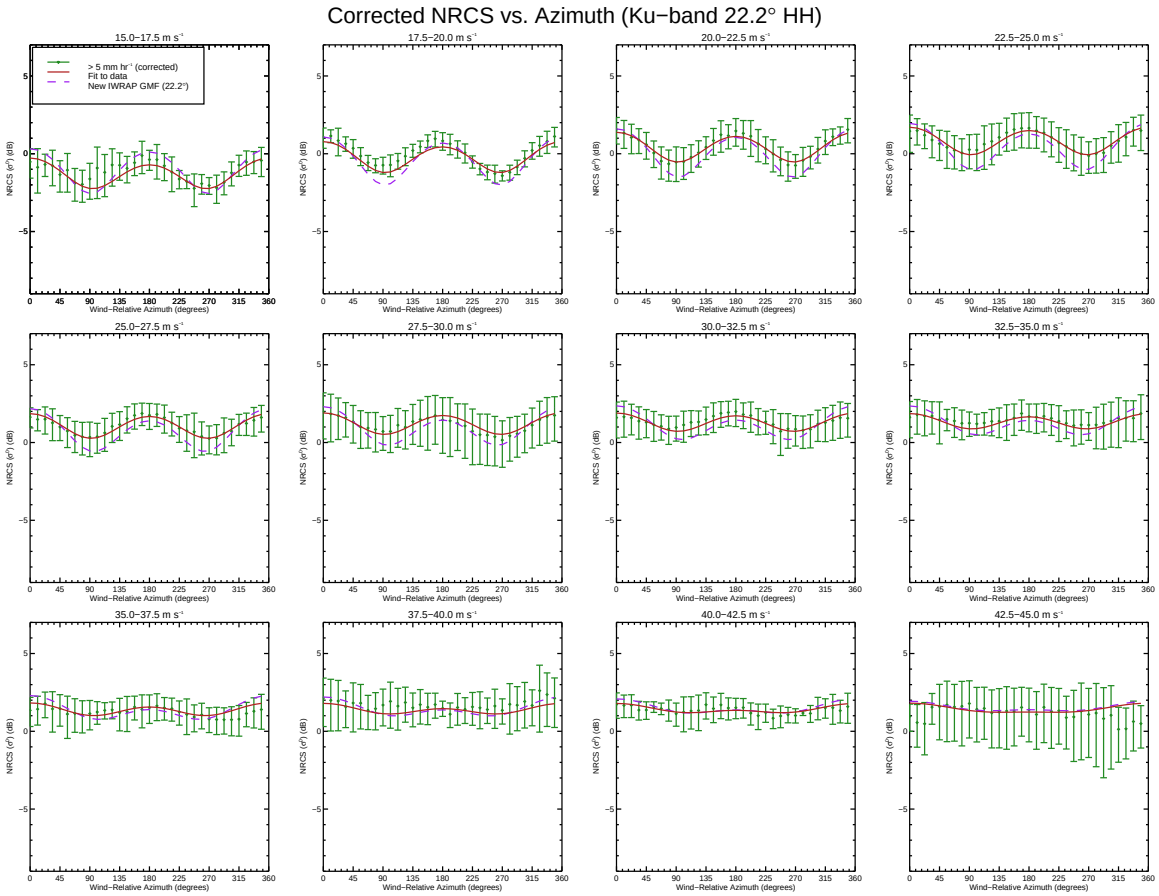

Figure 4.15. Ku-band NRCS vs. azimuth for HH-polarization at 22.2° incidence in precipitation for wind speed bins from 15 m s^{-1} to 45 m s^{-1}, corrected for attenuation. The fit to the parameters are used to compute a model function, which is shown as solid lines. The new IWRAP GMF from chapter 3 is shown as dashed lines.

360° scans of each were collocated. Through the observation of similar volumes, the attenuation experienced by the Ku-band radar between the aircraft and ocean surface as a function of SFMR rain rate was estimated. It was determined that SFMR rain rate retrievals are accurate above $5\,\mathrm{mm\,h^{-1}}$ to predict specific attenuation.

SFMR rain rate retrievals were used with specific attenuation models at C- and Ku-band to remove attenuation and scattering due to rain. NRCS data from the IWRAP radars at incidence angles near 22° and both VV- and HH-polarizations were collected from between the 2011 and the 2014 hurricane seasons. After correcting NRCS observed in rain for attenuation, there remained some offsets in the measured mean NRCS (A_0). It was assumed that the effect of splash at wind speeds above $15\,\mathrm{m\,s^{-1}}$ was negligible at rain rates below $10\,\mathrm{m\,s^{-1}}$, so an adjustment was calculated using this data. This adjustment is independent of wind speed and rain rate and was applied to all NRCS data at each frequency and polarization.

In doing this, the rain attenuation and scattering effects from NRCS measurements were removed, leaving only the effects of precipitation impact in excess of the surface wind effect. No measurable change was observed in the mean NRCS at either frequency or polarization. There is some additional scatter around the means not evident in the rain-free measurements, which may indicate some additional geophysical noise.

There was also no noticeable effect on the a_1 term of the scatterometer GMF. It remains almost flat across the range of wind speeds, indicating that the upwind and crosswind peaks are almost equal and the difference is independent of wind speed. The a_2 term showed a fairly uniform dampening as a function of wind speed. This means that in precipitation, the NRCS have a more vertically compressed profile in azimuth. This result is also evident when explicitly calculating the upwind/downwind difference, which is largely driven by a_2.

The NRCS azimuthal behavior clarified the effects shown in each parameter. The modulation in azimuth flattened sooner than when free of precipitation. At C-band, there is still a visible signature up to the $45\,\mathrm{m\,s^{-1}}$, but the Ku-band signal is effectively flat above $35\,\mathrm{m\,s^{-1}}$ to $40\,\mathrm{m\,s^{-1}}$.

There appears to be no splash effect on the mean NRCS at 22° incidence at either polarization. The directional signature does suffer slightly in precipitation, compressing the extremes of the curve. Since these are low incidence angles, the amplitude of the NRCS may overcome any splash effects here. As saturation is observed from $30\,\mathrm{m\,s^{-1}}$ to $40\,\mathrm{m\,s^{-1}}$ for both C- and Ku-band, the ocean surface roughness is nearing a maximum at these wind speeds. It is anticipated that there are more significant splash effects at larger incidence angles, but these results suggest it is only in the azimuthal response or at the lower end of the wind speed range.

CHAPTER 5

POLARIZATION RATIO EFFECTS OF HIGH WIND SPEEDS AT C-BAND

5.1 Introduction

Satellite-borne observations of sea surface backscatter are routinely used to estimate winds. Currently, the Advanced Scatterometer (ASCAT) aboard the European MetOp-1 satellite measures sea surface winds using C-band vertical polarization. The Canadian RADARSAT-2 SAR instrument also operates at C-band measuring both V- and H-polarizations. Though primarily designed for high-resolution imaging, there have been a number of recent efforts to infer wind speed and direction from C-band RADARSAT SAR imagery [60], [61], most recently on the potential utility of cross-polarized measurements [6], [43] (i.e., transmit and receive polarizations are orthogonal). Use of C-band is also being explored in designs for a future US scatterometer to replace the defunct Ku-band QuikSCAT instrument. As C-band is less prone to attenuation in precipitation, it is more robust in the presence of rain than is Ku-band. However, since Ku-band offers finer spatial resolution for a given antenna size, future scatterometry missions are expected to incorporate both frequencies.

During January and February 2011 a series of flight experiments were conducted over the North Atlantic in extratropical storms to obtain observations of the sea surface under strong wind forcing. In particular, it was desired to extend rain-free, high-wind normalized radar cross-section (NRCS), or σ^0, observations at VV- and HH-polarizations to incidence angles near and beyond 60°. In this chapter the radar instrumentation, flight experiments, and the results of several circle flights are de-

Table 5.1. C-band Radar Parameters

Parameter	Chan. 1	Chan. 2
Frequency (GHz)	5.025	5.2
Nom. Incidence Angle	46.4°(H), 46.7°(V)	34.0°(H), 36.0°(V)
Pulse Rate (kHz)	15	15
Pulse width (μs)	10 (chirp)	0.8 (pulse)
Antenna Gain (dB)	21.4(H), 24.9(V)	23.9(H), 25.1(V)
Azimuthal Beamwidth	10.1°(H), 9.9°(V)	13.5°(H), 12.2°(V)
Scan Rate (rpm)	60	60

scribed, from which the incidence angle and azimuthal dependence at one C-band frequency were investigated. A condensed version of this chapter was published as Sapp *et al.* [62].

5.2 Experiment Description

The Imaging Wind and Rain Airborne Profiler (IWRAP), initially described in Fernandez *et al.* [18], is a dual-frequency conically-scanning Doppler radar developed by MIRSL at UMass that is routinely installed on the NOAA WP-3D research aircraft. IWRAP is primarily designed to study the signature of the ocean surface under wind forcing. Two radars (one C-band and one Ku-band) scan at two incidence angles each, typically between 20° and 50°. Each radar is capable of implementing up to four simultaneous beams, however, two simultaneous beams per radar is the normal mode of operation. Both VV- and HH-polarizations are available and are selected based upon mission requirements. The radar beam widths vary depending upon the selected incidence angle owing to properties of the frequency-scanning antenna, but are typically in the neighborhood of 10°. For the Winter 2011 mission, IWRAP was configured to measure VV- and HH-polarizations by toggling rapidly between them during each azimuthal scan. Table 5.1 summarizes the C-band radar parameters during data collection.

Table 5.2. Summary of the Winter 2011 Flight Experiment

Date	Times (UTC)	Circles Executed	Wind Speeds ($\mathrm{m\,s^{-1}}$)
20110123	1600–2000	3	19–24
20110124	1600–2000	8	21–27
20110130	1700–2100	5	18–24
20110201	1600–1900	6	25–36
20110207	1600–1900	6	23–31

The IWRAP geophysical model function (GMF) was developed for several fixed incidence angles between 30° and 50° at VV- and HH-polarizations [30]. The goal of the Winter 2011 experiment was to obtain rain-free sea-surface NRCS observations over a continuous range of incidence angles between 20° and 60° at both VV- and HH-polarizations. The most expedient means to accomplish this is to fly the aircraft in a circular pattern at a constant roll angle. In this way, the conically scanning beam impinging on the sea surface traces out an ellipse with incidence angles varying with the azimuthal scan angle. The range of incidence angles encountered is given by the nominal (level flight) incidence angle plus or minus the roll angle. Since the incidence angle varies with the azimuthal angle, and since the NRCS also varies with azimuth angle (relative to the wind direction), a circle pattern ensures that all incidence angles are observed from all directions. The instantaneous incidence angle given this maneuver is derived in section 5.3.

Surface wind speeds were measured simultaneously with the Stepped Frequency Microwave Radiometer (SFMR) [28] operated by AOC aboard the WP-3D aircraft. Since the SFMR is a nadir-looking instrument, the mean wind speed from the retrievals before and after a roll is used as the wind speed during a roll. Several missions were flown out of Halifax, NS during January–February 2011; table 5.2 contains a summary of the Winter 2011 flight experiment.

5.3 Data Processing Methodology

During the Winter 2011 experiment, the IWRAP radar alternated between polarizations by transmitting a sequence of 126 pulses in each polarization. Raw I- and Q-channel samples were collected and recorded. In post-processing, some of these data were subject to pulse compression; Doppler spectrum moments were then accumulated over each 126-pulse block using pulse-pair methods [54]. The resulting profiles of backscatter and Doppler velocity are available at a rate of approximately 60 Hz per polarization. Given the azimuthal scan rate of the antenna, there are approximately 60 radials in each 360° scan of the antenna (one per second). The resulting profiles are then merged with navigation parameters (pitch, roll, drift, etc. available at a 40 Hz rate) and simultaneous surface wind speed estimates from the SFMR (available at a 1 Hz rate).

Once merged, the data are sorted by incidence and azimuth angle. The incidence angle is derived from navigation parameters and antenna azimuth information using methods described in Lee *et al.* [63]. This is checked for consistency against a separate radar estimate from the arc-cosine of the ratio of the slant range to the surface echo and the aircraft altitude. Similarly, antenna azimuth is verified by a check against the observed Doppler shift from the sea surface after appropriate transformations for pitch, roll, and drift.

Although a range of incidence angles may be observed during the circle patterns, there is a small source of error due to polarization mixing. That is, given the finite roll angle, the polarization incident upon the sea surface is only truly the polarization transmitted and received at the extreme incidence angles (when the antenna is scanning to the side of the aircraft). Polarization mixing is largest when the antenna scans forward or aft of the aircraft, at which point the rotation of the polarizations is equal to the aircraft roll angle, and the incidence angle is equal to the nominal (level-flight)

value. The instantaneous polarization rotation about the antenna boresight axis, γ, is derived here.

Following Lee *et al.* [63], the aircraft-relative coordinate system is used with $\hat{x}_a$ pointing over the right wing, $\hat{y}_a$ toward the nose, and $\hat{z}_a$ upward through the fuselage. The radar antenna scans conically below the aircraft, and the unit vector in the propagation direction is

$$\begin{aligned} \hat{k} =& \hat{x}_a \sin\theta_a \sin\phi_a && (5.1)\\ &+ \hat{y}_a \sin\theta_a \cos\phi_a && (5.2)\\ &+ \hat{z}_a \cos\theta_a && (5.3) \end{aligned}$$

where θ_a is the zenith angle measured from the positive z_a-axis and ϕ_a is the azimuth angle measured clockwise from the y_a-axis (the aircraft heading). This is converted to a level, track-relative coordinate system by successive rotations through the aircraft roll, pitch, and drift angles. For simplicity zero pitch and zero drift angle is assumed. After rotation through a roll angle, R, $\hat{k}$ becomes

$$\begin{aligned} \hat{k} =& \hat{x} \sin\theta_a \sin\phi_a \cos R + \cos\theta_a \sin R \\ &+ \hat{y} \sin\theta_a \cos\phi_a \\ &+ \hat{z} \left(-\sin\theta_a \sin\phi_a \sin R + \cos\theta_a \cos R\right) \end{aligned} \qquad (5.4)$$

where the $\hat{x}$, $\hat{y}$, and $\hat{z}$ unit vectors now indicate a level, Earth-relative coordinate system. The zenith angle of the radar beam on the sea surface is given by $\cos\theta' = \hat{z}\cdot\hat{k}$, or

$$\theta' = \cos^{-1}(-\sin\theta_a \sin\phi_a \sin R + \cos\theta_a \cos R), \qquad (5.5)$$

which is the supplement of the incidence angle θ.

The unit vector parallel to the H'-polarization in aircraft coordinates is the $\hat{\phi}_a$ unit vector given by

$$\hat{\phi}_a = \hat{x}_a \cos\phi_a - \hat{y}_a \sin\phi_a \tag{5.6}$$

which when subjected to a roll angle R is expressed in level coordinates as

$$\hat{\phi} = \hat{x} \cos\phi_a \cos R - \hat{y} \sin\phi_a - \hat{z} \cos\phi_a \sin R. \tag{5.7}$$

The rotation angle of this vector out of the horizontal is given by

$$\tan\gamma = \frac{\phi_z}{\sqrt{\phi_x^2 + \phi_y^2}} = \frac{-\cos\phi_a \sin R}{\sqrt{\cos^2\phi_a \cos^2 R + \sin^2\phi_a}}. \tag{5.8}$$

Figure 5.1 illustrates this rotation at one antenna azimuth (60°). Except for large roll angles (greater than 30°), this is very well approximated by

$$\gamma \approx -R\cos\phi_a, \tag{5.9}$$

where R is the roll angle and ϕ_a is the azimuth angle measured clockwise from the aircraft heading.

To obtain the relationship between the observed (rotated) NRCS values and the desired sea-surface NRCS values, the appropriate rotations are applied to each affected part of the NRCS equation. The transmit power sampled by the radar's calibration loop, P_t, is actually representative of the transmit power in the polarization-rotated coordinated system. In order to derive the remainder of the relationship, a measurement of σ^0_{HH} is considered here.

The transmitted power, $P_{t,H'}$, is related to the transmitted power in the $\hat{V}$ and $\hat{H}$ directions by

$$\begin{aligned} P_{t,H} &= P_{t,H'} \cos\gamma \\ P_{t,V} &= P_{t,H'} \sin\gamma. \end{aligned} \tag{5.10}$$

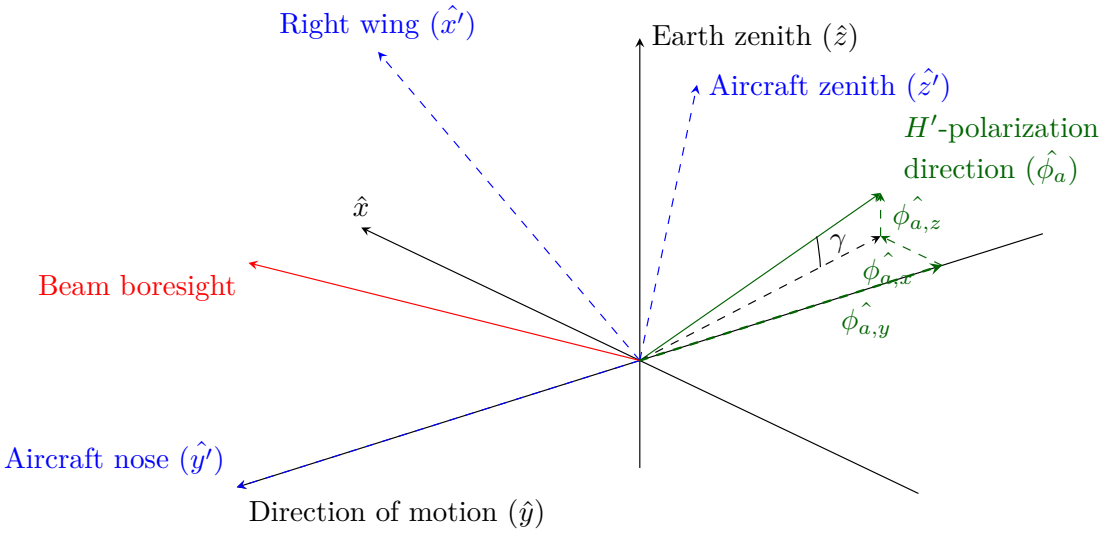

Figure 5.1. Diagram illustrating the rotation angle of the vector parallel to the H'-polarized electric field, γ, from horizontal. The aircraft is rolling at a $-20°$ angle and $0°$ pitch is assumed. The aircraft-relative unit vectors ($\hat{x'}$, $\hat{y'}$, $\hat{z'}$) are shown as dark blue dashed lines. The aircraft-relative azimuth (ϕ_a) for an incidence angle of $48°$, shown as a red solid line, is $60°$. This vector is perpendicular to the $\hat{\phi_a}$ vector.

The total transmitted power is the vector sum of the power transmitted in each polarization. The power scattered back to the antenna from the sea surface can be determined by using the NRCS:

$$\begin{aligned} P_{s,H} &= C_H\, P_{t,H}\, \sigma^0_{HH} + C_H\, P_{t,V}\, \sigma^0_{HV} \\ &= C_H\, P_{t,H'}\, \sigma^0_{HH} \cos\gamma + C_H\, P_{t,H'}\, \sigma^0_{HV} \sin\gamma \\ P_{s,V} &= C_H\, P_{t,V}\, \sigma^0_{VV} + C_H\, P_{t,H}\, \sigma^0_{VH} \\ &= C_H\, P_{t,H'}\, \sigma^0_{VV} \sin\gamma + C_H\, P_{t,H'}\, \sigma^0_{VH} \cos\gamma, \end{aligned} \tag{5.11}$$

where $C_H = \frac{G_H^2\, \lambda^2\, A_{ill,H}}{(4\pi)^3\, r^4}$. This factor is used to convert NRCS to power; the values for the H-pol antenna are used since the transmitted and received waves are propagated through this antenna. The notation σ^0_{HV} refers to the NRCS observed when transmitting at H-polarization and receiving at V-polarization. The transmitted power is illustrated in figure 5.2(a).

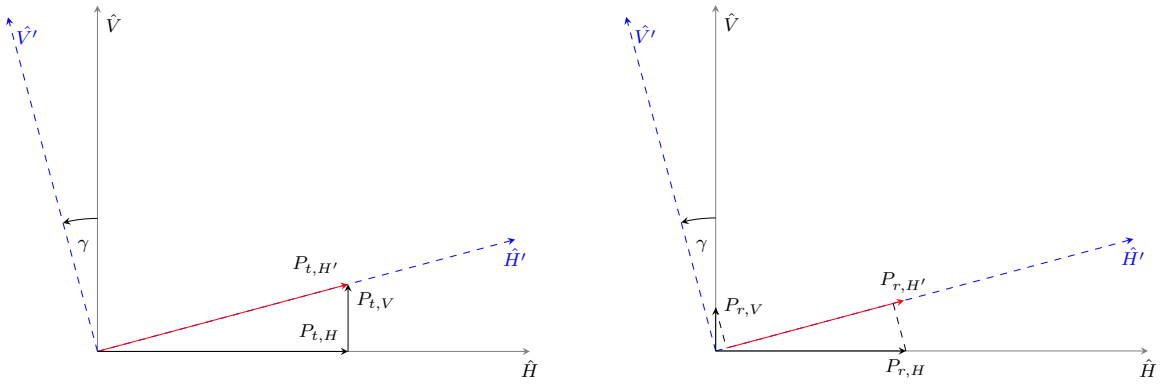

(a) Rotation on transmit

(b) Rotation on receive

Figure 5.2. Diagram illustrating the effects of polarization mixing on the transmit (a) and receive (b) vectors.

Since the antenna is rotated, the power it receives is the sum of the projections of the backscattered powers onto the original H' axis:

$$\begin{aligned} P_{r,H'} &= P_{s,H}\cos\gamma + P_{s,V}\sin\gamma \\ &= C_H\,P_{t,H'}\,\sigma^0_{HH}\cos^2\gamma + C_H\,P_{t,H'}\,\sigma^0_{HV}\cos\gamma\sin\gamma + \\ &\quad C_H\,P_{t,H'}\,\sigma^0_{VV}\sin^2\gamma + C_H\,P_{t,H'}\,\sigma^0_{VH}\cos\gamma\sin\gamma. \end{aligned} \tag{5.12}$$

These vectors are shown in figure 5.2(b). Since the cross-polarized (VH and HV) NRCS terms make a negligible contribution to the co-polarized NRCS at the wind speeds observed in this experiment, their effects are neglected here. The resulting equation relates the observed (rotated) NRCS values to the desired sea-surface NRCS values by dividing both sides of (5.12) by the transmitted power $P_{t,H'}$ and the coefficient C_H.

Extrapolating the results of (5.12) to the $V'V'$ basis,

$$\begin{aligned} \sigma^0_{V'V'} &= \sigma^0_{VV}\cos^2\gamma + \sigma^0_{HH}\sin^2\gamma \\ \sigma^0_{H'H'} &= \sigma^0_{HH}\cos^2\gamma + \sigma^0_{VV}\sin^2\gamma \end{aligned} \tag{5.13}$$

is obtained, where primes denote the rotated polarization basis. These may be inverted to obtain

$$\begin{aligned}\sigma^0_{VV} &= \frac{\sigma^0_{V'V'} + \sigma^0_{H'H'}}{2} + \frac{\sigma^0_{V'V'} - \sigma^0_{H'H'}}{2\cos 2\gamma} \\ \sigma^0_{HH} &= \frac{\sigma^0_{V'V'} + \sigma^0_{H'H'}}{2} - \frac{\sigma^0_{V'V'} - \sigma^0_{H'H'}}{2\cos 2\gamma}.\end{aligned} \tag{5.14}$$

Note the second term becomes singular when $\gamma = 45°$ (at which point both V' and H' are 45° slant polarizations), so the roll angle should be limited. The maximum roll angle was 20° and was more typically 10°–15°. The correction described is small, but without it errors in polarization ratio of up to 1.5 dB may occur.

NRCS is estimated from the echo using a pulse-limited surface area given an estimate of the transmitted power provided by an internal calibration loop. Although 126 points are averaged to obtain an NRCS estimate, the number of independent samples is approximately 7–8. Any profile with a measurable precipitation echo in the atmosphere between the aircraft and surface is considered to be contaminated by rain and is discarded.

Upon averaging many estimates, residual biases are inevitably observed in the data due to uncompensated system losses (e.g. feed lines, wet radome from previous flight through rain, etc.). A final adjustment is applied to the NRCS observed during a particular flight. For each circle during the flight and at each polarization, the difference between the observed mean NRCS and a known GMF at a known incidence angle and wind speed is computed. The mean adjustment is then applied to all circles in the flight. The wind speed used for each calculation is the mean wind speed observed within its wind speed group; it is obtained from the SFMR and is assumed to be indicative of the neutral stability wind speed at 10 m height (U_{10N}). The model function used is the corrected IWRAP GMF; valid for VV- and HH-polarizations but only at specific incidence angles [30]. The incidence angle used is the largest incidence angle available for the GMF at the corresponding polarization.

5.4 Results

Figure 5.3 shows a summary of data collected by the C-band VV-polarization radar during one of the circle patterns flown on January 24, 2011. The top panel shows NRCS as a function of the computed incidence angle (but for all aircraft headings, hence all wind directions). The individual NRCS samples collected during the circle pattern are shown as gray dots. The mean, shown as a solid line, indicates the mean NRCS—the A_0 term in the typical scatterometer directional signature, i.e.,

$$\sigma^0 = A_0 + A_1 \cos\chi + A_2 \cos 2\chi \tag{5.15}$$

where χ is the wind-relative look direction. This and subsequent mean NRCS lines do not necessarily match up with the IWRAP GMF at 50°; this is a result of applying one final adjustment per polarization to all NRCS from this flight. When the aircraft heading is added to the track-relative azimuth, one obtains the compass direction. The bottom panel shows the NRCS versus compass direction, revealing the scatterometer directional signature of (5.15). The mean NRCS over compass direction for approximately 50° incidence at $22.5\,\mathrm{m\,s^{-1}}$ is shown as a solid line. The CMOD5.N [35] and IWRAP VV-polarization GMFs are also shown. Since the IWRAP GMF is only defined for a few incidence angles, its values are shown as unconnected filled circles.

Figure 5.4 shows a summary of mean NRCS over all observation directions, or the A_0 term in (5.15), as a function of incidence angle for all dates in the Winter 2011 experiment at C-band at both VV- and HH-polarizations. For a given wind speed range, each data point is the A_0 value for one circle pattern at one polarization at one incidence angle, ±0.5°. The mean of these points are shown as a solid line. In addition, shown are the A_0 values for the IWRAP model function at the incidence angles for which it is defined and the CMOD5.N model function averaged over all azimuth angles. The data in the lowest wind speed group show more scatter than the higher wind speeds. This is influenced by the increased uncertainty in wind speed

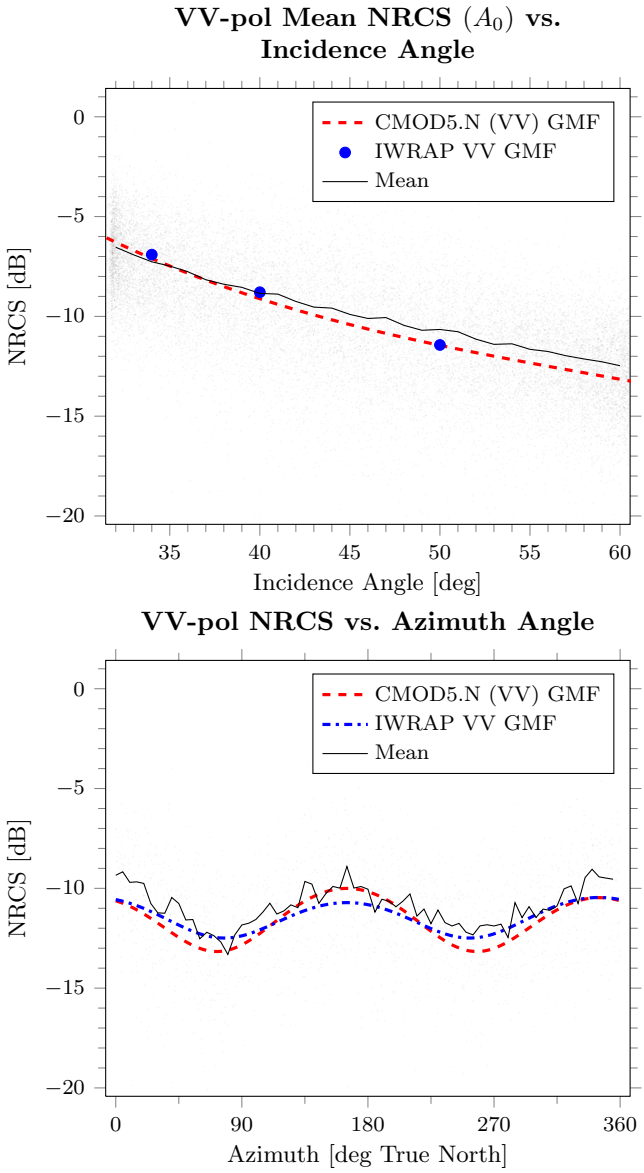

Figure 5.3. Summary from a circle pattern flown on January 24, 2011 for C-band VV-polarization. The wind speed was 22.5 m s^{-1}. The CMOD5.N and the IWRAP VV-polarization GMF are also shown at the wind speeds for which they are defined. (Top) VV-polarized NRCS (A_0) versus incidence angle for all azimuthal directions. Each NRCS sample collected is shown as a gray dot. The mean NRCS is shown as a solid line. CMOD5.N is shown as a dashed line and values from the IWRAP GMF are shown as filled circles at the incidence angles for which it is valid. (Bottom) VV-polarized NRCS versus azimuth. Each NRCS sample is shown as a gray dot. All samples between 48° and 52° incidence are averaged every 5° in azimuth and are connected with a solid line. CMOD5.N is shown as a dashed line and the IWRAP GMF at 50° incidence is shown as a dash-dotted line.

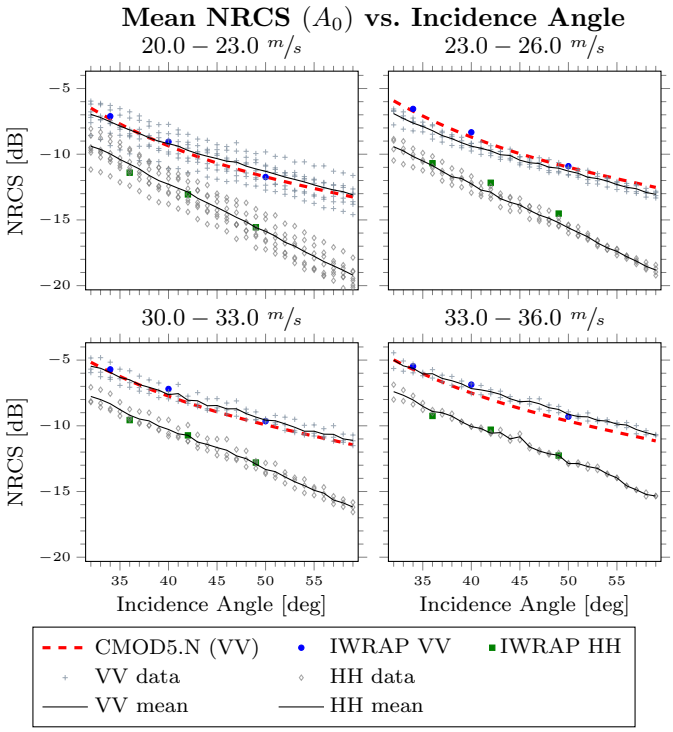

Figure 5.4. Mean NRCS (A_0) versus incidence angle for circle patterns flown on all dates in the Winter 2011 experiment grouped by wind speed. The model functions shown are computed with the mean wind speed in each wind speed range. Mean NRCS samples at each incidence angle from each circle are shown as gray plus symbols (VV-pol) and gray diamond symbols (HH-pol). The uncertainties of these means are no greater than 0.4 dB. The mean of all samples within a wind speed bin is shown as a solid line. CMOD5.N is shown as a dashed line. The IWRAP VV-pol and HH-pol GMFs are shown as filled circles and squares, respectively, at the incidence angles for which they are valid.

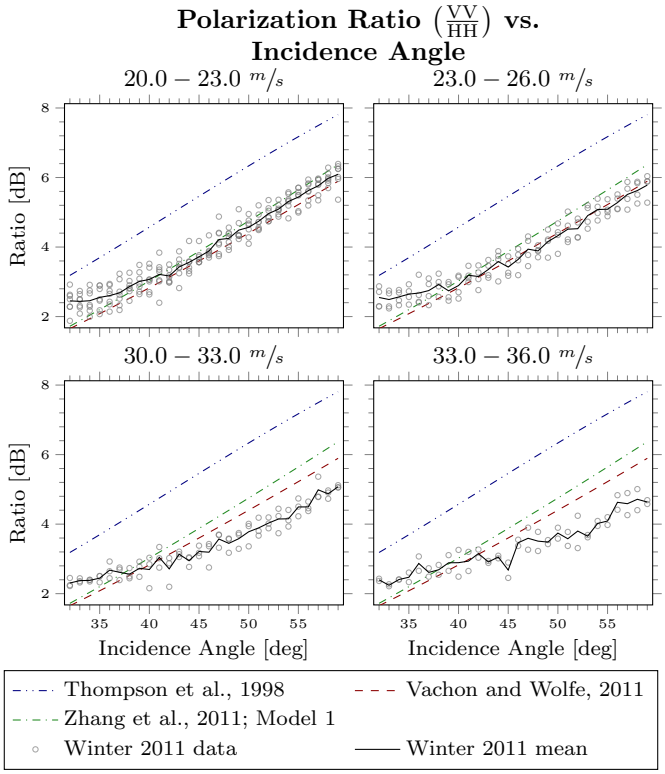

Figure 5.5. Polarization ratio VV/HH versus incidence angle grouped by wind speed. Ratios of the mean NRCS samples at each incidence angle from each circle are shown as gray circles. The mean of these is shown as a solid line. Polarization ratio models from [6], [43], [64] are also shown for reference.

retrieval from the SFMR below about $22\,\mathrm{m\,s^{-1}}$. The VV-polarization data compare well with both the CMOD5.N and IWRAP A_0 at all incidence angles shown and over all wind speeds sampled. The IWRAP HH model function compares well with the HH-polarized data for the larger two incidence angles shown; however, the IWRAP HH GMF differs from the observations at the smallest incidence angle shown. The trend in NRCS over incidence angle observed during the Winter 2011 experiment is consistent with that of CMOD5.N.

Figure 5.5 shows the polarization ratio as a function of incidence angle for all dates in the Winter 2011 experiment at C-band. For a given wind speed range, the gray circles are the ratio VV/HH of the mean A_0 at each incidence angle for one complete

Table 5.3. Coefficients for the Fit of the Mean VV-polarized NRCS as a Function of Wind-relative Azimuth Angle to $A + B\cos\ \chi + C\cos\ 2\chi$ in Linear Units

Wind Speed Group ($\mathrm{m\,s^{-1}}$)	A	B	C
20.0–23.0	1.0168	$1.8716 \cdot 10^{-3}$	$6.2065 \cdot 10^{-3}$
23.0–26.0	1.0171	$1.3911 \cdot 10^{-3}$	$5.6421 \cdot 10^{-3}$
30.0–33.0	1.0254	$1.4188 \cdot 10^{-4}$	$4.6547 \cdot 10^{-3}$
33.0–36.0	1.0285	$1.8897 \cdot 10^{-4}$	$4.6014 \cdot 10^{-3}$

Table 5.4. Coefficients for the Fit of the Mean HH-polarized NRCS as a Function of Wind-relative Azimuth Angle to $A + B\cos\ \chi + C\cos\ 2\chi$ in Linear Units

Wind Speed Group ($\mathrm{m\,s^{-1}}$)	A	B	C
20.0–23.0	1.0059	$1.4591 \cdot 10^{-3}$	$2.0956 \cdot 10^{-3}$
23.0–26.0	1.0063	$1.1929 \cdot 10^{-3}$	$2.1497 \cdot 10^{-3}$
30.0–33.0	1.0109	$2.0066 \cdot 10^{-3}$	$1.9351 \cdot 10^{-3}$
33.0–36.0	1.0126	$1.5882 \cdot 10^{-3}$	$1.2505 \cdot 10^{-3}$

circle. The wind-speed-independent polarization ratio models from [6], [43], [64] are also shown. In the lowest two wind speed groups, the ratios observed in the Winter 2011 data match reasonably well with the ratio from [6] and with Model 1 from [43] for incidence angles greater than 40°. As the wind speed increases, the incidence angle dependence on polarization ratio decreases and cannot be represented by any of the models shown. At incidence angles below 40°, the ratio begins to flatten out slightly. The ratio is expected to continue to trend towards unity as the incidence angle approaches nadir. This divergence from the models may be anticipated; both the ratios from [6] and Model 1 from [43] reach unity around 20° incidence.

Assuming a constant wind field over the area sampled during the circle pattern, the NRCS directional signature can be investigated. Figure 5.6 shows NRCS versus wind-relative azimuth angle (χ) at 50° incidence for the same wind speed bins and in the same manner as figure 5.4. The scatterometer directional signature of (5.15) is visible in all plots. As expected, with increasing wind speed the amplitude decreases,

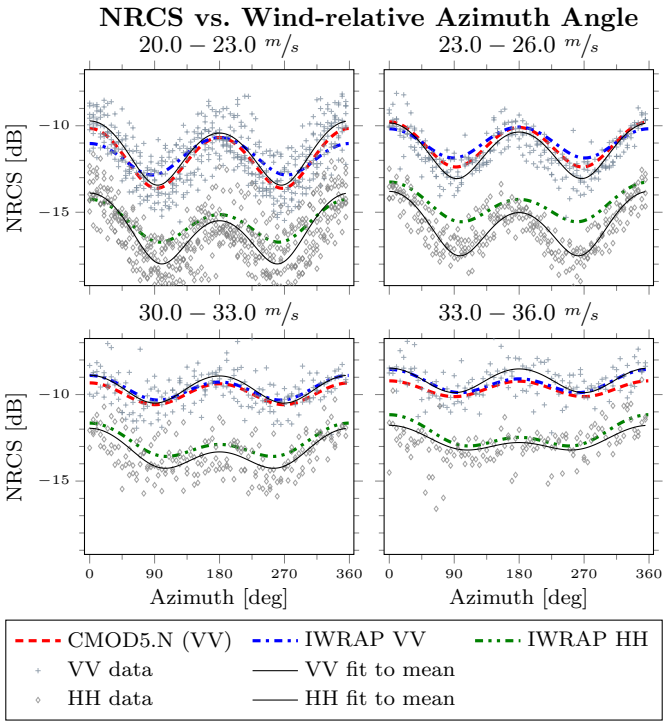

Figure 5.6. NRCS at an incidence angle of 50° versus wind-relative azimuth angle grouped by wind speed. The model functions shown are computed with the mean wind speed observed in each wind speed range. Mean NRCS samples at each incidence angle from each circle are shown as gray plus symbols (VV-pol) and gray diamond symbols (HH-pol). A function in the form of $A + B\cos\ \chi + C\cos\ 2\chi$ is fitted to the mean of each polarization's samples within a wind speed group and is shown as a solid line. The coefficients for each fit are reported in tables 5.3 and 5.4. CMOD5.N is shown as a dashed line and the IWRAP GMFs are shown as dash-dotted lines.

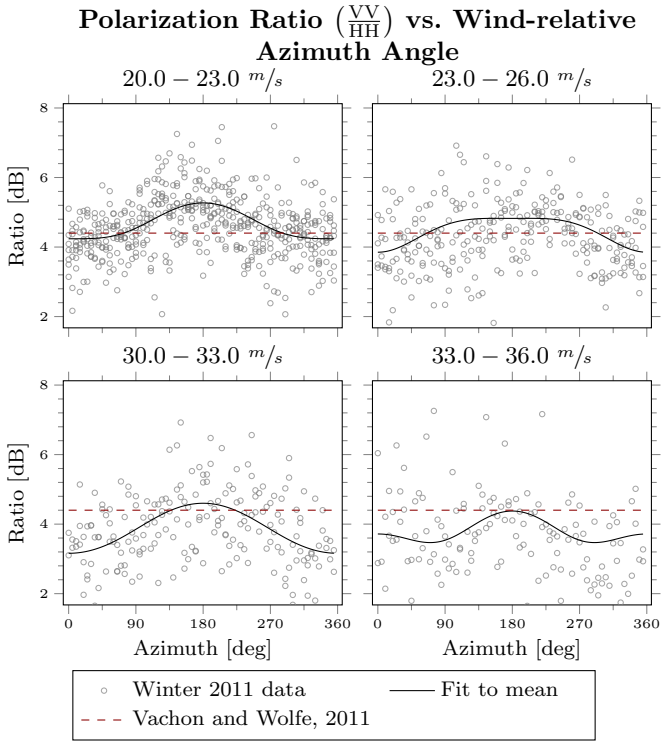

Figure 5.7. Polarization ratios VV/HH at incidence angle 50° versus wind-relative azimuth angle grouped by wind speed. Ratios of the mean NRCS sampled from each circle flight between 48° and 52° incidence are averaged in 5° azimuth bins and are shown as gray open circles. A function in the form of $A + B\cos\ \chi + C\cos\ 2\chi$ is fitted to the mean and is shown as a solid line. The coefficients for each fit are reported in table 5.5. The polarization ratio from Vachon and Wolfe [6] at 50° is shown for reference as a horizontal dashed line.

and wind direction is more difficult to unambiguously determine. In addition, shown are the CMOD5.N and IWRAP GMFs at 50° incidence.

Figure 5.7 shows the polarization ratio as a function of wind-relative azimuth angle at 50° incidence. The data points from each circle flight are shown as gray circles. The function $A + B\cos\ \chi + C\cos\ 2\chi$ is fitted to the mean and is shown as a solid line; the coefficients for each fit are reported in table 5.5. For reference, the polarization ratio from Vachon and Wolfe [6] at 50° incidence is shown as a horizontal dashed line. There is a small but measurable wind-directional signature in the polarization ratio data from the Winter 2011 experiment. This is consistent with

Table 5.5. Coefficients for the Fit of the Mean Polarization Ratio as a Function of Wind-relative Azimuth Angle to $A + B\cos\ \chi + C\cos\ 2\chi$ in Linear Units

Wind Speed Group ($\mathrm{m\,s^{-1}}$)	A	B	C
20.0–23.0	1.9661	$-1.6399 \cdot 10^{-1}$	$4.0108 \cdot 10^{-2}$
23.0–26.0	1.9162	$-1.3179 \cdot 10^{-1}$	$-3.5722 \cdot 10^{-2}$
30.0–33.0	1.7628	$-1.6599 \cdot 10^{-1}$	$1.399 \cdot 10^{-2}$
33.0–36.0	1.7406	$-7.9928 \cdot 10^{-2}$	$5.8588 \cdot 10^{-2}$

earlier observations [7], [30], [43]. There was no analytical relationship for polarization ratio as a function of azimuth angle proposed by Zhang *et al.* [43]. Moreover, while an analytical relationship with azimuth angle dependence was proposed by Mouche *et al.* [7], it is only valid between 10° and 43° incidence. As a result, only the observations by Mouche *et al.* [7] and Zhang *et al.* [43] are verified that the polarization ratio appears to have a maximum in the downwind direction for the wind speeds and incidence angles sampled.

5.5 Summary

Observations of the dual-polarized sea surface NRCS at C-band under high winds ($20\,\mathrm{m\,s^{-1}}$ to $36\,\mathrm{m\,s^{-1}}$) are reported over a range of incidence angles (32° to 60°). The polarization ratio behavior at lower wind speeds is found to be well described by the expression in Vachon and Wolfe [6], even when extrapolating beyond their measurements. However, in all wind speed groups, the slope of the polarization ratio in decibels appears to change more drastically than indicated by recent models. A dependence of polarization ratio on wind speed is also observed; as wind speed increases, the slope of the polarization ratio in decibels as a function of incidence angle decreases. Finally, a small but measurable wind-directional signature in the polarization ratio is observed, which is consistent with earlier observations [7], [30], [43].

CHAPTER 6

CONCLUSION AND FUTURE WORK

In chapter 1 the concept of remotely measured ocean surface wind vectors using microwave radars was introduced. Chapter 2 described the IWRAP airborne scatterometer/profiler, from which the data used in this dissertation comes. The Stepped Frequency Microwave Radiometer was also described, since it serves as a ground truth sensor and thus plays a key role in this work.

Chapter 3 extended scatterometer geophysical model function to 22° in both C- and Ku-bands and at both VV- and HH-polarizations. This chapter also confirmed the behavior of the IWRAP A_0 GMF at the outer incidence angles, introducing more data and independent analysis of the existing GMF. The behavior of the higher harmonics of the existing IWRAP GMF are questionable, considering the data presented. Since the data shown in this chapter are supported by empirical, satellite-derived GMFs, revision of the a_1 and a_2 GMFs are suggested.

Chapter 4 addressed the precipitation splash effect on sea-surface NRCS at approximately 22° incidence. The two IWRAP radars were used in a dual-frequency attenuation estimation method to verify that SFMR was a viable method of measuring precipitation. The IWRAP-derived mean specific attenuation as a function of SFMR rain rate was found to match reasonably well with existing models. The same flight experiments from chapter 3 were used in this chapter, except that rainy data were not discarded. After applying a frequency-specific attenuation model to the data, some offset with the new IWRAP GMF in the mean NRCS (A_0) was observed. Since a small vertical shift of the specific attenuation-rain rate models could not be ruled out,

a small adjustment was made to all rainy data so that the mean NRCS at $25\,\mathrm{m\,s^{-1}}$ in light rain matches the rain-free GMF. No measurable effect due to precipitation was observed in the mean NRCS or normalized first harmonic (a_1) at wind speeds from $15\,\mathrm{m\,s^{-1}}$ to $45\,\mathrm{m\,s^{-1}}$ at C- and Ku-band and VV- and HH-polarizations. A dampening effect on the normalized second harmonic (a_2) was observed at all frequencies and polarizations, consistent with other observations that precipitation hampers direction retrieval.

Chapter 5 examined C-band data from the winter 2011 IWRAP and SFMR flight experiments in which 360° aircraft orbits were performed in a variety of wind speeds ranging from $20\,\mathrm{m\,s^{-1}}$ to $36\,\mathrm{m\,s^{-1}}$. The polarization ratio $\frac{VV}{HH}$ at high wind speeds was examined as a function of incidence angle (between 32° and 60°) and azimuth angle. The polarization ratio as a function of incidence angle was observed to have a wind speed dependence. Additionally, a small azimuthal polarization ratio was observed, both of which are consistent with previous observations. The data taken during this experiment were not fully utilized, since both Ku-band channels and the inner C-band incidence angle channel were not analyzed. In the future, these could provide additional verification of the behavior at the low incidence angle GMFs developed in chapter 3.

Cross-polarized NRCS measurements, in which the radar transmits in one polarization and receives in the other, seem to have great potential for retrieving high-speed ocean vector winds [6], [65]. IWRAP is in a good position to investigate this phenomena at high winds, but the cross-polarized signature needs to overcome the low isolation of the antennas. Since IWRAP has been capable of measuring the cross-polarization signal, there have been few flights where this is a possibility—and all were during the hurricane season of 2014. These flights have not been thoroughly investigated yet, but this is an area of high interest to the scatterometer community.

BIBLIOGRAPHY

[1] D. E. Barrick and C. T. Swift, "The seasat microwave instruments in historical perspective," *IEEE Journal of Oceanic Engineering*, vol. 5, no. 2, pp. 74–79, Apr. 1980. DOI: 10.1109/JOE.1980.1145457.

[2] W. T. Liu and W. Tang, "Equivalent neutral wind," National Aeronautics and Space Administration, Jet Propulsion Laboratory, California Institute of Technology, JPL Publication 96-17, Aug. 1, 1996.

[3] M. Portabella, A. Stoffelen, W. Lin, A. Turiel, A. Verhoef, J. Verspeek, and J. Ballabrera-Poy, "Rain effects on ASCAT-retrieved winds: Toward an improved quality control," *IEEE Transactions on Geoscience and Remote Sensing*, vol. 50, no. 7, pp. 2495–2506, Jul. 2012. DOI: 10.1109/TGRS.2012.2185933.

[4] D. E. Weissman, B. W. Stiles, S. M. Hristova-Veleva, D. G. Long, D. K. Smith, K. A. Hilburn, and W. L. Jones, "Challenges to satellite sensors of ocean winds: Addressing precipitation effects," *Journal of Atmospheric and Oceanic Technology*, vol. 29, no. 3, pp. 356–374, Mar. 2012. DOI: 10.1175/JTECH-D-11-00054.1.

[5] B. Zhang, W. Perrie, P. W. Vachon, X. Li, W. G. Pichel, J. Guo, and Y. He, "Ocean vector winds retrieval from c-band fully polarimetric SAR measurements," *IEEE Transactions on Geoscience and Remote Sensing*, vol. 50, no. 11, pp. 4252–4261, Nov. 2012. DOI: 10.1109/TGRS.2012.2194157.

[6] P. W. Vachon and J. Wolfe, "C-band cross-polarization wind speed retrieval," *IEEE Geoscience and Remote Sensing Letters*, vol. 8, no. 3, pp. 456–459, 2011. DOI: 10.1109/LGRS.2010.2085417.

[7] A. Mouche, D. Hauser, J.-F. Daloze, and C. Guerin, "Dual-polarization measurements at c-band over the ocean: Results from airborne radar observations and comparison with ENVISAT ASAR data," *IEEE Transactions on Geoscience and Remote Sensing*, vol. 43, no. 4, pp. 753–769, Apr. 2005. DOI: 10.1109/TGRS.2005.843951.

[8] R. Moore and A. Fung, "Radar determination of winds at sea," *Proc. IEEE*, vol. 67, no. 11, pp. 1504–1521, 1979. DOI: 10.1109/PROC.1979.11510.

[9] W. L. Jones, L. C. Schroeder, D. H. Boggs, E. M. Bracalente, R. A. Brown, G. J. Dome, W. J. Pierson, and F. J. Wentz, "The SEASAT-a satellite scatterometer: The geophysical evaluation of remotely sensed wind vectors over the ocean," *Journal of Geophysical Research: Oceans*, vol. 87, pp. 3297–3317, C5 Apr. 30, 1982. DOI: 10.1029/JC087iC05p03297.

[10] F. Naderi, M. Freilich, and D. Long, "Spaceborne radar measurement of wind velocity over the ocean-an overview of the NSCAT scatterometer system," *Proceedings of the IEEE*, vol. 79, no. 6, pp. 850–866, Jun. 1991. DOI: 10.1109/5.90163.

[11] A. Stoffelen and D. Anderson, "Scatterometer data interpretation: Measurement space and inversion," *Journal of Atmospheric and Oceanic Technology*, vol. 14, no. 6, pp. 1298–1313, Dec. 1997. DOI: 10.1175/1520-0426(1997)014<1298:SDIMSA>2.0.CO;2.

[12] W.-Y. Tsai, J. Graf, C. Winn, J. Huddleston, S. Dunbar, M. Freilich, F. Wentz, D. Long, and W. Jones, "Postlaunch sensor verification and calibration of the NASA scatterometer," *IEEE Transactions on Geoscience and Remote Sensing*, vol. 37, no. 3, pp. 1517–1542, May 1999. DOI: 10.1109/36.763264.

[13] W.-Y. Tsai, M. Spencer, C. Wu, C. Winn, and K. Kellogg, "SeaWinds on QuikSCAT: Sensor description and mission overview," in *Proc. 2000 IEEE Int. Geosci. and Remote Sens. Symp.*, vol. 3, 2000, 1021–1023 vol.3. DOI: 10.1109/IGARSS.2000.858008.

[14] "NASA QuickScat satellite antenna experiences age-related failure," *Satellite Today*, vol. 8, no. 232, Nov. 25, 2009.

[15] J. M. Von Ahn, J. M. Sienkiewicz, and P. S. Chang, "Operational impact of QuikSCAT winds at the NOAA ocean prediction center," *Weather and Forecasting*, vol. 21, no. 4, pp. 523–539, Aug. 1, 2006. DOI: 10.1175/WAF934.1.

[16] J. Figa-Saldaña, J. J. Wilson, E. Attema, R. Gelsthorpe, M. R. Drinkwater, and A. Stoffelen, "The advanced scatterometer (ASCAT) on the meteorological operational (MetOp) platform: A follow on for european wind scatterometers," *Canadian Journal of Remote Sensing*, vol. 28, no. 3, pp. 404–412, 2002. DOI: 10.5589/m02-035.

[17] NASA JPL. (2014). Rapidscat, [Online]. Available: http://winds.jpl.nasa.gov/missions/RapidScat/ (visited on 12/31/2014).

[18] D. E. Fernandez, E. M. Kerr, A. Castells, J. R. Carswell, S. J. Shaffer, P. S. Chang, P. G. Black, and F. D. Marks, "IWRAP: The imaging wind and rain airborne profiler for remote sensing of the ocean and the atmospheric boundary layer within tropical cyclones," *IEEE Transactions on Geoscience and Remote Sensing*, vol. 43, no. 8, pp. 1775–1787, 2005. DOI: 10.1109/TGRS.2005.851640.

[19] J. Dvorsky, "Implementation of dual-polarization on an airborne scatterometer and preliminary data quality," Paper 743, Master's thesis, University of Massachusetts Amherst, Feb. 2012.

[20] T. Chu, "Operation and improvement of the IWRAP airborne doppler radar/scatterometer," Master's thesis, University of Massachusetts Amherst, Feb. 2008.

[21] D. Esteban-Fernandez, "Remote sensing of the ocean and the atmospheric boundary layer within tropical cyclones," University of Massachusetts Amherst, Feb. 2005.

[22] J. J. McManus, S. J. Frasier, and J. R. Carswell, "Implementation of pulse compression on an airborne scatterometer," in *Proc. 2008 IEEE Int. Geosci. and Remote Sens. Symp.*, Boston, MA, 2008, pp. 1418–1421. DOI: 10.1109/IGARSS.2008.4779999.

[23] J. J. McManus, "Implementing pulse compression in the IWRAP airborne doppler radar/scatterometer," Master's thesis, University of Massachusetts Amherst, Feb. 2009.

[24] W. L. Jones, P. G. Black, V. E. Delnore, and C. T. Swift, "Airborne microwave remote-sensing measurements of hurricane allen," *Science*, New Series, vol. 214, no. 4518, pp. 274–280, Oct. 16, 1981.

[25] F. T. Ulaby, R. K. Moore, and A. K. Fung, *Microwave Remote Sensing : Fundamentals and Radiometry*. Reading, MA: Addison-Wesley Pub. Co. Advanced Book Program/World Science Division, 1981, vol. 1, 456 pp.

[26] L. A. Klein and C. T. Swift, "An improved model for the dielectric constant of sea water at microwave frequencies," *IEEE Journal of Oceanic Engineering*, vol. 2, no. 1, pp. 104–111, Jan. 1977.

[27] E. W. Uhlhorn, P. G. Black, J. L. Franklin, M. Goodberlet, J. Carswell, and A. S. Goldstein, "Hurricane surface wind measurements from an operational stepped frequency microwave radiometer," *Monthly Weather Review*, vol. 135, no. 9, pp. 3070–3085, 2007. DOI: 10.1175/MWR3454.1.

[28] E. W. Uhlhorn and P. G. Black, "Verification of remotely sensed sea surface winds in hurricanes," *Journal of Atmospheric and Oceanic Technology*, vol. 20, no. 1, p. 99, Jan. 2003. DOI: 10.1175/1520-0426(2003)020<0099:VORSSS>2.0.CO;2.

[29] E. J. Knapp, J. R. Carswell, and C. T. Swift, "A dual polarization multi-frequency microwave radiometer," in *Proc. 2000 IEEE Int. Geosci. and Remote Sens. Symp.*, vol. 7, Honolulu, HI, 2000, pp. 3160–3162. DOI: 10.1109/IGARSS.2000.860369.

[30] D. E. Fernandez, J. R. Carswell, S. Frasier, P. S. Chang, P. G. Black, and F. D. Marks, "Dual-polarized c- and ku-band ocean backscatter response to hurricane-force winds," *Journal of Geophysical Research*, vol. 111, C8 2006. DOI: 10.1029/2005JC003048.

[31] (2013). Stepped frequency microwave radiometer (SFMR) - ProSensing, inc, [Online]. Available: http://www.prosensing.com/sensors/radiometers/hurricane/sfmr/ (visited on 11/06/2013).

[32] T. Schott, C. Landsea, G. Hafele, J. Lorens, A. Taylor, H. Thurm, B. Ward, M. Willis, and W. Zaleski. (Feb. 1, 2012). The saffir-simpson hurricane wind scale, The Saffir-Simpson Hurricane Wind Scale, [Online]. Available: http://www.nhc.noaa.gov/sshws.shtml (visited on 10/01/2012).

[33] A. Verhoef, M. Portabella, A. Stoffelen, and H. Hersbach, "CMOD5.n - the CMOD5 GMF for neutral winds," SAF/OSI/CDOP/KNMI/TEC/TN/165, May 2008.

[34] H. Hersbach, "CMOD5 - An improved geophysical model function for ERS c-band scatterometry," ECMWF Technical Memorandum 395, 2003.

[35] H. Hersbach, A. Stoffelen, and S. de Haan, "An improved c-band scatterometer ocean geophysical model function: CMOD5," *Journal of Geophysical Research*, vol. 112, C3 Mar. 2007. DOI: 10.1029/2006JC003743.

[36] S. Soisuvarn, Z. Jelenak, P. S. Chang, S. O. Alsweiss, and Q. Zhu, "CMOD5.h—A high wind geophysical model function for C-band vertically polarized satellite scatterometer measure-

ments," *IEEE Transactions on Geoscience and Remote Sensing*, pp. 1–17, Nov. 22, 2012. DOI: 10.1109/TGRS.2012.2219871.

[37] L. Ricciardulli and F. Wentz, "Reprocessed QuikSCAT (v04) wind vectors with ku-2011 geophysical model function," Remote Sensing Systems, Santa Rosa, CA, 043011, Apr. 30, 2011.

[38] T. Meissner and F. J. Wentz, "Wind-vector retrievals under rain with passive satellite microwave radiometers," *IEEE Trans. Geosci. Remote Sens.*, vol. 47, no. 9, pp. 3065–3083, Sep. 2009. DOI: 10.1109/TGRS.2009.2027012.

[39] W. J. Donnelly, J. R. Carswell, R. E. McIntosh, P. S. Chang, J. Wilkerson, F. Marks, and P. G. Black, "Revised ocean backscatter models at c and ku band under high-wind conditions," *Journal of Geophysical Research*, vol. 104, pp. 11 485–11 497, C5 1999. DOI: 10.1029/1998JC900030.

[40] M. I. Skolnik, *Introduction to radar systems*, 3rd edition. Boston: McGraw Hill, 2001.

[41] W. T. Liu, X. Xie, and W. Tang, "Scatterometer's unique capability in measuring ocean surface stress," in *Oceanography from Space*, V. Barale, J. Gower, and L. Alberotanza, Eds., Chapter 6, Springer Science, 2010, pp. 93–111.

[42] A. Bentamy, K. B. Katsaros, A. M. Mestas-Nuñez, W. M. Drennan, E. B. Forde, and H. Roquet, "Satellite estimates of wind speed and latent heat flux over the global oceans," *Journal of Climate*, vol. 16, no. 4, pp. 637–656, Feb. 1, 2003. DOI: 10.1175/1520-0442(2003)016<0637:SEOWSA>2.0.CO;2.

[43] B. Zhang, W. Perrie, and Y. He, "Wind speed retrieval from RADARSAT-2 quad-polarization images using a new polarization ratio model," *Journal of Geophysical Research*, vol. 116, Aug. 4, 2011. DOI: 10.1029/2010JC006522.

[44] M. Portabella and A. Stoffelen, "Scatterometer backscatter uncertainty due to wind variability," *IEEE Transactions on Geoscience and Remote Sensing*, vol. 44, no. 11, pp. 3356–3362, Nov. 2006. DOI: 10.1109/TGRS.2006.877952.

[45] M. D. Powell, E. W. Uhlhorn, and J. D. Kepert, "Estimating maximum surface winds from hurricane reconnaissance measurements," *Weather & Forecasting*, vol. 24, no. 3, pp. 868–883, Jun. 2009. DOI: 10.1175/2008WAF2007087.1.

[46] N. Tran, B. Chapron, and D. Vandemark, "Effect of long waves on ku-band ocean radar backscatter at low incidence angles using TRMM and altimeter data," *IEEE Geoscience and Remote Sensing Letters*, vol. 4, no. 4, pp. 542–546, Oct. 2007. DOI: 10.1109/LGRS.2007.896329.

[47] R. F. Contreras and W. J. Plant, "Surface effect of rain on microwave backscatter from the ocean: Measurements and modeling," *J. Geophys. Res.*, vol. 111, C8 2006. DOI: 10.1029/2005JC003356.

[48] A. M. Worthington, *A study of splashes*. London: Longmans, Green, and Co., 1908.

[49] C. Nie and D. G. Long, "A C-band wind / rain backscatter model," *IEEE Transactions on Geoscience and Remote Sensing*, vol. 45, no. 3, pp. 621–631, Mar. 2007. DOI: 10.1109/TGRS.2006.888457.

[50] D. E. Weissman and M. A. Bourassa, "The influence of rainfall on scatterometer backscatter within tropical cyclone environments—implications on parameterization of sea-surface stress," *IEEE Transactions on Geoscience and Remote Sensing*, vol. 49, no. 12, pp. 4805–4814, Dec. 2011. DOI: 10.1109/TGRS.2011.2170842.

[51] J. R. Carswell, D. Perkovic, T. Chu, S. J. Frasier, P. Chang, and Z. Jelenak, "Preliminary investigation of splash effect on high wind c-band HH-pol model function," in *Proc. 2010 IEEE Int. Geosci. and Remote Sens. Symp.*, Jul. 25, 2010. DOI: 10.1109/IGARSS.2010.5651890.

[52] Z. Jelenak and P. Chang, "Impact of the dual-frequency scatterometer on NOAA operations," in *Proc. 2010 IEEE Int. Geosci. and Remote Sens. Symp.*, Jul. 2010, pp. 1808–1811. DOI: 10.1109/IGARSS.2010.5654168.

[53] E. Rodriguez, R. Gaston, S. Durden, B. Stiles, M. Spencer, L. Veilleux, R. Hughes, D. Fernadez, S. Chan, S. Veleva, and R. Dunbar, "A scatterometer for XOVWM, the extended ocean vector winds mission," in *2009 IEEE Radar Conference*, May 2009, pp. 1–4. DOI: 10.1109/RADAR.2009.4977093.

[54] R. J. Doviak and D. S. Zrnić, *Doppler Radar and Weather Observations: Second Edition*. Mineola, NY: Dover Publications, May 26, 2006.

[55] M. Fujita and M. Satake, "Rainfall rate profiling with attenuating-frequency radar using nonlinear LMS technique under a constraint on path-integrated rainfall rate," *International Journal of Remote Sensing*, vol. 18, no. 5, pp. 1137–1147, Mar. 1997. DOI: 10.1080/014311697218610.

[56] P. J. Eccles and E. A. Mueller, "X-band attenuation and liquid water content estimation by a dual-wavelength radar," *Journal of Applied Meteorology*, vol. 10, no. 6, pp. 1252–1259, Dec. 1971. DOI: 10.1175/1520-0450(1971)010<1252:XBAALW>2.0.CO;2.

[57] D. Atlas and C. W. Ulbrich, "Path- and area-integrated rainfall measurement by microwave attenuation in the 1–3 cm band," *Journal of Applied Meteorology*, vol. 16, no. 12, pp. 1322–1331, Dec. 1977. DOI: 10.1175/1520-0450(1977)016<1322:PAAIRM>2.0.CO;2.

[58] "Specific attenuation model for rain for use in prediction methods," ITU, reference P.838-3, Mar. 2005.

[59] C. Nie and D. G. Long, "A c-band scatterometer simultaneous wind / rain retrieval method," *IEEE Transactions on Geoscience and Remote Sensing*, vol. 46, no. 11, pp. 3618–3631, Nov. 2008. DOI: 10.1109/TGRS.2008.922146.

[60] F. M. Monaldo, D. R. Thompson, R. C. Beal, W. G. Pichel, and P. Clemente-Colon, "Comparison of SAR-derived wind speed with model predictions and ocean buoy measurements," *IEEE Transactions on Geoscience and Remote Sensing*, vol. 39, no. 12, pp. 2587–2600, Dec. 2001. DOI: 10.1109/36.974994.

[61] P. W. Vachon and F. W. Dobson, "Wind retrieval from RADARSAT SAR images: Selection of a c-band HH polarization wind retrieval model," *Canadian Journal of Remote Sensing*, vol. 26, no. 4, pp. 306–313, 2000.

[62] J. W. Sapp, S. J. Frasier, J. Dvorsky, P. S. Chang, and Z. Jelenak, "Airborne dual-polarization observations of the sea surface NRCS at c-band in high winds," *IEEE Geoscience and Remote Sensing Letters*, vol. 10, no. 4, pp. 726–730, Jul. 2013. DOI: 10.1109/LGRS.2012.2220118.

[63] W.-C. Lee, P. Dodge, F. D. Marks, and P. H. Hildebrand, "Mapping of airborne doppler radar data," *Journal of Atmospheric and Oceanic Technology*, vol. 11, pp. 572–578, Apr. 1994.

[64] D. Thompson, T. Elfouhaily, and B. Chapron, "Polarization ratio for microwave backscattering from the ocean surface at low to moderate incidence angles," in *Proc. 1998 IEEE Int. Geosci. and Remote Sens. Symp.*, vol. 3, Seattle, WA, USA: IEEE, 1998, pp. 1671–1673. DOI: 10.1109/IGARSS.1998.692411.

[65] P. Hwang, W. Perrie, and B. Zhang, "Cross-polarization radar backscattering from the ocean surface and its dependence on wind velocity," *IEEE Geoscience and Remote Sensing Letters*, vol. 11, no. 12, pp. 2188–2192, Dec. 2014. DOI: 10.1109/LGRS.2014.2324276.